

COSMOGLOBE I. Improved Wilkinson Microwave Anisotropy Probe frequency maps through Bayesian end-to-end analysis

D. J. Watts^{1*}, A. Basyrov¹, H. T. Ihle¹, S. Paradiso², F. Rahman³, H. Thommesen¹, M. Bersanelli⁴, L. A. Bianchi⁴, M. Brilenkov¹, L. P. L. Colombo⁴, H. K. Eriksen¹, J. R. Eskilt^{1,5}, K. S. F. Fornazier⁶, U. Fuskeland¹, M. Galloway¹, E. Gjerløw¹, B. Hensley⁷, L. T. Herzt⁸, D. Herman¹, G. A. Hoerning⁶, K. Lee¹, J. G. S. Lunde¹, A. Marins^{6,9}, S. K. Nerval^{10,11}, S. K. Patel¹², M. Regnier¹³, M. San¹, S. Sanyal¹², N.-O. Stutz¹, A. Verma¹², I. K. Wehus¹, and Y. Zhou¹⁴

¹ Institute of Theoretical Astrophysics, University of Oslo, Blindern, Oslo, Norway

² Waterloo Centre for Astrophysics, University of Waterloo, Waterloo, ON N2L 3G1, Canada

³ Indian Institute of Astrophysics, Koramangala II Block, Bangalore, 560034, India

⁴ Dipartimento di Fisica, Università degli Studi di Milano, Via Celoria, 16, Milano, Italy

⁵ Imperial Centre for Inference and Cosmology, Department of Physics, Imperial College London, Blackett Laboratory, Prince Consort Road, London SW7 2AZ, United Kingdom

⁶ Instituto de Física, Universidade de São Paulo - C.P. 66318, CEP: 05315-970, São Paulo, Brazil

⁷ Department of Astrophysical Sciences, Princeton University, 4 Ivy Lane, Princeton, NJ 08540

⁸ Department of Physics and Astronomy, University of British Columbia, 6224 Agricultural Road, Vancouver BC, V6T1Z1, Canada

⁹ Department of Astronomy, University of Science and Technology of China, Hefei, China

¹⁰ David A. Dunlap Department of Astronomy & Astrophysics, University of Toronto, 50 St. George Street, Toronto, ON M5S 3H4, Canada

¹¹ Dunlap Institute for Astronomy & Astrophysics, University of Toronto, 50 St. George Street, Toronto, ON M5S 3H4, Canada

¹² Department of Physics, Indian Institute of Technology (BHU), Varanasi - 221005, India

¹³ Laboratoire Astroparticule et Cosmologie (APC), Université Paris-Cité, Paris, France

¹⁴ Department of Physics, UC Berkeley

February 28, 2023

ABSTRACT

We present the first joint analysis of *WMAP* and *Planck* LFI time-ordered data, processed within the Bayesian end-to-end COSMOGLOBE framework. This framework builds directly on a similar analysis of the LFI measurements by the BEYONDPLANCK collaboration, and approaches the CMB analysis challenge through Gibbs sampling of a global posterior distribution. The computational cost of producing one complete *WMAP*+LFI Gibbs sample is 581 CPU-hr, including calibration, map-making, and component separation, of which 389 CPU-hr is spent on *WMAP* low-level processing; this demonstrates that end-to-end Bayesian analysis of the *WMAP* data is computationally feasible. We find that our *WMAP* posterior mean temperature sky maps are largely consistent with the official maps, and the resulting CMB power spectrum is in excellent agreement with previous results. The most notable difference is a slightly lower CMB quadrupole amplitude of $\sigma_2 = 120 \pm 65 \mu\text{K}^2$, as compared to $\sigma_2 = 229 \pm 97 \mu\text{K}^2$ in the BEYONDPLANCK analysis. In contrast, our *WMAP* polarization maps differ more notably from the official results, and in general they exhibit weaker transmission imbalance residuals; it is particularly noteworthy that our *W*-band sky maps appear statistically consistent with the *V*-band maps. At a higher level, *WMAP*-minus-LFI frequency map differences appear for the first time visually consistent with instrumental noise over most of the sky. Still, we identify three specific issues that require additional work, namely 1) noise mismodelling at high temporal frequencies, 2) a quadrupolar *V*-band temperature residual at the $2 \mu\text{K}$ level; and 3) a strong degeneracy between the absolute *K*-band calibration and the dipole of the anomalous microwave emission component. Nevertheless, we believe that the reprocessed *WMAP* maps presented here are significantly cleaner in terms of systematic uncertainties than the official *WMAP* maps, and they should be preferable for most scientific analyses that rely on *WMAP* measurements. Both sky maps and the associated code are made publicly available through the COSMOGLOBE web page.

Key words. ISM: general – Cosmology: observations, polarization, cosmic microwave background, diffuse radiation – Galaxy: general

Contents

1	Introduction	2	2.4 Sky model	4
2	End-to-end Bayesian CMB analysis	3	2.5 Priors	5
2.1	LFI and BEYONDPLANCK	3	2.6 Posterior distribution and Gibbs sampling	5
2.2	Official <i>WMAP</i> pipeline	3	2.7 Sampling algorithms	5
2.3	Instrument model	4	2.7.1 Review of sampling algorithms	5
			2.7.2 Differential mapmaking	6
			2.7.3 Transmission imbalance estimation	7
			2.7.4 Baseline sampling	7

* Corresponding author: D. J. Watts; duncanwa@astro.uio.no

3 Data and data processing

3.1 Publicly available <i>WMAP</i> products	7	<i>COBE</i> -DMR, aiming to map the microwave sky with 45 times higher sensitivity and 33 times higher angular resolution, and thereby revolutionizing our understanding of early universe physics (Bennett et al. 2003a). As quantified by Bennett et al. (2013), the permissible parameter space volume for a standard Λ CDM model was decreased by a factor of 68,000 by <i>WMAP</i> , and the best pre- <i>WMAP</i> determination of the age of the universe was $t_0 < 14$ Gyr from Boomerang (Lange et al. 2001), with best-fit values of 9–11 Gyr; the latter values in apparent contradiction with direct measurements of the oldest globular clusters (Hu et al. 2001).
3.2 TOD pre-processing and data selection	8	
3.3 Computational resources	9	
4 Instrumental parameters	9	
4.1 Trace plots and correlations	9	
4.2 Gain and baselines	9	
4.3 Transmission imbalance	10	
4.4 Instrumental noise and goodness-of-fit	10	
4.5 Astrophysical sky model	12	
5 Frequency maps	15	
5.1 Map summary statistics	15	
5.2 Comparison with 9-year <i>WMAP</i> maps	16	
5.3 Consistency within <i>WMAP</i> channels	16	
5.4 Consistency between <i>WMAP</i> and LFI	16	
6 Preliminary astrophysical results	16	
6.1 CMB results	16	
6.1.1 Solar dipole	16	
6.1.2 Quadrupole and octopole	16	
6.1.3 Angular temperature power spectrum	16	
6.1.4 Large-scale polarization	16	
6.2 Galactic foregrounds	16	
6.3 <i>WMAP</i> -versus-LFI signal-to-noise ratio comparison	16	
7 Systematic error corrections and uncertainties	16	
7.1 Sky map corrections	16	
7.2 Power spectrum residuals	16	
8 Outstanding issues	16	
8.1 Noise modelling	16	
8.2 <i>V</i> -band quadrupole residual	16	
8.3 Degeneracy between <i>K</i> -band calibration and AME dipole	16	
8.4 Other minor effects	16	
8.4.1 Time-variable bandpass modelling	16	
8.4.2 Polarized sidelobe modelling	16	
9 Conclusions	16	
A Survey of instrumental parameters	37	
A.1 Gain, baselines, noise and χ^2	37	
A.2 Transmission imbalance	37	
B WMAP frequency map survey	37	
C Comparison with BEYONDPLANCK LFI results	37	

1. Introduction

The discovery of the cosmic microwave background (CMB) by Penzias & Wilson (1965) marked a paradigm shift in the field of cosmology, providing direct evidence that the Universe was once much hotter than it is today, effectively ruling out the steady-state theory of the universe (Dicke et al. 1965). This discovery spurred a series of ground-breaking cosmological experiments, including the Nobel Prize-winning measurements by *COBE*-FIRAS and *COBE*-DMR that confirmed the blackbody nature of the CMB Mather et al. (1994) and measured temperature variations from the primordial gravitational field (Smoot et al. 1992).

The NASA-funded *Wilkinson Microwave Anisotropy Probe* (*WMAP*; Bennett et al. 2003a) mission directly superseded

The ESA-led *Planck* satellite (Planck Collaboration I 2020) was developed concurrently with *WMAP*, and their operation lifetimes briefly overlapped, with *Planck* observing from 2009–2013 and *WMAP* from 2001–2011. *Planck*'s stated goal was to fully characterize the primary CMB temperature fluctuations from recombination, as well as to characterize the polarized microwave sky on large angular scales. Overall, *Planck*'s raw CMB sensitivity was an order of magnitude higher than *WMAP*'s, and its angular resolution three times higher, and *Planck* represents today the state-of-the-art in terms of full-sky microwave sky measurements.

Planck comprised two independent experiments, namely the Low Frequency Instrument (LFI; Planck Collaboration II 2020) and High Frequency Instrument (HFI; Planck Collaboration III 2020), respectively. The LFI detectors were based on HEMT (high electron mobility transistor) amplifiers, spanning three frequency channels between 30 and 70 GHz, while the HFI detectors were based on TES (transition edge sensitive) bolometers, and spanned six frequency channels between 100 and 857 GHz. For comparison, *WMAP* was also HEMT-based, with comparable sensitivity as LFI alone, and spanned five frequencies between 23 and 94 GHz. At the same time, the two experiments implemented very different scanning strategies, and as a result they are highly complementary and synergistic, and together provide a clearer view of the low-frequency microwave sky than either can alone.

Towards the end of the *Planck* analysis phase it became clear that the interplay between instrument calibration and astrophysical component separation represents a main limiting factor in terms of systematic effects for high signal-to-noise measurements (Planck Collaboration II 2020). Specifically, in order to calibrate the instrument to sufficient precision, it is necessary to know the true sky to a comparably high precision – but to know the sky, it is also necessary to know the instrumental calibration. The data analysis is thus fundamentally circular and global in nature. For the final *Planck* LFI analysis, four complete iterations between calibration and component separation were performed (Planck Collaboration II 2020), aiming to probe this degeneracy. However, it was clearly recognized that this was not sufficient to reach full convergence, and this sub-optimality led to the BEYONDPLANCK project (BeyondPlanck 2022), which aimed to perform thousands of complete analysis cycles, as opposed to just a handful. This framework was implemented in terms of the Commander3 (Galloway et al. 2022) code, a CMB Gibbs sampler that performs integrated high-level and low-level parameter estimation in a single integrated framework. This analysis demonstrated the feasibility of a full end-to-end Gibbs sampling analysis in the CMB framework, while providing the highest-quality LFI maps to date.

Rather than simply probing the degeneracy between instrument calibration and component separation, a better solution is to actually break it. And the optimal approach to do so is by jointly analyzing complementary datasets, each of which pro-

vide key information regarding the full system. This insight led to the COSMOGLOBE¹ initiative, which is an Open Source and community-wide effort that aims to derive a single joint model of the radio, microwave, and sub-millimeter sky by combining all state-of-the-art experiments. An obvious first extension of the LFI-oriented BEYONDPLANCK project is to analyze the *WMAP* measurements in the same framework. Indeed, already as part of the BEYONDPLANCK suite of papers, Watts et al. (2022) integrated *WMAP* *Q*-band TODs into the Commander3 framework, calibrated off of the BEYONDPLANCK sky model.

In this paper, we present the first end-to-end Bayesian analysis of the full *WMAP* time-ordered data (TOD), processed within the COSMOGLOBE framework. As such, this paper also presents the first joint analysis ever of two major CMB experiments (LFI and *WMAP*) at the lowest possible level, and as such it constitutes a major milestone of the COSMOGLOBE project. In the future, many more datasets will be added, gradually providing stronger and stronger constraints on the true astrophysical sky. As such, each new experiment will then also in turn improve the instrumental calibration of all previous experiments.

The rest of this paper is organized as follows. In Sect. 2, we provide a brief review of the Bayesian end-to-end statistical framework used in this work, before describing the underlying data and computational expenses in Sect. 3. The main results, as defined by the global posterior distribution, are described in Sects. 4–6, summarizing instrumental parameters, frequency sky maps, and astrophysical results, respectively. In Sect. 7 we provide a discussion of systematic errors, while Sect. 8 discusses a few minor unresolved issues that should be addressed in future work. We conclude in Sect. 9, and lay a path forward for the COSMOGLOBE project.

2. End-to-end Bayesian CMB analysis

We begin by discussing the *WMAP* analysis from uncalibrated TOD to maps. Section 2.1 gives an overview of the BEYONDPLANCK project’s reanalysis of *Planck* LFI data, Sect. 2.2 provides a brief overview of the official *WMAP* pipeline, and Sect. 2.3 constructs the data model that is used in the end-to-end Gibbs sampling analysis.

2.1. LFI and BEYONDPLANCK

The BEYONDPLANCK project (BeyondPlanck 2022) was the first true application of end-to-end Gibbs sampling in the framework of CMB data analysis. The *Planck* Low Frequency Instrument data had been gradually improved through each *Planck* data release, specifically PR1 (Planck Collaboration II 2016), PR2 (Planck Collaboration II 2016), PR3 (Planck Collaboration II 2020), and PR4 (Planck Collaboration II 2016). Even after PR4, the LFI data still failed polarization null tests and contained visually striking poorly measured modes corresponding to relative gain uncertainty between different detectors. During the PR3 analysis, it became clear that there was a degeneracy between the assumption of the sky’s polarization and the gain differences.

The BEYONDPLANCK analysis generated the first clean LFI maps by Gibbs sampling the sky components and underlying instrumental parameters jointly (BeyondPlanck 2022; Galloway et al. 2022; Basyrov et al. 2022). The Commander3 pipeline was used to perform the low-level data analysis conditioned on a sky model that was created through component separation, and the reprocessed maps were used to perform component separation

once again. This Gibbs chain not only allowed for the true instrumental properties to be determined thus creating the best LFI maps to date – it fully explored the degeneracies between the low-level instrumental parameters themselves and our knowledge of the sky (Andersen et al. 2022; Svalheim et al. 2022).

2.2. Official WMAP pipeline

The *WMAP* satellite carried forty differential polarization-sensitive radiometers grouped as differencing assemblies (DAs), where one pair was sensitive to the difference in signal at one polarization orientation and the other pair sensitive to the orthogonal polarization. In total, the DAs were allocated as: 1 *K* (23 GHz), 1 *Ka* (30 GHz), 2 *Q* (40 GHz), 2 *V* (60 GHz), and 4 *W* (90 GHz).

The *WMAP* pointing solution was determined using the bore-sight vectors of individual feedhorns in spacecraft coordinates, in combination with on-board star trackers. Thermal flexure of the tracking structure introduced small pointing errors, as discussed by Jarosik et al. (2007). Using the temperature variation measured by housekeeping data, the quaternion pointing solution was corrected using a linear model that depends on arcsecond per temperature change. The residual pointing errors were computed using observations of Jupiter Saturn, and the reported upper limit was given by 10” (Bennett et al. 2013; Greason et al. 2012).

The *WMAP* bandpasses were measured directly pre-launch, sweeping a signal source through 201 frequencies and recording the output (Jarosik et al. 2003b). The bandpass responses have not been updated since the initial data release. However, as noted in Bennett et al. (2013), there has been an observed drift in the center frequency of *K*, *Ka*, *Q*, and *V*-band corresponding to a $\sim 0.1\%$ decrease over time. In practice, this did not affect the *WMAP* data processing because each year was mapped separately and co-added afterwards. An effective frequency calculator was delivered in the DR5 release as part of the IDL library to mitigate this effect during astrophysical analyses.²

The beams were characterized in the form of maps, with separate products for the near-field and far-field. The main beam and near sidelobes were characterized using a combination of physical optics codes and observations of Jupiter for each horn separately. The maps of Jupiter were then combined with the best-fit physical optics codes to create a map of the beam response (Hill et al. 2009; Weiland et al. 2011; Bennett et al. 2013). Far sidelobes were estimated using a combination of laboratory measurements and Moon data taken during the mission (Barnes et al. 2003), as well as a physical optics model describe in Hinshaw et al. (2009). To remove the far sidelobe in the TOD, an estimate was calculated by convolving the intensity map and the orbital dipole signal with the measured sidelobe signal (Jarosik et al. 2007). Although the sidelobe pickup was modeled in Barnes et al. (2003), it was determined that the results were small enough to be neglected, and have not been reported in any of the *WMAP* data releases.

The *WMAP* data were calibrated by jointly estimating the time-dependent gains and baselines, as describe in Hinshaw et al. (2007), Hinshaw et al. (2009), and Jarosik et al. (2011). The TOD are intially modelled as having constant gain and baseline for a 1–24 hour period, and are fit to the orbital dipole assuming T_0 from Mather et al. (1999) and a map made from a previous iteration of the mapmaking procedure. Once the gain and baseline

¹ <https://cosmoglobe.uio.no>

² https://lambda.gsfc.nasa.gov/product/wmap/dr5/m_sw.html

solution has converged, the data are fit to a parametric form of the radiometer performance as a function of housekeeping data, given in Appendix A of Greason et al. (2012).

Transmission imbalance, i.e., the effect of different sky signal transmission from the A-side and B-side optics, is parameterized using x_{im} , which is zero in the case of an ideal differential radiometer. In practice, an unpolarized sky map generates a timestamp

$$d_t^{\text{imbal}} \propto (1 + x_{\text{im}})T_{p_A} - (1 - x_{\text{im}})T_{p_B} \quad (1)$$

$$= (T_{p_A} - T_{p_B}) + x_{\text{im}}(T_{p_A} + T_{p_B}). \quad (2)$$

If the x_{im} value is inaccurate, this yields a spurious polarization component, and creates imbalance modes due to coupling with the Solar dipole (Jarosik et al. 2007). The transmission imbalance factors are fit by using the Solar dipole in TOD space and fitting the common-mode and differential signals in TOD space directly (Jarosik et al. 2003a, 2007).

Data are flagged and masked before the final mapmaking step. In particular, station-keeping maneuvers, solar flares, and unscheduled events caused certain data to be unusable – the full catalog of these events is listed in Table 1.8 of Greason et al. (2012). In addition, data are masked depending on the channel frequency and the planet itself, with the full list of exclusion radii enumerated in Table 4 of Bennett et al. (2013).

To create the sky maps, the calibrated data are put into the asymmetric mapmaking equation,

$$\mathbf{P}_{\text{am}}^T \mathbf{N}^{-1} \mathbf{P} \mathbf{m} = \mathbf{P}_{\text{am}}^T \mathbf{N}^{-1} \mathbf{d}, \quad (3)$$

where \mathbf{P} is implicitly defined for detectors \mathbf{d}_1 and \mathbf{d}_2 sensitive to different polarization orientations,

$$\begin{aligned} \mathbf{d}_1 &= \mathbf{P}_1 \mathbf{m} \\ &= (1 + x_{\text{im}})[T_A + Q_A \cos 2\gamma_A + U_A \sin 2\gamma_A + S_A] \\ &\quad + (1 - x_{\text{im}})[-T_B - Q_B \cos 2\gamma_B - U_B \sin 2\gamma_B - S_B] \end{aligned} \quad (4)$$

$$\begin{aligned} \mathbf{d}_2 &= \mathbf{P}_2 \mathbf{m} \\ &= (1 + x_{\text{im}})[T_A - Q_A \cos 2\gamma_A - U_A \sin 2\gamma_A - S_A] \\ &\quad + (1 - x_{\text{im}})[-T_B + Q_B \cos 2\gamma_B + U_B \sin 2\gamma_B + S_B] \end{aligned} \quad (5)$$

In this formalism, S acts as an extra Stokes parameter that absorbs the effects of different bandpass response between radiometers \mathbf{d}_1 and \mathbf{d}_2 (Jarosik et al. 2007). The asymmetric mapmaking matrix, \mathbf{P}_{am} , is used because, as noted in Jarosik et al. (2011), large signals observed in one beam can leak into the solution for the pixel observed by the other beam, leading to incorrect signals in the final map. The asymmetric mapmaking solution essentially works by only updating the matrix multiplication for beam A when beam A is in a high emission region and beam B is not, and vice versa. Bennett et al. (2013) also identified that these effects are pronounced when there is a steep gradient in the emission across the $N_{\text{side}} = 512$ pixels within an $N_{\text{side}} = 16$ superpixel, leading to excesses 140° away from the Galactic center.

An accurate noise model is necessary to perform the maximum likelihood mapmaking, as it requires the evaluation of \mathbf{N}^{-1} . The time-space autocorrelation function was estimated for each year of data, which is then Fourier transformed, inverted, and Fourier transformed again to create an effective inverse noise operator $\mathbf{N}_{tt'}^{-1}$. Finally, to create the sky maps themselves, the data are treated one year at a time, and the iterative Bi-conjugate Gradient Stabilized Method (BiCG-STAB van der Vorst 1992; Barrett et al. 1994) is applied to the maps.

2.3. Instrument model

As opposed to the *WMAP* pipeline, the *COSMOGLOBE* model involves creating a generative model for every aspect of the data, including the sky and instrumental effects at once. In the *COSMOGLOBE* paradigm, it is simplest to characterize the data's goodness-of-fit to a model,

$$\mathbf{d} = \mathbf{GP}[\mathbf{B}^{\text{symm}} \mathbf{Ma} + \mathbf{B}^{4\pi}(s^{\text{orb}} + s^{\text{fsl}})] + s^{\text{inst}} + \mathbf{n}^{\text{corr}} + \mathbf{n}^{\text{w}}, \quad (6)$$

where \mathbf{G} is the time-dependent gain in the form of the matrix $\text{diag}(g_t)$, \mathbf{P} is the $n_p \times n_t$ pointing matrix, \mathbf{B}^{symm} and $\mathbf{B}^{4\pi}$ are the symmetrized and full symmetric beam, respectively, \mathbf{M} is the mixing matrix between a given component c with spectral energy distribution $f_c(\nu/\nu_{0,c})$ and a detector j with bandpass $\tau_j(\nu)$, given by

$$M_{cj} = \int d\nu \tau_j(\nu) f_c(\nu/\nu_{c,0}). \quad (7)$$

The maps \mathbf{a} are the component amplitudes, s^{orb} is the orbital dipole induced by the motion of the telescope with respect to the Sun, and s^{fsl} is the time-dependent far sidelobe signal. In the *Commander3* (Galloway et al. 2022) implementation, \mathbf{n}^{corr} is a realization of the correlated noise component whose SED is parametrized by $P(f \mid \xi_n)$, where ξ_n generally includes f_{knee} , a slope α , and whose amplitude is fixed by the white noise σ_0 . Similarly, each experiment has particular signals that are specific to the instrument in question, e.g., the 1 Hz spike in *Planck* LFI or the large baseline in *WMAP*, which can be modeled by s^{inst} .

The most unique feature of the *WMAP* data is that it includes differential pointing. *WMAP* has two primary mirrors approximately reflected along the vertical satellite axis, and are tilted approximately 19.5° downwards – in total, when horn A is pointed at pixel p_A , horn B is pointed at a pixel p_B that is approximately 141° away (Page et al. 2003). The incoming radiation is differentiated in the electronics before being deposited on the detectors, essentially recording radiation proportional to $\mathbf{m}_A - \mathbf{m}_B$ and $\mathbf{m}_B - \mathbf{m}_A$ on the detectors (Jarosik et al. 2003b). Each pair of radiometers has a partner pair of radiometers that observes the same pixels with sensitivity to the orthogonal polarization direction. Taking these effects all into account, the total data model for a single radiometer is given by

$$d_t = g_t \mathbf{P}_{t,p} s_p + s_t^{\text{inst}} + n_t \quad (8)$$

$$\begin{aligned} &= g_t [\alpha_A(T_{p_A(t)} + Q_{p_A(t)} \cos 2\gamma_A(t) + U_{p_A(t)} \sin 2\gamma_A(t)) \\ &\quad - \alpha_B(T_{p_B(t)} + Q_{p_B(t)} \cos 2\gamma_B(t) + U_{p_B(t)} \sin 2\gamma_B(t))] \\ &\quad + s_t^{\text{inst}} + n_t \end{aligned} \quad (9)$$

where s_p is the total sky signal $\mathbf{B} \mathbf{M} \mathbf{a}$, $\gamma_{A/B}$ are the time-dependent polarization angles, and $p_{A/B}$ are the A and B pixel locations. In this notation, $\alpha_{A/B}$ is the total optical power transmission for horn A and B. Defining the transmission imbalance for a given radiometer pair $x_{\text{im}} \equiv (\alpha_A - \alpha_B)/(\alpha_A + \alpha_B)$ and absorbing $\alpha_A + \alpha_B$ into the definition of g_t allows the pointing operation to be written in terms of the deviation from ideality,

$$\begin{aligned} \mathbf{P}_{t,p} s_p &= (1 + x_{\text{im}})(T_{p_A} + Q_{p_A} \cos 2\gamma_A + U_{p_A} \sin 2\gamma_A) \\ &\quad - (1 - x_{\text{im}})(T_{p_B} + Q_{p_B} \cos 2\gamma_B + U_{p_B} \sin 2\gamma_B). \end{aligned} \quad (10)$$

2.4. Sky model

Following BeyondPlanck (2022), we assume that the sky can be modeled as a linear combination of CMB fluctuations, synchrotron, free-free emission, anomalous microwave emission,

thermal dust, and radio point sources. The parametric sky model we adopt is given in brightness temperature units as

$$s_{\text{RJ}} = (\mathbf{a}_{\text{CMB}} + \mathbf{a}_{\text{quad}}(\nu)) \frac{x^2 e^x}{(e^x - 1)^2} + \quad (11)$$

$$+ \mathbf{a}_s \left(\frac{\nu}{\nu_{0,s}} \right)^{\beta_s} + \quad (12)$$

$$+ \mathbf{a}_{\text{ff}} \left(\frac{\nu_{0,\text{ff}}}{\nu} \right)^2 \frac{g_{\text{ff}}(\nu; T_e)}{g_{\text{ff}}(\nu_{0,\text{ff}}; T_e)} + \quad (13)$$

$$+ \mathbf{a}_{\text{ame}} e^{\beta(\nu - \nu_{0,\text{ame}})} + \quad (14)$$

$$+ \mathbf{a}_d \left(\frac{\nu}{\nu_{0,d}} \right)^{\beta_d+1} \frac{e^{h\nu_{0,d}/k_B T_d} - 1}{e^{h\nu/k_B T_d} - 1} + \quad (15)$$

$$+ U_{\text{mJy}} \sum_{j=1}^{N_{\text{src}}} \mathbf{a}_{j,\text{src}} \left(\frac{\nu}{\nu_{0,\text{src}}} \right)^{\alpha_{j,\text{src}}-2}. \quad (16)$$

Note that the AME model we adopt is a pure exponential, rather than the SED template $s_0^{\text{sd}}(\nu)$ computed using SpDust2 (Ali-Haïmoud et al. 2009; Ali-Haïmoud 2010; Silsbee et al. 2011). The SpDust2 model was parameterized in BeyondPlanck (2022) by a peak frequency ν_p such that

$$s_{\text{RJ}}^{\text{sd}}(\nu) \propto \nu^{-2} s_0^{\text{sd}} \left(\nu \cdot \frac{30 \text{ GHz}}{\nu_p} \right). \quad (17)$$

In the *WMAP* and LFI frequency range, the exponential model and the SpDust2 are phenomenologically quite similar, despite their very different origins. The exponential model is a simple fit with β drawn from a prior value of -3.57 , and is a clear parametric form that is easy to interpret. An alternative model is the two-parameter log-normal AME SED,

$$s_{\text{RJ}}^{\text{ame,log-N}} = \mathbf{a}_{\text{ame}} \left(\frac{\nu}{\nu_{\text{ame}}} \right)^{-2} \exp \left(-\frac{1}{2} \left[\ln(\nu/\nu_{\text{ame}}) \right]^2 \right), \quad (18)$$

derived by Stevenson (2014) as an analytical approximation to the spinning dust emission. This has also been employed in the latest QUIJOTE analysis, e.g., Tramonte et al. (2023), as it allows for variation of the peak frequency ν_{ame} and width W_{ame} . Although this work is not dependent on the specific parametric form of the AME, we opt for the exponential form described above, as it provides an excellent fit to the diffuse AME with a single parameter.

2.5. Priors

2.6. Posterior distribution and Gibbs sampling

As shown in BeyondPlanck (2022), this parametric description of the instrumental effects and sky this parametric description of the instrumental effects and sky allows us to write down a total model for the data, $\mathbf{d} = \mathbf{s}^{\text{tot}}(\omega) + \mathbf{n}^w$, where \mathbf{s}^{tot} encompasses all of the terms in Eq. (6) except for the white noise term. Assuming that all instrumental effects have been modelled, the data should be Gaussian distributed with a mean of $\mathbf{s}^{\text{tot}}(\omega)$ and variance σ_0^2 . Given this model, we can evaluate the likelihood for arbitrary chunks of time-ordered data in the context of the entire model, so that individual chunks of data with poor fits can be more easily identified. In general, the likelihood is written

$$P(\mathbf{d} | \omega) \propto \exp \left(-\frac{1}{2} \sum_t \frac{(d_t - s_t^{\text{tot}}(\omega))^2}{\sigma_0^2} \right). \quad (19)$$

If $\mathbf{d} \sim \mathcal{N}(\mathbf{s}^{\text{tot}}, \sigma_0^2)$ is the correct model for the data, the argument of the exponent is proportional to a χ^2 -distribution with n_{TOD} degrees of freedom. In the limit of large n , a χ^2 distribution is well-approximated by a Gaussian with mean n and variance $2n$. Therefore we define and use the reduced- χ^2 statistic,

$$\chi^2 \equiv \frac{\sum_t ((d_t - s_t^{\text{tot}})^2 / \sigma_0^2 - n_{\text{TOD}})}{\sqrt{2n_{\text{TOD}}}}, \quad (20)$$

which is approximately drawn from the standard normal distribution $\mathcal{N}(0, 1)$.

The COSMOGLOBE Gibbs chain is given by

$$\mathbf{g} \leftarrow P(\mathbf{g} | \xi_n, s^{\text{inst}}, \beta, \mathbf{a}, C_\ell, \theta) \quad (21)$$

$$\mathbf{n}_{\text{corr}} \leftarrow P(\mathbf{n}_{\text{corr}} | \mathbf{g}, \xi_n, s^{\text{inst}}, \beta, \mathbf{a}, C_\ell, \theta) \quad (22)$$

$$\xi_n \leftarrow P(\xi_n | \mathbf{g}, \mathbf{n}_{\text{corr}}, s^{\text{inst}}, \beta, \mathbf{a}, C_\ell, \theta) \quad (23)$$

$$s^{\text{inst}} \leftarrow P(s^{\text{inst}} | \mathbf{g}, \mathbf{n}_{\text{corr}}, \xi_n, \beta, \mathbf{a}, C_\ell, \theta) \quad (24)$$

$$\beta \leftarrow P(\beta | \mathbf{g}, \mathbf{n}_{\text{corr}}, \xi_n, s^{\text{inst}}, C_\ell, \theta) \quad (25)$$

$$\mathbf{a} \leftarrow P(\mathbf{a} | \mathbf{g}, \mathbf{n}_{\text{corr}}, \xi_n, s^{\text{inst}}, \beta, C_\ell, \theta) \quad (26)$$

$$C_\ell \leftarrow P(C_\ell | \mathbf{g}, \mathbf{n}_{\text{corr}}, \xi_n, s^{\text{inst}}, \beta, \mathbf{a}, \theta) \quad (27)$$

$$\theta \leftarrow P(\theta | \mathbf{g}, \mathbf{n}_{\text{corr}}, \xi_n, s^{\text{inst}}, \beta, \mathbf{a}, C_\ell), \quad (28)$$

with each step requiring its own dedicated sampling algorithm, and in the case of BEYONDPLANCK, its own publication. The Commander3 pipeline is designed so that results of each Gibbs sample can be easily passed to each other, and that the internal calculations of each step do not directly depend on the inner workings of each other. Therefore, in order to add another data set to the Gibbs chain, one must implement Eqs. (21)–(24) for each instrument, as was done in BeyondPlanck (2022) and Basyrov et al. (2022) for *Planck* LFI and in Watts et al. (2022) for *WMAP*, or simply pass processed maps with beam, mask, and noise information to Eqs. (25)–(28), as was done for the Haslam 408 MHz map (Haslam et al. 1982; Remazeilles et al. 2015) and the *Planck* 353 and 857 GHz maps.

Before we discuss the results of this Gibbs chain as applied to the *Planck* LFI and *WMAP* data, we summarize the TOD processing steps in Sect. 2.7.

2.7. Sampling algorithms

Each step of the Gibbs chain requires its own distribution to be sampled from. In Sect. 2.7.1 we review the sampling algorithms implemented in the BEYONDPLANCK suite of papers, while Sects. 2.7.2–2.7.4 provide an overview of the *WMAP*-specific processing steps.

2.7.1. Review of sampling algorithms

Several of the techniques required for *WMAP* data analysis have already been implemented and described in the BEYONDPLANCK framework and implemented in Commander3. This section includes a summary of the algorithms that were used described previously for the analysis of LFI data. In each of these cases, every part of the model not explicitly mentioned is held fixed unless specified otherwise.

Noise estimation and calibration, described in Ihle et al. (2022) and Gjerløw et al. (2022) respectively, are highly degenerate, given that the timestream

$$d_{t,i} = g_{q,i} s_{t,i}^{\text{tot}} + n_{t,i}^{\text{corr}} + n_{t,i}^{\text{wn}} \quad (29)$$

is equally well fit by two solutions if $g' = gs^{\text{tot}}/(s^{\text{tot}})'$ or $(n^{\text{corr}})' = n^{\text{corr}} + gs^{\text{tot}} + g'(s^{\text{tot}})'$. In practice, this is dealt with by marginalizing over the correlated noise realization \mathbf{n}^{corr} assuming a fixed PSD ξ_n , so that Eqs. (21) and (22) are evaluated as

$$\mathbf{g} \leftarrow P(\mathbf{g} \mid \xi_n, \dots) \quad (30)$$

$$\mathbf{n}_{\text{corr}} \leftarrow P(\mathbf{n}_{\text{corr}} \mid \mathbf{g}, \xi_n, \dots). \quad (31)$$

This is allowed by probability theory given that the joint distribution $P(\mathbf{g}, \mathbf{n}_{\text{corr}} \mid \omega) = P(\mathbf{n}_{\text{corr}} \mid \mathbf{g}, \omega)P(\mathbf{g} \mid \omega)$, so that Eqs. (30) and (31) evaluated in sequence is equivalent to drawing a joint sample from $P(\mathbf{g}, \mathbf{n}_{\text{corr}} \mid \omega)$. In practice, this means that when sampling for \mathbf{g} , the covariance matrix $\mathbf{N} = \mathbf{N}_{\text{wn}} + \mathbf{N}_{\text{corr}}$ must be used, rather than just \mathbf{N}_{wn} .

Commander3 models the gain at each timestream t for a detector i as

$$g_{t,i} = g_0 + \Delta g_i + \delta g_{q,i} \quad (32)$$

where q labels the time interval for which we assume the gain is constant over, e.g., a single scan. In order to sample the gain, we write down a generative model for the TOD,

$$\mathbf{d}_i = \mathbf{g}_i s_i^{\text{tot}} + \mathbf{n}_i^{\text{tot}} \sim \mathcal{N}(\mathbf{g}_i s_i^{\text{tot}}, \mathbf{N}_i). \quad (33)$$

Since the \mathbf{d}_i is given as a linear combination of the fixed signal and the gains, a random sample of the gain can be drawn by solving³

$$[(s_i^{\text{tot}})^T \mathbf{N}_i^{-1} s_i^{\text{tot}}] \mathbf{g}_i = (s_i^{\text{tot}})^T \mathbf{N}_i^{-1} \mathbf{d}_i + (s_i^{\text{tot}})^T \mathbf{N}_i^{-1/2} \boldsymbol{\eta}. \quad (34)$$

Note that the \mathbf{N}_i depends implicitly on the noise PSD ξ_n , while the specific realization of \mathbf{n}_{corr} is accounted for in the covariance matrix. In practice, as shown in Gjerløw et al. (2022), **Commander3** samples g_0 , Δg_i , and $\delta g_{q,i}$ in separate sampling steps. Formally, the Gibbs chain is broken by fitting the absolute gain g_0 to the orbital dipole rather than the full sky signal. However, this makes the sampling much more robust to unmodelled systematic effects, so the trade-off in rigor is justified.

The correlated noise sampling, described in Ihle et al. (2022), follows a similar procedure to gain sampling, except now conditioned upon the gain estimate, sampled just before correlated noise in the code. Similar to the gain case, we can write a generative model for the data

$$\mathbf{d}_i = \mathbf{g}_i s_i^{\text{tot}} + \mathbf{n}_i^{\text{corr}} + \mathbf{n}_i^{\text{wn}} \sim \mathcal{N}(\mathbf{g}_i s_i^{\text{tot}}, \mathbf{N}_{\text{corr},i} + \mathbf{N}_{\text{wn},i}). \quad (35)$$

Given fixed $\mathbf{r}_i = \mathbf{d}_i - \mathbf{g}_i s_i^{\text{tot}}$, we can again write a sampling equation,

$$(\mathbf{N}_{\text{corr},i}^{-1} + \mathbf{N}_{\text{wn},i}^{-1}) \mathbf{n}_i^{\text{corr}} = \mathbf{N}_{\text{wn},i}^{-1} \mathbf{r}_i + \mathbf{N}_{\text{wn},i}^{-1/2} \boldsymbol{\eta}_1 + \mathbf{N}_{\text{corr},i}^{-1/2} \boldsymbol{\eta}_2. \quad (36)$$

This gives a sample of the true underlying correlated noise that occurred when the instrument was taking data. In practice, this is equivalent to the destriping mapmaking algorithm Madam, and returns equivalent results to the classical method (Keihänen et al. 2022).

To solve for the correlated noise parameters, we assume that the correlated noise is drawn from a correlated Gaussian and form the posterior distribution

$$P(\xi_n \mid \mathbf{n}^{\text{corr}}) \propto \frac{\exp[-\frac{1}{2}(\mathbf{n}^{\text{corr}})^T \mathbf{N}_{\text{corr}}^{-1} \mathbf{n}^{\text{corr}}]}{\sqrt{|\mathbf{N}_{\text{corr}}|}} P(\xi_n). \quad (37)$$

³ See, e.g., Appendix A.2 of BeyondPlanck (2022) for a derivation of this result.

The simplest parameterization for correlated noise is given by

$$\mathbf{N}_{\text{corr}}(f) = \sigma_0^2 \left(\frac{f}{f_{\text{knee}}} \right)^\alpha. \quad (38)$$

This can in principle be modified, and for *Planck* LFI a Gaussian log-normal bump was added at a late stage in the BEYOND-PLANCK analysis. Rather than sampling for σ_0 , we effectively fix the white noise level to the noise level at the highest frequency, e.g.,

$$\sigma_0^2 \equiv \frac{\text{Var}(r_{t+1} - r_t)}{2}, \quad (39)$$

where t and $t + 1$ are consecutive time samples, and $r \equiv \mathbf{d} - \mathbf{g}s^{\text{tot}} - \mathbf{n}^{\text{corr}}$. In practice, this makes σ_0 a deterministic function of the sampled sky and gain parameters. The parameters α and f_{knee} are not linear in the data, so must be sampled using the general inversion sampler.⁴ In practice, this requires gridding out the posterior one parameter at a time.

The bandpass mismatch is explicitly modeled in **Commander3**. Using the calibrated sky model, the expected calibrated sky signal is given by

$$m_{p,j} = \mathbf{B}_{p,p'} \sum_c \mathbf{M}_{c,j} a_{p'}^c + n_{j,p}^w. \quad (40)$$

Since $\mathbf{M}_{c,j}$ encodes the bandpass response of every detector j to every component c , the maps \mathbf{m}_j will each be slightly different depending on their bandpass τ_j . More importantly, differences in signal between different detectors can be attributed to a spurious polarization signal, giving spurious polarized maps. Therefore, before averaging different detectors together, **Commander3** estimates the average over all detectors in a given frequency channel $\mathbf{m} \equiv \langle \mathbf{m}_j \rangle$, and subtracts it directly in the timestream;

$$\delta s_{t,j}^{\text{leak}} = \mathbf{P}_{t,p}^j \mathbf{B}_{p,p'}^j (\mathbf{m}_{j,p'} - \mathbf{m}_{p'}). \quad (41)$$

This leakage term uses the expected bandpass

Once the instrumental parameters have been sampled, **Commander3** computes the calibrated TOD for each band,

$$r_{t,j} = \frac{d_{t,j} - n_{t,j}^{\text{corr}}}{g_{t,j}} - (s_{t,j}^{\text{orb}} + s_{t,j}^{\text{fsl}} + \delta s_{t,j}^{\text{leak}} + s_{t,j}^{\text{inst}}) \quad (42)$$

where s^{orb} is the orbital dipole, s^{fsl} is the far sidelobe timestream, δs^{leak} is the bandpass leakage, and s^{inst} is the set of instrumental parameters, e.g., the 1 Hz spike in LFI. With the a correlated noise realization removed, one can perform simple binned mapmaking, weighting each pixel by the white noise amplitude.

2.7.2. Differential mapmaking

The first additional algorithm that needed to be added to **Commander3** was differential mapmaking, since the *Planck* LFI data came from a standard single-horn instrument.

After calibration and correction for instrumental effects, the TOD can be modeled as

$$\mathbf{d} = \mathbf{P}\mathbf{m} + \mathbf{n}^w, \quad (43)$$

where

$$\mathbf{m} = \mathbf{B}^{\text{symm}} \mathbf{M} \mathbf{a} \quad (44)$$

⁴ See, e.g., Appendix A.3 of BeyondPlanck (2022) and Chapter 7.3.2 of Press et al. (2007) for further details.

is the expected map for each detector after removing the orbital dipole, far sidelobe, baseline, and a realization of correlated noise. The differential pointing strategy can be represented in matrix form as

$$\mathbf{P}_{tp} = (1 + x_{im})(\delta_{p^l p_A^l} + \delta_{p^o p_A^o} \cos 2\psi_A + \delta_{p^u p_A^u} \sin 2\psi_A) \quad (45)$$

$$- (1 - x_{im})(\delta_{p^l p_B^l} - \delta_{p^o p_B^o} \cos 2\psi_B - \delta_{p^u p_B^u} \sin 2\psi_B) \quad (46)$$

where p_A and p_B are the time-dependent pointings for each DA. The maximum likelihood map can in principle be solved using the usual mapmaking equation,

$$\mathbf{P}^T \mathbf{N}^{-1} \mathbf{P} \mathbf{m} = \mathbf{P}^T \mathbf{N}^{-1} \mathbf{d}. \quad (47)$$

For a single-horn experiment, i.e., *Planck* LFI, this reduces to a 3×3 matrix that can be inverted for each pixel independently. For the pointing matrix in Eq. (45), this is no longer possible, as there is inherently coupling between horns A and B in the timestreams. The $3N_{pix} \times 3N_{pix}$ matrix can be solved using an iterative algorithm, e.g., preconditioned conjugate gradients.

Jarosik et al. (2011) identified an issue where a large difference in the sky temperature at pixel value at pixel A versus pixel B induced artifacts in the mapmaking procedure. We adopt the procedure first described in Hinshaw et al. (2003) where only the pixel in a bright region, defined by a small processing mask (Bennett et al. 2013) is accumulated, thus modifying the mapmaking equation to

$$\mathbf{P}_{am}^T \mathbf{N}^{-1} \mathbf{P} \mathbf{m} = \mathbf{P}_{am}^T \mathbf{N}^{-1} \mathbf{d}. \quad (48)$$

This equation can be solved using the BiCG-STAB algorithm for a non-symmetric matrix \mathbf{A} where $\mathbf{A}\mathbf{x} = \mathbf{b}$. We apply a preconditioner \mathbf{M} by numerically inverting the same problem with $N_{side} = 16$ maps and applying a diagonal noise matrix. Numerically, we define convergence as when the residual $\mathbf{r} \equiv \mathbf{b} - \mathbf{A}\mathbf{x}$ satisfies $\mathbf{r}^T \mathbf{M}^{-1} \mathbf{r} / \mathbf{b}^T \mathbf{M}^{-1} \mathbf{b} < 10^{-10}$, which typically takes about 20 iterations for producing frequency maps.

2.7.3. Transmission imbalance estimation

Transmission imbalance, i.e., the differential power transmission of the optics and waveguide components, can be parameterized as

$$d_{t,j} = g_{t,j}[(1 + x_{im,j})s_{t,j}^{tot,A} - (1 - x_{im,j})s_{t,j}^{tot,B}] + n_t. \quad (49)$$

This can be decomposed into a differential (d) and common-mode (c) signal such that

$$d_{t,j} = g_{t,j}[s_{t,j}^d + x_{im,j}s_{t,j}^c] + n_t. \quad (50)$$

In this form, the imbalance parameters can be estimated by drawing Gaussian samples from the standard mean and standard deviation over the entire mission. To draw samples for $x_{im,j}$, we construct the sampling routine analogous to Eqs. (34) and (36) with $\mathbf{r} = \mathbf{d} - \mathbf{gs}^d$,

$$[(\mathbf{gs}^c)^T \mathbf{N}^{-1} \mathbf{gs}^c]x_{im} = (\mathbf{gs}^c)^T \mathbf{N}^{-1} \mathbf{r} + (\mathbf{gs}^c)^T \mathbf{N}^{-1/2} \boldsymbol{\eta}, \quad (51)$$

essentially cross-correlating the common-mode signal with \mathbf{r} with appropriate weights and adding a Gaussian random variable with the correct weighting. Note that we are marginalizing over the correlated noise here by using $\mathbf{N} = \mathbf{N}_{wn} + \mathbf{N}_{corr}$. This mitigates any baseline drifts being erroneously attributed to the common-mode signal and biasing the estimate of x_{im} .

The WMAP procedure, described in Jarosik et al. (2003a), fit for common-mode and differential coefficients along with a cubic baseline over 10 precession periods at a time, corresponding to 10 hours of observation. The mean and uncertainty were then calculated by averaging and taking the standard deviation of these values. This approach has the benefit of allowing for the tracking of possible transmission imbalance variation throughout the mission. However, none of the WMAP suite of papers have indicated this, and it has not arisen in our analysis, so we model this as an effect whose value is constant throughout the mission.

2.7.4. Baseline sampling

The data model adopted in Hinshaw et al. (2003) can be written in raw digital units (du) as

$$= GPB \mathbf{M} \mathbf{a} + \mathbf{n} + \mathbf{b}, \quad (52)$$

where \mathbf{b} is the instrumental baseline and \mathbf{n} is the total instrumental noise. As detailed in Ihle et al. (2022), Commander3 divides the noise into $\mathbf{n} = \mathbf{n}^w + \mathbf{n}^{corr}$, a white noise term and a correlated noise term. By definition, the white noise does not have any correlations between adjacent pixels, so that any pixel-pixel covariance should be fully described by realizations of the \mathbf{n}^{corr} timestream.

Commander estimates the baseline using the full estimate of the current sky model, $\mathbf{r} = \mathbf{d} - \mathbf{gs}^{tot} = \mathbf{b} + \mathbf{n}$. Modeling $\mathbf{b} = b_0 + b_1 \Delta t$, we solve for b_0 and b_1 using linear regression in each timestream while masking out samples that lie within the processing mask. Strictly speaking, this is breaking the Gibbs chain, as we are not formally sampling b_0 and b_1 for each TOD chunk. In practice, baseline estimation uncertainty propagates to correlated noise realizations and PSD parameters, as discussed below.

The approach detailed in Hinshaw et al. (2003) and the Commander implementation differ mainly in the assumed stable timescale – the initial WMAP baseline is estimated over one hour timescales, whereas Commander assumes constant values throughout the entire timestream, 3–7 days depending on the band in question. As noted in Hinshaw et al. (2003), residual baseline variations manifest as correlated noise stripes in the final maps. WMAP9 solves this using a time-domain filter, downweighting the data based off of the noise characterization. This approach is equivalent to the Commander3 procedure of removing a constrained realization of correlated noise from the timestream directly, based on the best-fit to the noise PSD.

3. Data and data processing

We describe the delivered WMAP data in Sect. 3.1, then describe the treatment we apply it to make them compatible with Commander3 in Sect. 3.2, then describe the computational requirements in Sect. 3.3.

3.1. Publicly available WMAP products

The full WMAP dataset is hosted at the Legacy Archive for Microwave Background Data Analysis (LAMBDA).⁵ In addition to the primary scientific products, e.g., cosmological parameters, CMB power spectra and anisotropy maps, and frequency maps,

⁵ https://lambda.gsfc.nasa.gov/product/wmap/dr5/m_products.html

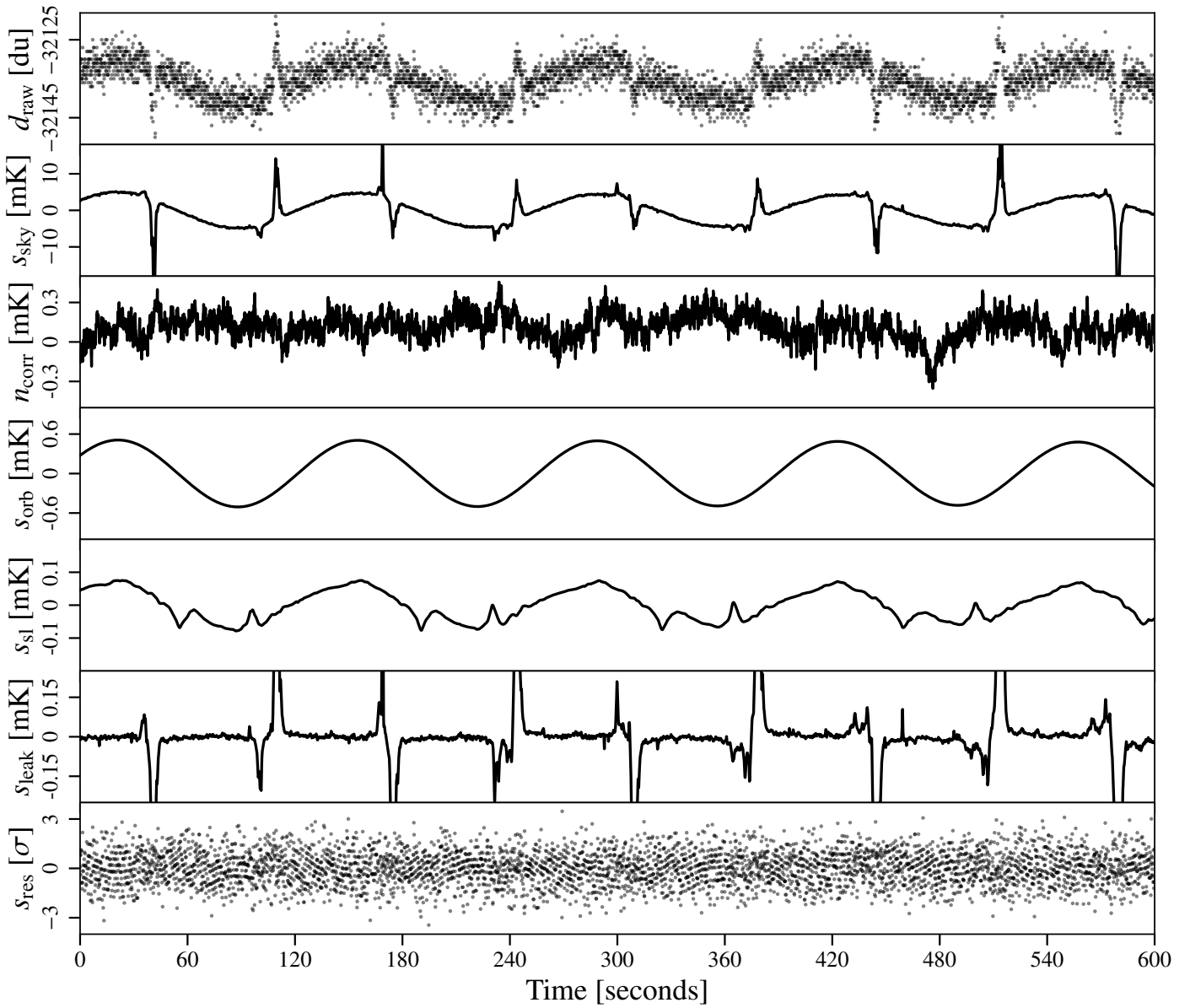


Fig. 1. Each of the timestreams that go into the model. Note the varying dynamic ranges of each plot.

the time-ordered data (TOD) can be downloaded, both in uncalibrated and calibrated form.⁶ In principle, thanks to these data and the explanatory supplements (Greason et al. 2012), the entire data analysis pipeline can be reproduced from TOD in digital units (du) to frequency maps.

For this analysis, we keep certain instrumental parameters fixed to the reported values. For example, we have made no attempts to rederive the pointing solutions, re-estimate the main beam response and far sidelobe pickup, or recover data that was flagged in the *WMAP* event log. These and other analyses, such as estimating the bandpass shift over the course of the mission, are certainly possible within the larger Gibbs sampling framework. However, in this work we limit ourselves to recalibrating the TOD, estimating the noise properties, and applying bandpass corrections to the data before mapmaking.

Table 1. Flagging statistics

Band	Flagged (%)	Discarded (%)	Used (%)
<i>K</i>	1.72	0.87	97.4
<i>Ka</i>	1.64	0.88	97.5
<i>Q1</i>	1.84	0.84	96.5
<i>Q2</i>	1.62	0.81	97.6
<i>V1</i>	1.62	1.10	97.3
<i>V2</i>	1.61	1.01	97.4
<i>W1</i>	1.76	1.03	97.2
<i>W2</i>	1.60	0.81	97.6
<i>W3</i>	1.61	0.87	97.5
<i>W4</i>	1.60	0.81	97.6

3.2. TOD pre-processing and data selection

The full nine-year *WMAP* archive spans from August 10, 2001 to August 10, 2010, with the raw uncalibrated data spanning 626 GB. A little over 1 % of the data were lost or rejected due to

⁶ https://lambda.gsfc.nasa.gov/product/wmap/dr5/tod_info.html

incomplete satellite telemetry, thermal disturbances, spacecraft anomalies, and station-keeping maneuvers, with an extra 0.1 % rejected due to planet flagging (Bennett et al. 2003b; Hinshaw et al. 2007, 2009; Bennett et al. 2013). The final results reported in Bennett et al. (2013) included roughly 98.4 % of the total data volume. A full accounting of all data cuts can be found in Table 1.8 of Greason et al. (2012). In total, we flag the same data indicated in the fiducial *WMAP* analysis, and use the same planet flags.

As shown in Galloway et al. (2022), a large fraction of Commander3’s computational time is spent performing FFTs on individual scans. Rather than truncating datastreams to have lengths equal to “magic numbers” for which FFTW (Frigo & Johnson 2005) is fastest, as in Galloway et al. (2022), we split the data into scans of length 2^N , where $N = 22$ for $K-Q$, $N = 23$ for $V-W$. This yields scans with lengths of 6.21 days for K - and Ka -band, 4.97 days for Q -band, 7.46 days for V -band, and 4.97 days for W -band. These datastream lengths are short enough to be processed quickly and distributed efficiently across multiple processors, while being long enough to properly characterize the noise properties of the timestreams, whose f_{knee} ’s are on the order 1 mHz. Most importantly, FFTW performs fastest when the datastream is of length 2^N .

When rechunking the data, timestreams of length 2^N were interrupted by events logged in Table 1.8 of Greason et al. (2012). When we encountered these events, TOD segments that were interrupted by the event were appended to the previous TOD, in most cases creating TODs with lengths $> 2^N$. We found that events of length $< 2^N$ were too short to accurately estimate the noise PSD parameters. This criterion led us to discard these otherwise useful data. In addition, when $> 10\%$ of the TOD was flagged, the large number of gaps in the data made the constrained realizations unreliable, as well as biasing the noise PSD parameters. Together, these two effects led to $\simeq 1\%$ of the data to be discarded despite being of acceptable quality. We present the full flagging statistics for our maps in Table 1. In total, the COSMOGLOBE maps use slightly less data than the *WMAP9* official products, which had a total efficiency of $\simeq 98.4\%$ (Bennett et al. 2013). The total difference in data volume can be entirely accounted for by the cuts described in this paragraph.

3.3. Computational resources

A key motivation of the COSMOGLOBE project is to evaluate whether it is feasible to perform a joint analysis of two datasets simultaneously, each with its own particular processing requirements and algorithmic treatment. One of the results from Watts et al. (2022) was that most of the data processing procedures for *WMAP* and *Planck* LFI overlapped, with the notable exception of mapmaking. While the algorithmic requirements have been discussed in Sect. 2, we have not yet quantified the requirements in terms of RAM and CPU hours. In Table 2, we enumerate the RAM requirements and CPU time for each sampling step using the local cluster at the Institute of Theoretical Astrophysics at the University of Oslo. The node that these numbers come from used 128 cores of an AMD EPYC 7H12, 2.6 GHz machine with 2 TB of memory. As Commander3 is parallelized and used 128 cores, wall hours in Table 2 can be obtained by dividing by 128.

Despite the relatively small data volume spanned by *WMAP*, the CPU time is comparable to each of the LFI channels. By far the largest reason for this is the mapmaking step, which requires looping over the entire dataset for each matrix multiplication, a process which must be repeated ~ 20 times. This is vastly sped

up by the use of a low resolution preconditioner, reducing the number of iterations by an order of magnitude.

Additionally, operations that require creating timestreams for each detector, i.e., TOD projection, sidelobe evaluation, and orbital dipole projection, take much longer than expected from a pure data volume scaling. Part of this is due to each *WMAP* radiometer needing to evaluate the sky in two pixels simultaneously, doubling the expected workload. The operations of gain sampling and correlated noise sampling include multiple FFTs. Typical LFI TODs are of length $\sim 200\,000$, an order of magnitude smaller than the *WMAP* TODs of length 2^{22-23} .

4. Instrumental parameters

4.1. Trace plots and correlations

To illustrate the dependence of the goodness-of-fit on the noise model, we inspect the 50th TOD segment, corresponding to MJDs 52285.2–52290.6, as a function of Gibbs iteration, in Fig. 3. This is one of the worst-fitting TOD segments of the entire mission, with a reduced relative χ^2 of -7.5 , equivalent to $\chi^2/n = 0.993$. The line plots demonstrate a strong correlation between the noise parameters and the χ^2 , while the gain itself is almost completely uncorrelated with the variations in the χ^2 . As σ_0 is not formally sampled in the Gibbs chain, it is weakly dependent on f_{knee} and α , making it more likely that it is the driver of the correlations in this figure.

4.2. Gain and baselines

To compare the calibrated TODs from *WMAP* versus COSMOGLOBE, it is important to look at the *WMAP* gain model,

$$g = \alpha \frac{\bar{V} - V_0 - \beta(T_{\text{RXB}} - 290 \text{ K})}{T_{\text{FPA}} - T_0} + (m\Delta t + c), \quad (53)$$

where α , V_0 , β , T_0 , m , and c are fit to a constant value across the mission for each radiometer. \bar{V} are radio frequency bias powers per detector, and T_{RXB} and T_{FPA} are the receiver box and focal plane assembly temperatures, which are recorded every 23.04 s. Evaluating the model as a function of T_{RXB} and T_{FPA} requires finding the housekeeping data for the thermistor that was physically closest to the relevant radiometer’s focal plane on the satellite. As this requires detailed technical information about the specifications of the satellite’s schematics layout that can easily be misunderstood, we do not attempt to reproduce the gain model given in Eq. (53) in this work. Although we are unable to reproduce the exact gain model parametrized in Greason et al. (2012), the 23.4 s time dependence of the gain model on housekeeping data is a plausible explanation for the time-dependent noise variation in the different calibrated data solutions.

As reported in Hinshaw et al. (2007), the calibrated data archive has been calibrated using the procedure listed above, with a baseline subtracted each hour and the sidelobe subtracted. Figure 5 shows the COSMOGLOBE timestream $\mathbf{d}/g - \mathbf{s}_{\text{sl}} - \mathbf{b}$ with the *WMAP* delivered calibrated signal subtracted. The most prominent feature is a $\sim 25 \mu\text{K}$ offset, which is unsurprising, given the different treatment of baselines in our two pipelines. The second obvious difference is a series of spikes associated with Galactic plane crossings. The differences of order $50 \mu\text{K}$ correspond to sky brightness of order 10 mK , equivalent to $\sim 0.5\%$ deviations in the gain solution. This is twice as large as the 0.2% uncertainty estimated in Bennett et al. (2013) based on end-to-end simulations.

Table 2. Computational resources required for end-to-end COSMOGLOBE processing. All times correspond to CPU hours, and all data volumes are reported in GB. Reported times are averaged over more than 100 samples, and vary by $\lesssim 5\%$ from sample to sample.

ITEM	30	44	70	K	Ka	$Q1$	$Q2$	V1	V2	W1	W2	W3	W4	SUM	
<i>Data volume</i>															
Compressed TOD volume	86	178	597	13	12	15	15	19	18	26	26	26	26	1 053	
<i>Processing time (cost per run)</i>															
TOD initialization/IO time	1.8	2.5	9.3	0.3	0.3	0.4	0.4	0.4	0.4	0.5	0.5	0.5	0.5	17.8	
Other initialization														13.4	
Total initialization														31.2	
<i>Gibbs sampling steps (cost per sample)</i>															
Huffman decompression	1.1	2.1	10.5	0.9	0.8	1.0	1.0	1.3	1.3	1.8	1.8	1.8	1.8	27.2	
TOD projection (P operation)	0.4	0.9	4.2	2.6	2.6	3.3	3.4	4.3	4.3	6.4	6.3	6.3	6.4	54.0	
Sidelobe evaluation	1.0	2.1	7.6	2.9	2.9	3.5	3.5	4.7	4.8	7.0	6.9	6.9	6.9	60.7	
Orbital dipole	0.9	1.9	7.1	1.3	1.3	1.7	1.7	2.2	2.3	3.4	3.3	3.3	3.3	33.7	
Gain sampling	0.5	0.8	1.9	0.8	0.8	0.5	0.5	0.9	0.9	0.7	0.7	0.7	0.7	10.4	
1 Hz spike sampling	0.3	0.4	1.6											2.4	
Correlated noise sampling	2.0	4.0	21.7	2.8	2.9	3.3	3.6	5.1	5.4	8.0	7.7	7.2	8.5	81.3	
Correlated noise PSD sampling	4.8	5.9	1.5	0.2	0.2	0.3	0.3	0.5	0.4	0.7	0.6	0.6	0.7	16.7	
TOD binning (P' operation)	0.1	0.1	4.0	0.5	0.5	0.7	0.8	0.8	0.8	1.2	1.2	1.2	1.2	13.1	
Mapmaking						6.4	7.0	8.9	8.1	11.1	9.5	14.4	14.3	15.3	119.5
Sum of other TOD processing	4.4	8.6	44.4	14.7	4.6	5.1	5.0	9.4	7.7	8.1	6.8	8.6	8.7	136.1	
TOD processing cost per sample	15.5	26.8	104.5	23.0	24.1	27.6	27.9	40.3	37.4	51.7	50.6	51.9	54.6	535.9	
Amplitude sampling														14.0	
Spectral index sampling														25.5	
Total cost per sample														581.2	

On longer timescales, as displayed in Figure 6, the most prominent feature is a varying signal of amplitude 0.2 mK. This likely due to the hourly baseline subtraction mentioned above, which contrasts with the COSMOGLOBE approach of assigning a linear baseline solution for the entire scan. The variations are commensurate with correlated noise, which for K113 has $f_{\text{knee}} \sim 0.5$ mHz, corresponding to a little over half an hour. Therefore, the hourlong baseline subtraction essentially acts as a destriper, removing an estimate of the correlated noise. To test this hypothesis, we plot a realization of correlated noise generated by Commander, and find that the signals are very similar, both in amplitude and morphology.

We also compare the gain and baseline solutions throughout the course of the mission in Fig. 2. To recover the WMAP9 gain solution, we directly compare the uncalibrated WMAP data with the calibrated WMAP data with a far sidelobe contribution convolved with the delivered WMAP9 DA maps. We find that the calibrated and uncalibrated data can be related by

$$d_t^{\text{raw}} = g(d_t^{\text{cal}} + s_t^{\text{sl}}) + \sum_{i=0}^3 c_i(t - t_0)^i. \quad (54)$$

We find that d_t^{raw} is consistent with the expression on the right at the level of < 0.1 du for all radiometers, suggesting that this estimate of g and the baseline c_0 is a good approximation of the WMAP9 calibration solution. An initial estimate using a linear baseline gave an unacceptably poor fit. Given that Eqn. (2) of Jarosik et al. (2003a) employed a cubic baseline fit while fitting for transmission imbalance parameters, it is reasonable to assume that the official calibrated archive was created using a similar procedure.

The morphological characteristics of the WMAP9 and COSMOGLOBE gain solutions are similar, with a general trend to increase with time. Both solutions also follow a sinusoidal pattern, corresponding to temperature change due to L2's motion

around the Sun (Greasen et al. 2012). However, we do find the amplitude of the COSMOGLOBE K -band gain is slightly lower than the WMAP9 solution, and with fewer oscillatory features. Other than the absolute calibration shift in K -band, the gains are consistent between COSMOGLOBE and WMAP9 within 1 %. For completeness, the full gain comparisons can be found in Fig. A.3.

4.3. Transmission imbalance

The transmission imbalance parameters x_{im} are crucial to measure correctly because their mis-estimation can induce a large polarized signal that is coupled to the Solar dipole (Jarosik et al. 2007; Watts et al. 2022). The uncertainty in x_{im} was quoted as the source of large-scale polarized features in the WMAP9 maps, and a template of this effect was explicitly projected out in the pixel-space polarized covariance matrix.

We find x_{im} values that are largely consistent with the values reported in Bennett et al. (2013), albeit with some outliers. We find in general that the 68 % confidence intervals from COSMOGLOBE are smaller than the fiducial values, although we caution against a direct comparison of these values since such different procedures were used for estimating the uncertainties.

4.4. Instrumental noise and goodness-of-fit

The noise fitting, as outlined in Sect. 2.7, inherently depends the data being fit well by both the sky model and the instrument model. In practice, correlated noise fitting can model any unmodelled signals, so the power spectrum and TODs must be carefully scrutinized before any conclusions can be made about the corresponding maps.

The white noise level in raw du is not strictly sampled, but is estimated conditioned on the instrumental parameters and the sky parameters. However, the calibrated white noise level

Table 3. Summary of noise properties.

Radiometer ..	Diode	Sensitivity, σ_0 (mK \sqrt{s})			Knee frequency, f_{knee} (mHz)			Slope, α
		GSFC	WMAP	CG/ $\sqrt{2}$	GSFC	WMAP	CG/ $\sqrt{2}$	
K11	1	0.72	0.66	0.704 ± 0.002	6.13	0.4	0.82 ± 0.20	-1.01 ± 0.10
	2			0.708 ± 0.003			0.63 ± 0.14	-0.95 ± 0.10
K12	1	0.87	0.75	0.796 ± 0.004	5.37	0.51	0.42 ± 0.19	-0.93 ± 0.12
	2			0.780 ± 0.005			0.71 ± 0.15	-1.02 ± 0.10
Ka11	1	0.75	0.71	0.788 ± 0.001	1.66	0.71	1.20 ± 0.22	-1.02 ± 0.09
	2			0.777 ± 0.001			1.19 ± 0.22	-1.02 ± 0.09
Ka12	1	0.77	0.72	0.788 ± 0.003	1.29	0.32	0.62 ± 0.16	-0.99 ± 0.11
	2			0.784 ± 0.001			0.63 ± 0.13	-1.01 ± 0.11
Q11	1	0.99	0.92	0.998 ± 0.002	3.21	1.09	1.06 ± 0.16	-1.09 ± 0.09
	2			0.992 ± 0.002			1.06 ± 0.16	-1.10 ± 0.09
Q12	1	0.95	1.02	1.159 ± 0.007	3.13	0.35	0.45 ± 0.47	-0.98 ± 0.11
	2			1.146 ± 0.007			0.83 ± 0.14	-1.00 ± 0.09
Q21	1	0.89	0.85	0.908 ± 0.002	1.92	5.76	2.88 ± 0.37	-1.10 ± 0.07
	2			0.906 ± 0.002			3.22 ± 0.56	-1.10 ± 0.06
Q22	1	1.04	0.99	1.074 ± 0.004	4.61	8.62	3.95 ± 0.54	-1.11 ± 0.06
	2			1.064 ± 0.003			4.05 ± 0.64	-1.11 ± 0.06
V11	1	1.25	1.22	1.551 ± 0.003	2.56	0.09	1.27 ± 0.15	-0.90 ± 0.06
	2			1.539 ± 0.003			1.19 ± 0.14	-0.89 ± 0.06
V12	1	1.07	1.11	1.398 ± 0.002	4.49	1.41	2.11 ± 0.20	-0.97 ± 0.05
	2			1.432 ± 0.002			1.88 ± 0.17	-0.96 ± 0.05
V21	1	1.01	0.97	1.241 ± 0.298	2.43	0.88	1.50 ± 0.24	-0.95 ± 0.07
	2			1.217 ± 0.294			1.60 ± 0.26	-0.97 ± 0.06
V22	1	1.13	1.1	1.443 ± 0.300	3.06	8.35	4.01 ± 0.85	-1.00 ± 0.08
	2			1.415 ± 0.316			3.08 ± 0.65	-1.01 ± 0.08
W11	1	1.18	1.35	1.938 ± 0.005	16.2	7.88	5.59 ± 0.53	-0.94 ± 0.05
	2			1.895 ± 0.005			8.99 ± 0.85	-0.95 ± 0.04
W12	1	1.41	1.61	2.301 ± 0.005	15.1	0.66	3.91 ± 0.42	-0.89 ± 0.05
	2			2.345 ± 0.006			4.81 ± 0.53	-0.89 ± 0.05
W21	1	1.38	1.61	2.225 ± 0.007	1.76	9.02	13.57 ± 1.47	-0.89 ± 0.03
	2			2.292 ± 0.006			5.06 ± 0.95	-0.93 ± 0.05
W22	1	1.44	1.72	2.291 ± 0.006	0.77	7.47	3.02 ± 0.53	-0.98 ± 0.05
	2			2.232 ± 0.007			7.26 ± 1.05	-0.95 ± 0.04
W31	1	1.47	1.65	2.328 ± 0.005	1.84	0.93	1.30 ± 0.46	-0.99 ± 0.07
	2			2.322 ± 0.006			1.97 ± 0.28	-0.98 ± 0.06
W32	1	1.69	1.86	2.707 ± 0.015	2.39	0.28	1.59 ± 0.29	-0.98 ± 0.07
	2			2.579 ± 0.015			1.40 ± 0.39	-1.00 ± 0.07
W41	1	1.6	1.71	2.519 ± 0.010	8.46	46.5	26.81 ± 1.83	-0.92 ± 0.04
	2			2.479 ± 0.009			24.75 ± 1.63	-0.92 ± 0.04
W42	1	1.43	1.65	2.221 ± 0.017	5.31	26.0	16.10 ± 1.09	-0.94 ± 0.04
	2			2.202 ± 0.015			17.11 ± 1.19	-0.94 ± 0.04

$\sigma_0[\text{K}] = \sigma_0[\text{du}]/g$ does depend on the gain quite directly, which allows us to test the effects of the calibration on the instrument sensitivity itself. The calibrated white noise level follows a biaurnal trend indicative of a system temperature variation, which is to be expected given the radiometer equation

$$\sigma_0[\text{V}] \propto gT_{\text{sys}}. \quad (55)$$

Aside from an overall amplitude shift due to the absolute calibration variation, the shape of the white noise level is stable throughout the Gibbs chain.

The knee frequencies for each channel lie between the reported values in Jarosik et al. (2003a) for both the Goddard Space Flight Center (GSFC) laboratory measurements and those from the first year of data collection. Nearly all radiometers have constant f_{knee} throughout the mission, with a few notable exceptions. First, all W -band channels display some amount of temporal variation that does not seem to be associated with any sinusoidal features. Second, all $Q2$ channels, $V223$, and $V224$ all display a similar asymptotic drift in time. We have not found any

instrumental effects that share this feature. The PSD slope α is around -1 for each radiometer, albeit with high scatter for the lower frequencies. As expected, the uncertainty in α decreases as f_{knee} increases, since there are more datapoints to fit below f_{knee} where the constraining power on α is the strongest.

The most striking feature of the reduced normalized χ^2 is its amplitude and its semiannual periodicity. Given the noise model and data residual, we can evaluate the goodness-of-fit in the form of the relative χ^2 . Here, we find that approximately half of the radiometers have a χ^2 value at least 6σ above or below the expected value. Given perfect Gaussian residuals, we would expect the reduced sum of squares to be $n_{\text{TOD}} = 2^N$ and be within $\sqrt{2n_{\text{TOD}}} = 2^{(N+1)/2}$ 68 % of the time. For a typical W -band scan of length $n_{\text{TOD}} = 2^{22}$, a 10σ model failure corresponds to $\chi^2/n_{\text{TOD}} = 1.003$. Therefore, it is exceedingly difficult to look at any given $WMAP$ scan in the time domain and identify a model failure. In power spectrum space, i.e., in Fig. 8, the data are still characterized well at all scales, despite this scan having a χ^2 7 σ above the expectation value.

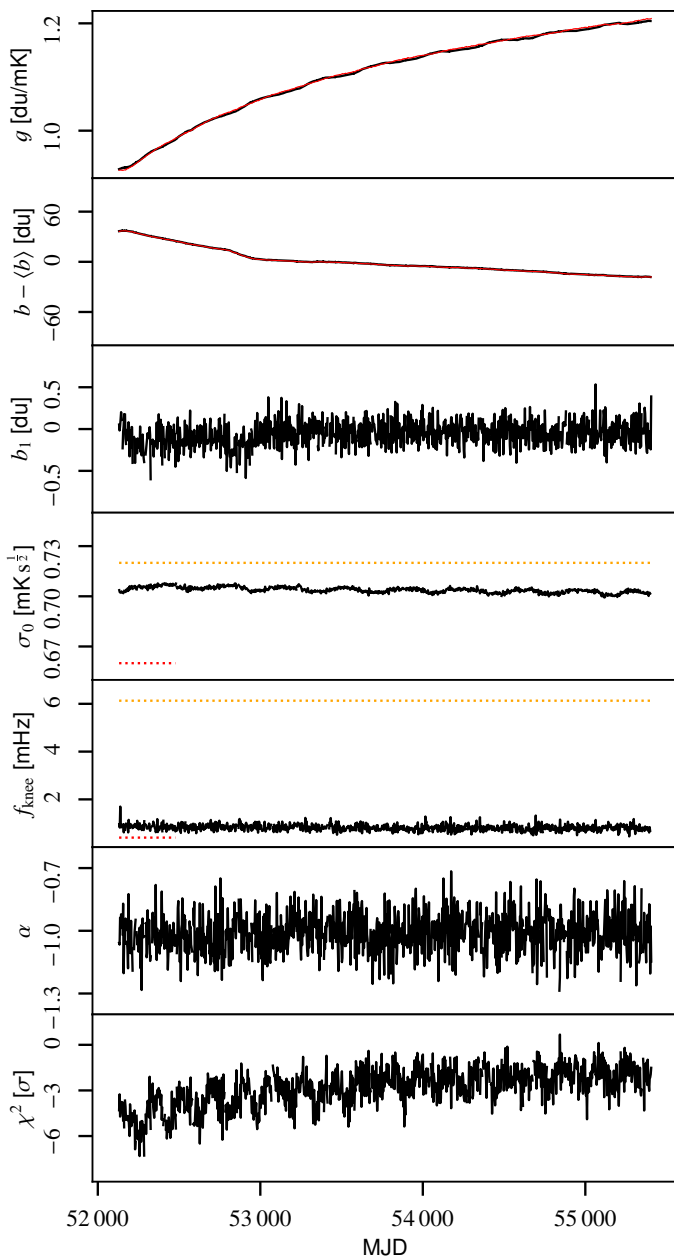


Fig. 2. Overview of *K113*. The red solid lines in first and second panel are the delivered gain and baselines from *WMAP9*, while the black lines in all panels are samples from the COSMOGLOBE Gibbs chain. The red dashed and yellow dashed lines are reported σ_0 and f_{knee} values from the first-year *WMAP* data analysis and GSFC measurements, respectively.

Only with aggressive smoothing, as in Fig. 9, does the model failure become apparent at frequencies 1–10 Hz. Here, it is clear that despite fitting the data well at the highest and lowest frequencies, it is in the intermediate range of 1–5 Hz where the power spectrum is a less accurate fit to the power spectrum. Part of the cause of this failure is that the white noise level is essentially fixed by the value of the power spectrum at the Nyquist frequency, as it was computed by differencing adjacent samples. The power spectrum has a downward trend beyond above 1 Hz, indicating that the data would be better fit by one or more terms proportional to f^α . This is phenomenologically similar to the *WMAP* collaboration’s approach of describing the time-space autocorrelation as a cubic polynomial in $\log \Delta t$ (Jarosik et al. 2007).

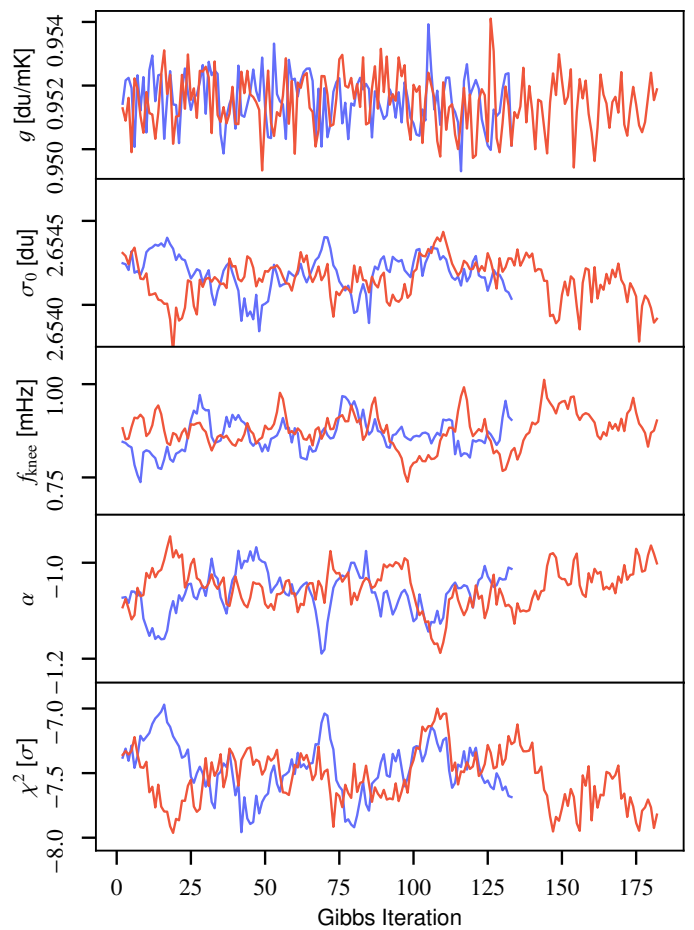


Fig. 3. Subset of *K113* Gibbs samples for both chains, arbitrarily colored red and blue. The parameters correspond to MJDs 52285.2–52290.6.

In practice, the $1/f$ model has a small effect on the final data products, and was not visible in noise models when we modeled the data in one day scans rather than the longer 3–7 day scans due to the lower n_{TOD} giving a higher uncertainty on the relative χ^2 . Therefore, although this strictly constitutes a deficiency in the model, it is in practice too small to affect the results of the rest of the chain. The downturn of the noise PSD at high frequencies is also present in, e.g., the *Planck* HFI data (Planck Collaboration Int. XLVI 2016, Fig. 1), so improved modelling of this form will be a necessity in future COSMOGLOBE endeavors, and will be used to improve the *WMAP* data processing.

4.5. Astrophysical sky model

Given the frequency maps,⁷ we can determine the component’s amplitude maps as part of the Gibbs chain. Due to the high signal-to-noise of the *K*-band map, which was not used in the BeyondPlanck (2022) for this reason, the spectral indices were not fit in this chain but rather drawn from prior distributions.

Fusce mauris. Vestibulum luctus nibh at lectus. Sed bibendum, nulla a faucibus semper, leo velit ultricies tellus, ac venenatis arcu wisi vel nisl. Vestibulum diam. Aliquam pellentesque, augue quis sagittis posuere, turpis lacus congue quam, in hendrerit risus eros eget felis. Maecenas eget erat in sapien mattis

⁷ As the maps are deterministic functions of the instrumental parameters, they are discussed in Sect. 5.

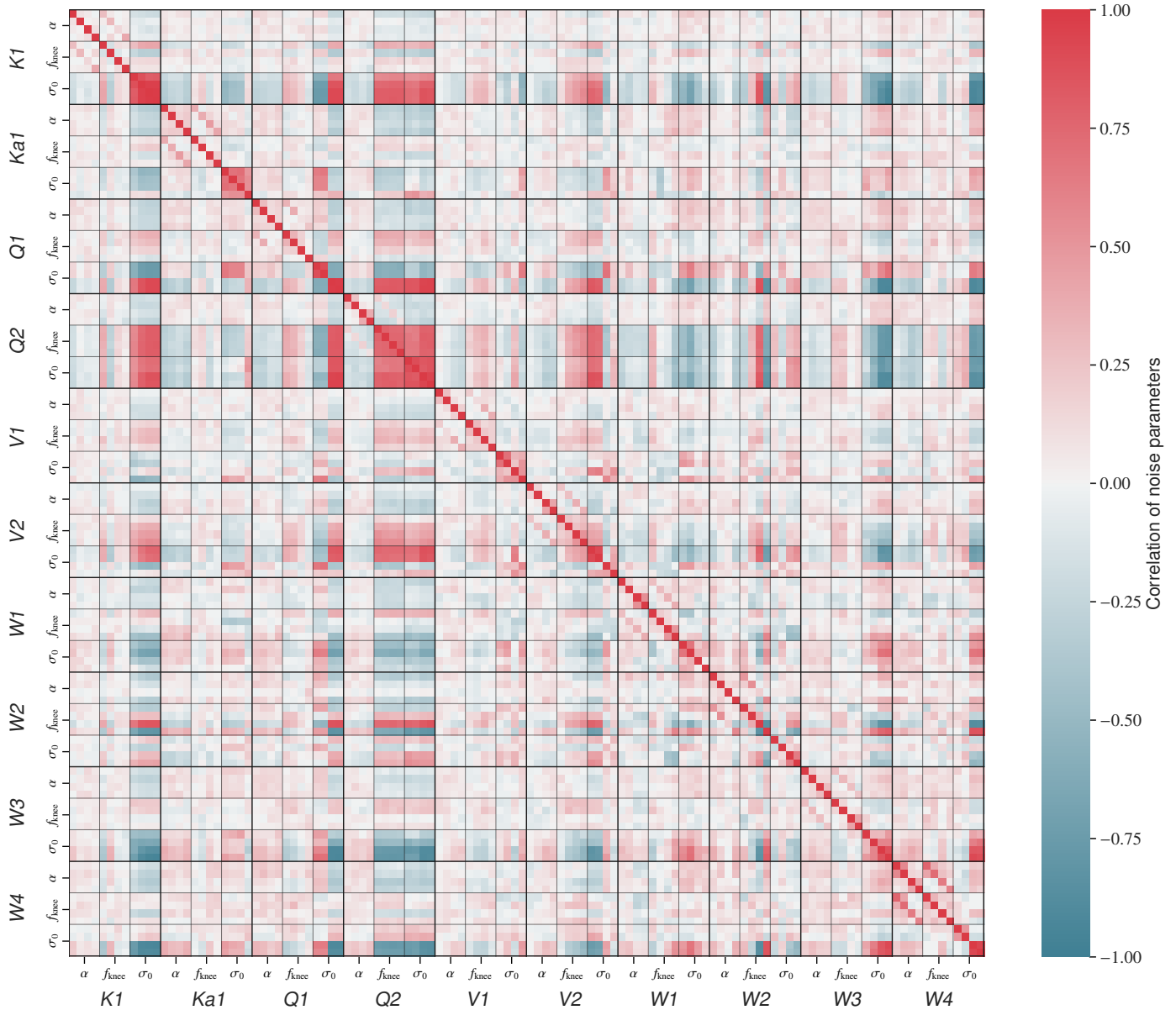


Fig. 4. Noise parameter correlation matrix. We average over all Gibbs samples of the noise parameters $\xi^n = \{\alpha, f_{\text{knee}}, \sigma_0\}$ for each PID. We then find the correlation in time between these averages for the different bands and detector. The results here are for the calibrated white noise level, $\sigma_0[\text{mK}]$. The values for each detector are ordered 13, 14, 23, and 24

porttitor. Vestibulum porttitor. Nulla facilisi. Sed a turpis eu la-
cus commodo facilisis. Morbi fringilla, wisi in dignissim inter-
dum, justo lectus sagittis dui, et vehicula libero dui cursus dui.
Mauris tempor ligula sed lacus. Duis cursus enim ut augue. Cras
ac magna. Cras nulla. Nulla egestas. Curabitur a leo. Quisque
egestas wisi eget nunc. Nam feugiat lacus vel est. Curabitur con-
sectetuer.

Lorem ipsum dolor sit amet, consectetuer adipiscing elit. Ut purus elit, vestibulum ut, placerat ac, adipiscing vitae, felis. Curabitur dictum gravida mauris. Nam arcu libero, nonummy eget, consectetuer id, vulputate a, magna. Donec vehicula augue eu neque. Pellentesque habitant morbi tristique senectus et netus et malesuada fames ac turpis egestas. Mauris ut leo. Cras viverra metus rhoncus sem. Nulla et lectus vestibulum urna fringilla ultrices. Phasellus eu tellus sit amet tortor gravida placerat. Integer sapien est, iaculis in, pretium quis, viverra ac, nunc. Praesent eget sem vel leo ultrices bibendum. Aenean faucibus. Morbi do-

lor nulla, malesuada eu, pulvinar at, mollis ac, nulla. Curabitur auctor semper nulla. Donec varius orci eget risus. Duis nibh mi, congue eu, accumsan eleifend, sagittis quis, diam. Duis eget orci sit amet orci dignissim rutrum.

The second main deviation... is in the treatment of the noise power spectra. As shown in Sect 2.5 of [Jarosik et al. \(2007\)](#), the noise autocorrelation spectrum is fit on a year-by-year basis to a polynomial in $\log(\Delta t)$, where Δt is the time lag between data points. This method is very similar to the `Commander3` approach, which fits for the power spectrum in Fourier space using a correlated noise model of the form $\sigma_0^2(f/f_{\text{knee}})^\alpha$. Properly parameterized, these two approaches should yield similar results, albeit with different levels of uncertainty and time resolution. However, we have confirmed that in many cases the simple $1/f$ noise model does not fit the signal-subtracted TOD, yielding χ^2 values that are up to 10σ discrepant from their expected values. [Show,

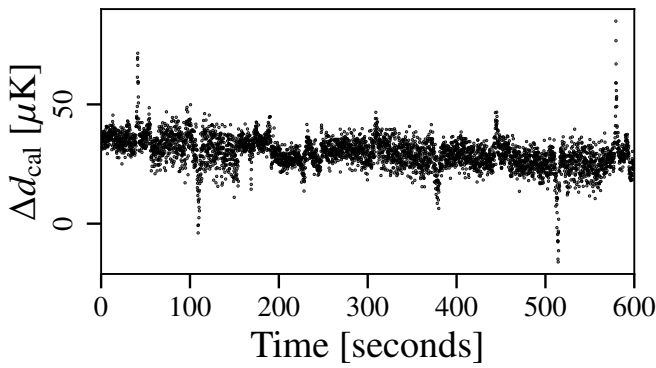


Fig. 5. Difference between the COSMOGLOBE $d_{\text{cal}} = d/g - b - s_{\text{sl}}$ and the delivered calibrated TOD from WMAP.

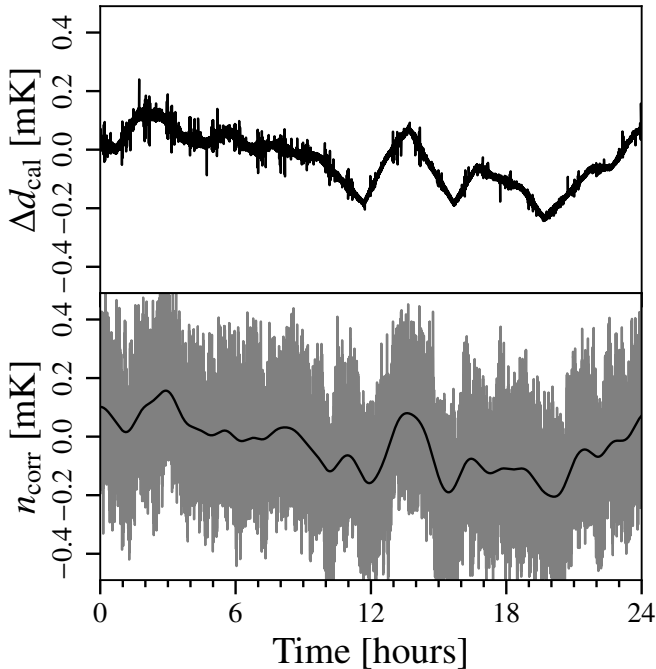


Fig. 6. (top) Difference between the COSMOGLOBE $d_{\text{cal}} = d/g - b - s_{\text{sl}}$ and the delivered calibrated TOD from WMAP. (bottom) Raw correlated noise (gray) and smoothed data with Gaussian kernel (black). This shows more clearly the hourly baseline subtraction from the WMAP treatment.

discuss figure with the PSDs, residual spectrum, and Bessel filter.]

Deviations from the $1/f$ model consist either of a linear increase or downturn above 10 Hz. This can be partially explained by the use of a two pole Bessel low-pass filter just prior to signal quantization, which introduces a 2.62% correlation between 25.6 ms sample integrations (Jarosik et al. 2003b, Sect. 5.3). The exact form of the Bessel filter was not used on flight data, but rather the parametric fit as discussed above. However, the filter is designed to reduce the signal by half at 100 Hz, and as such has a negligible effect.

Etiam ipsum dolor sit amet, consectetur adipiscing elit. Ut purus elit, vestibulum ut, placerat ac, adipiscing vitae, felis. Curabitur dictum gravida mauris. Nam arcu libero, nonummy eget, consectetur id, vulputate a, magna. Donec vehicula augue eu neque. Pellentesque habitant morbi tristique senectus et netus et

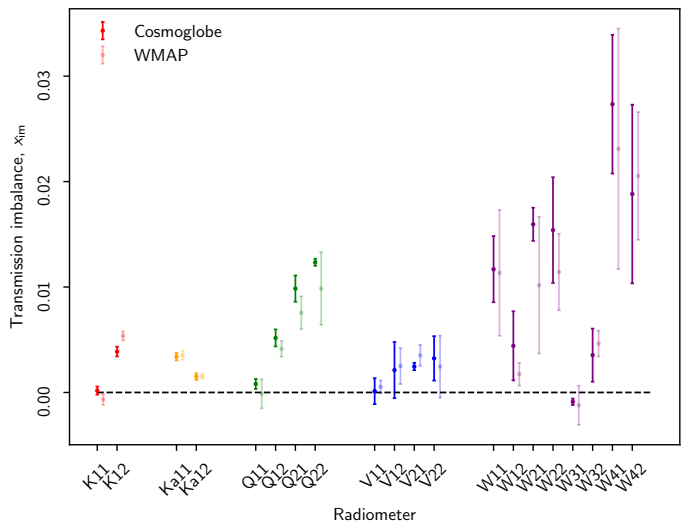


Fig. 7. Transmission imbalance

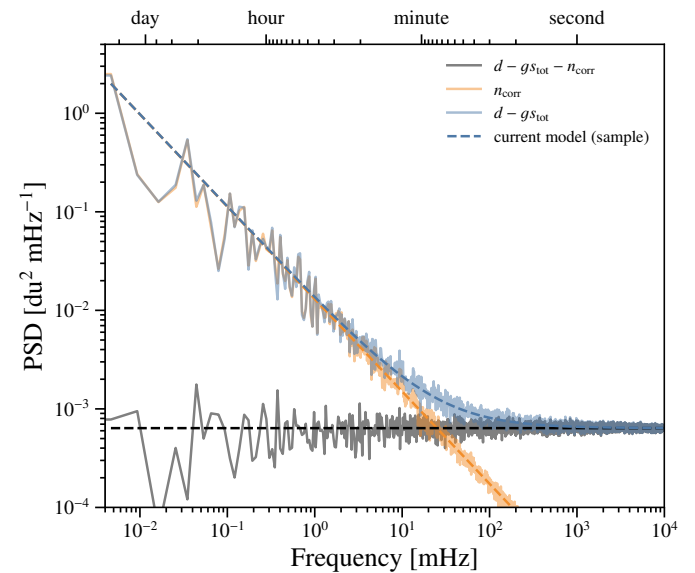


Fig. 8. PSD for radiometer W413 that spans MJDs 52252.3–52254.8. The power spectrum of the blue line corresponds to the residual, while the gray line is the residual with a correlated noise realization removed.

malesuada fames ac turpis egestas. Mauris ut leo. Cras viverra metus rhoncus sem. Nulla et lectus vestibulum urna fringilla ultrices. Phasellus eu tellus sit amet tortor gravida placerat. Integer sapien est, iaculis in, pretium quis, viverra ac, nunc. Praesent eget sem vel leo ultrices bibendum. Aenean faucibus. Morbi dolor nulla, malesuada eu, pulvinar at, mollis ac, nulla. Curabitur auctor semper nulla. Donec varius orci eget risus. Duis nibh mi, congue eu, accumsan eleifend, sagittis quis, diam. Duis eget orci sit amet orci dignissim rutrum.

Nam dui ligula, fringilla a, euismod sodales, sollicitudin vel, wisi. Morbi auctor lorem non justo. Nam lacus libero, pretium at, lobortis vitae, ultricies et, tellus. Donec aliquet, tortor sed accumsan bibendum, erat ligula aliquet magna, vitae ornare odio metus a mi. Morbi ac orci et nisl hendrerit mollis. Suspendisse ut massa. Cras nec ante. Pellentesque a nulla. Cum sociis natoque penatibus et magnis dis parturient montes, nascetur ridiculus mus. Aliquam tincidunt urna. Nulla ullamcorper vestibulum turpis. Pellentesque cursus luctus mauris.

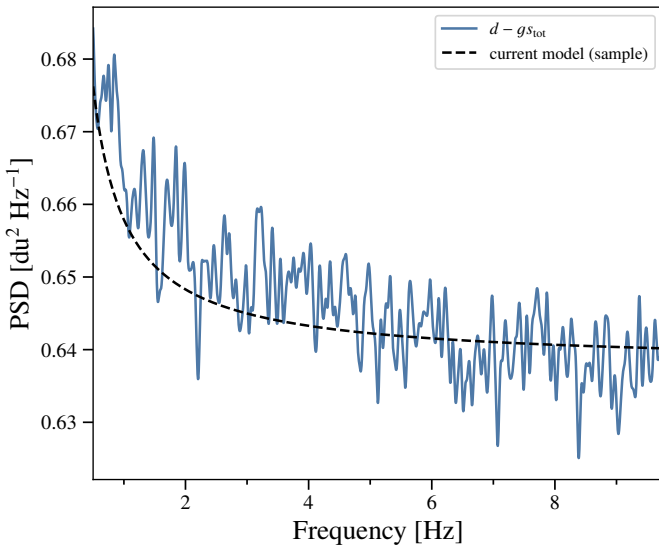


Fig. 9. PSD for radiometer W413 that spans MJDs 52252.3–52254.8. The black dashed line is a sample of the theoretical PSD, while the blue line is the smoothed residual power spectrum.

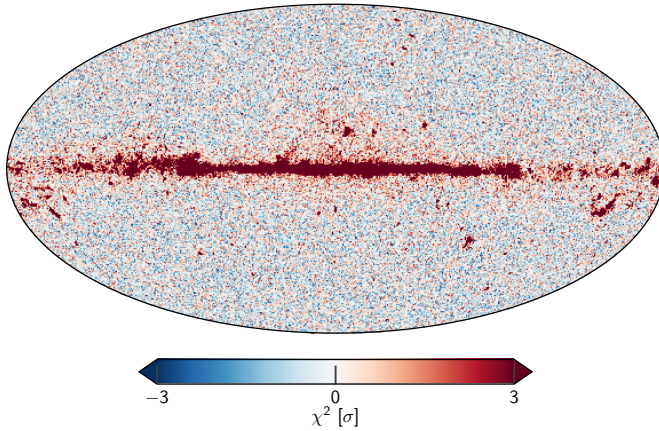


Fig. 10. Reduced- χ^2 , using $n_{\text{dof}} = 300$, which comes from fitting to the regions outside of the K -band processing mask.

Nulla malesuada porttitor diam. Donec felis erat, congue non, volutpat at, tincidunt tristique, libero. Vivamus viverra fermentum felis. Donec nonummy pellentesque ante. Phasellus adipiscing semper elit. Proin fermentum massa ac quam. Sed diam turpis, molestie vitae, placerat a, molestie nec, leo. Maecenas lacinia. Nam ipsum ligula, eleifend at, accumsan nec, suscipit a, ipsum. Morbi blandit ligula feugiat magna. Nunc eleifend consequat lorem. Sed lacinia nulla vitae enim. Pellentesque tincidunt purus vel magna. Integer non enim. Praesent euismod nunc eu purus. Donec bibendum quam in tellus. Nullam cursus pulvinar lectus. Donec et mi. Nam vulputate metus eu enim. Vestibulum pellentesque felis eu massa.

Quisque ullamcorper placerat ipsum. Cras nibh. Morbi vel justo vitae lacus tincidunt ultrices. Lorem ipsum dolor sit amet, consectetur adipiscing elit. In hac habitasse platea dictumst. Integer tempus convallis augue. Etiam facilisis. Nunc elementum fermentum wisi. Aenean placerat. Ut imperdiet, enim sed gravida sollicitudin, felis odio placerat quam, ac pulvinar elit purus eget enim. Nunc vitae tortor. Proin tempus nibh sit amet nisl. Vivamus quis tortor vitae risus porta vehicula.

5. Frequency maps

5.1. Map summary statistics

Will combine these spectra shortly

Want to compare the QU correlation in WMAP and Planck LFI, get a quantitative number. Point out that the polarization solution itself is much better, but the covariance between pixels themselves is much higher. This wasn't an issue for LFI, so we had to take that into account here.

I also want to put a bit here on why the low- ℓ approach needed to be done separately, how correlated noise sampling addresses it, to what extent it's mitigated, etc.

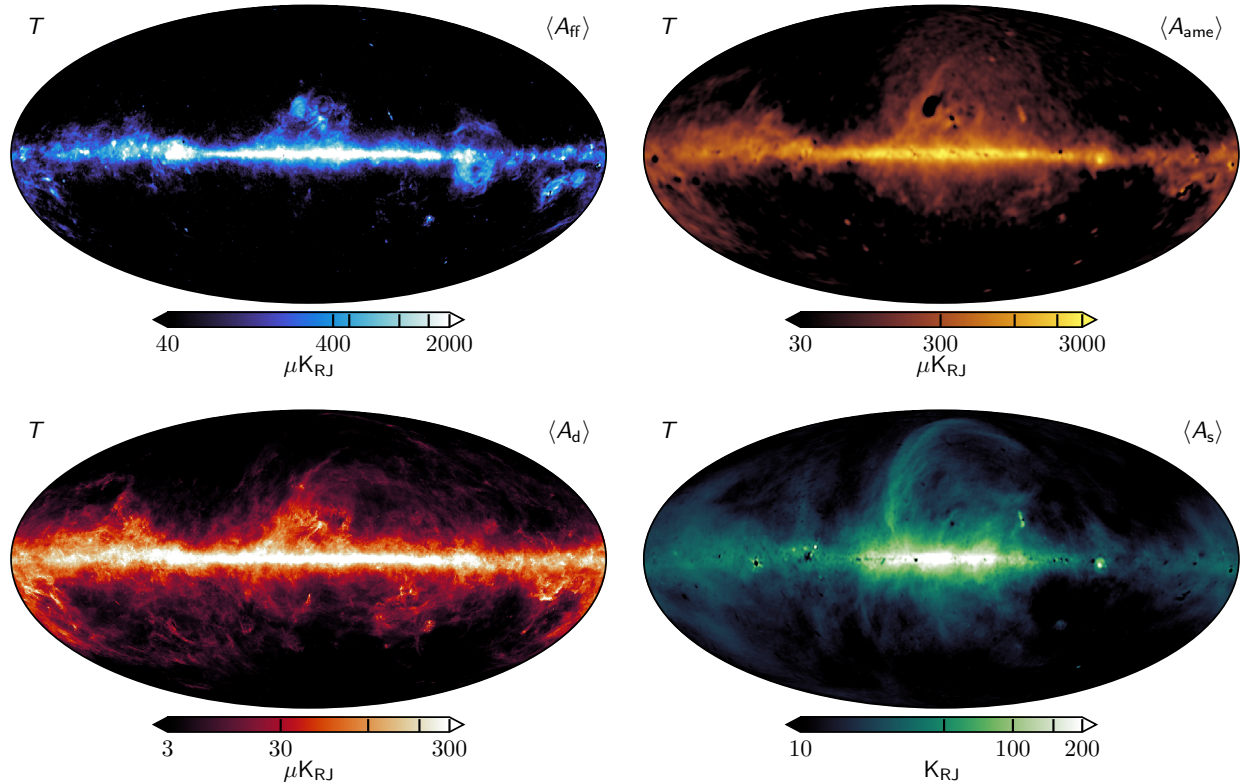
Note that LFI's 30 and 70 GHz QU correlation is ~ 0.1 , whereas 44 GHz is much larger, ~ 0.5 . This discrepancy is due to the number of horns with differing polarization orientation. Both 30 and 70 GHz have an even number of horns, allowing for pairs of datastreams to be combined to give independent polarization measurements. Conversely, 44 GHz has one horn pair and an unpaired horn, the latter of which induces more correlation in the QU observation matrix. An example for Ka and 30 GHz is shown in Fig. ???. Aside from the obvious morphological changes due to the two experiments' different observing strategies, the magnitude of WMAP's correlation is much larger than Planck's.

The BEYONDPLANCK project took this covariance structure into account using the dense $N_{\text{side}} = 16$ noise covariance matrix provided by the WMAP team.⁸ Properly sampled correlated noise only leaves white noise in the maps, so the noise properties of each map's sample do not require a dense pixel-pixel covariance, even at low resolution (BeyondPlanck 2022; Basyrov et al. 2022). The WMAP9 inverse noise covariance matrices were computed using the full time-space noise matrix $\mathbf{N} = \mathbf{N}^w + \mathbf{N}^{corr}$, so the full pixel-pixel covariance matrix $\Sigma^{-1} = \mathbf{P}^T \mathbf{N}^{-1} \mathbf{P}$ took into account the correlation between neighboring samples. The COSMOGLOBE maps, by subtracting a realization of correlated noise before mapmaking, estimates an inverse noise covariance matrix

$$\Sigma_{pp'}^{-1} = \sum_{t_1, t_2} \mathbf{P}_{t_1, p_1}^T \mathbf{N}_{t_1, t_2}^{-1} \mathbf{P}_{t_2, p_2} = \sum_t \mathbf{P}_{t, p_1}^T \mathbf{N}_{t, t}^{-1} \mathbf{P}_{t, p_2} \quad (56)$$

How much off-diagonal pixel covariance is there here?

dense noise covariance matrix also explicitly projected out the poorly-measured imbalance modes, but because we find no trace of these modes in our sky maps or residual maps, this treatment is not necessary in our approach. However, the correlation between Stokes Q and U was not taken into account in the BEYONDPLANCK LFI analysis. This was not a significant oversight in the LFI analysis because the 30 and 70 GHz maps only had a 10% correlation, and 44 GHz's 50% correlation was subdominant to other systematic effects. We have updated Commander3 to take QU correlation into account for LFI.

**Fig. 11.** Foreground intensity maps**Table 4.** Difference map χ^2 statistics.

DIFFERENCE	χ^2_{uncorr}	χ^2_{corr}	$\Delta\chi^2$
$0.32 \times \text{K1} - \text{Ka1} \dots$	4291	4287	4
$\text{Q1} - \text{Q2} \dots$	4500	4380	120
$\text{V1} - \text{V2} \dots$	4490	4429	61
$\text{W1} - \text{W2} \dots$	4328	4270	68
$\text{W3} - \text{W4} \dots$	4257	4145	112

Table 5. Transmission imbalance template amplitudes for each WMAP radiometer as estimated by fitting the official templates to low-resolution difference maps between COSMOGLOBE and WMAP. The templates are provided in mK, and the template amplitudes are therefore dimensionless. The fourth column lists the relative decrease in standard deviation, $\sqrt{\sigma_{\text{raw}}^2 - \sigma_{\text{corr}}^2}/\sigma_{\text{raw}}$, after subtracting the best-fit templates in percent.

DA	a_1	a_2	$\Delta\sigma [\%]$
K1	-27.5	-50.6	30
Ka1	-1.4	-1.9	25
Q1	-30.0	-71.6	11
Q2	-7.1	-1.5	20
V1	-32.8	-53.4	6
V2	8.8	-4.1	16
W1	-2.8	4.6	8
W2	-6.9	-3.5	11
W3	29.1	53.4	12
W4	15.5	-6.8	52

5.2. Comparison with 9-year WMAP maps

5.3. Consistency within WMAP channels

5.4. Consistency between WMAP and LFI

6. Preliminary astrophysical results

6.1. CMB results

6.1.1. Solar dipole

6.1.2. Quadrupole and octopole

6.1.3. Angular temperature power spectrum

6.1.4. Large-scale polarization

6.2. Galactic foregrounds

6.3. WMAP-versus-LFI signal-to-noise ratio comparison

7. Systematic error corrections and uncertainties

7.1. Sky map corrections

7.2. Power spectrum residuals

8. Outstanding issues

8.1. Noise modelling

8.2. V-band quadrupole residual

8.3. Degeneracy between K-band calibration and AME dipole

8.4. Other minor effects

8.4.1. Time-variable bandpass modelling

8.4.2. Polarized sidelobe modelling

9. Conclusions

References

Ali-Haïmoud, Y. 2010, Astrophysics Source Code Library [ascl:1010.016]

⁸ https://lambda.gsfc.nasa.gov/product/wmap/dr5/ninv_lfis.dat

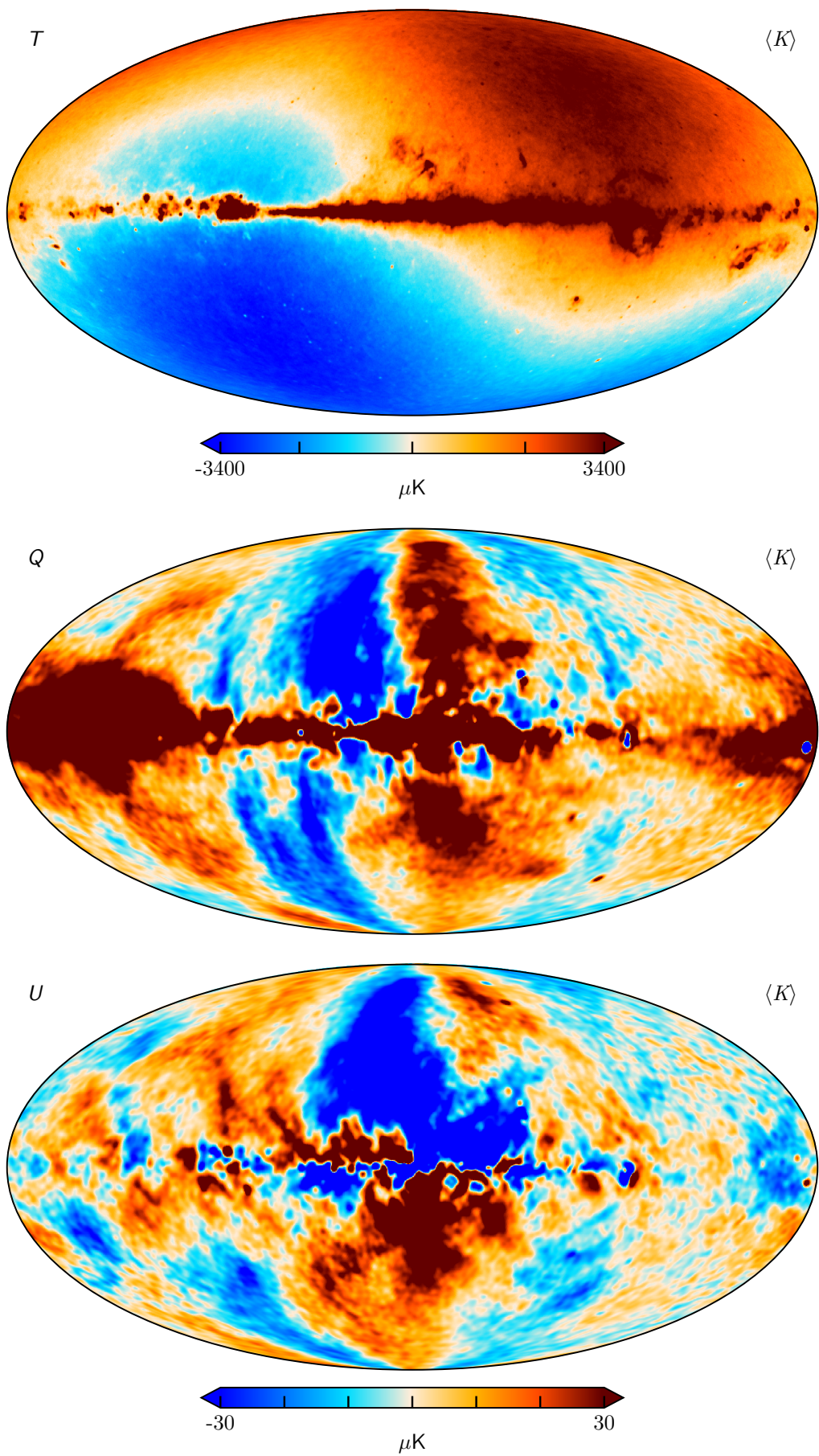


Fig. 12. K -band

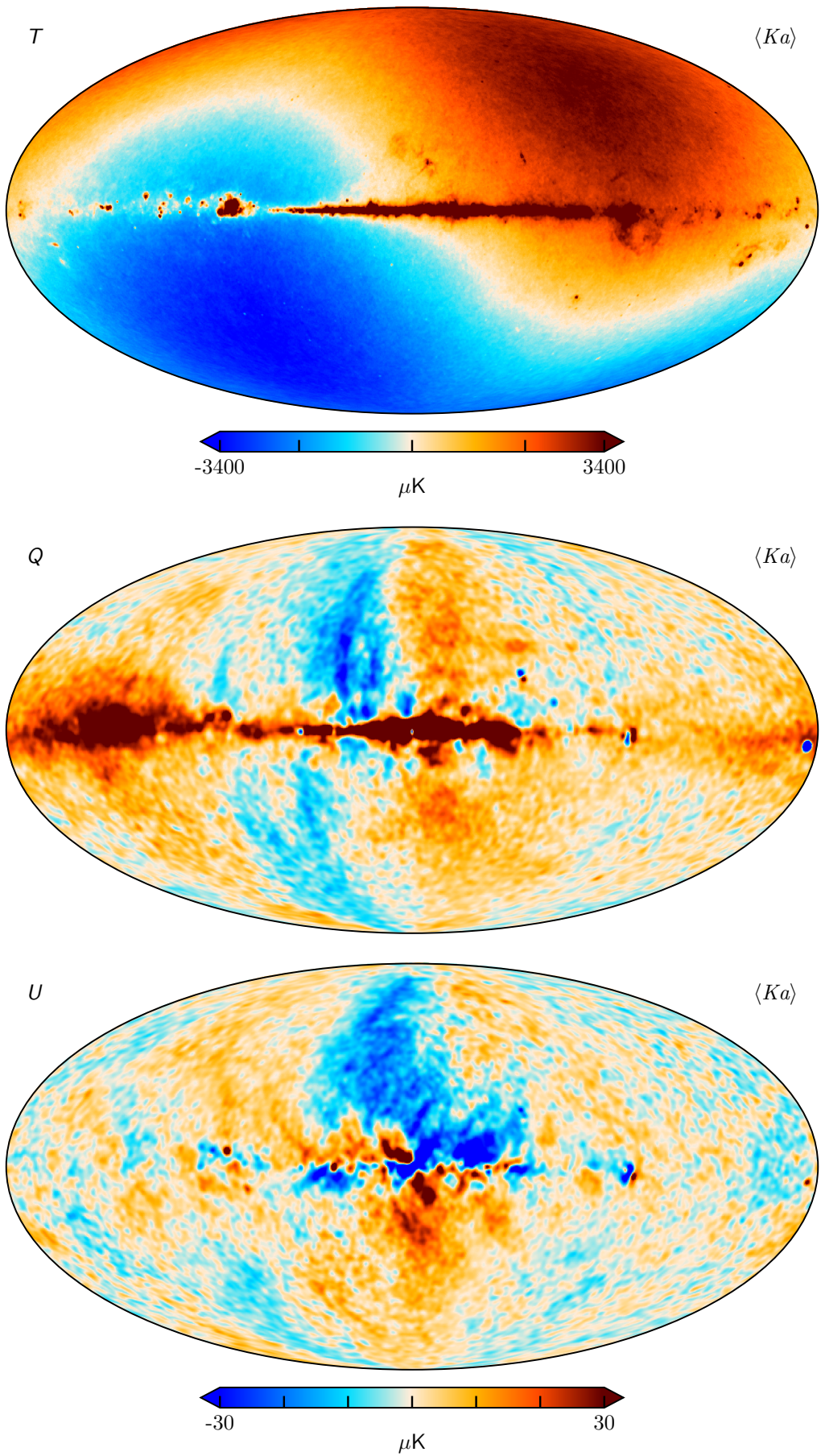


Fig. 13. Ka -band

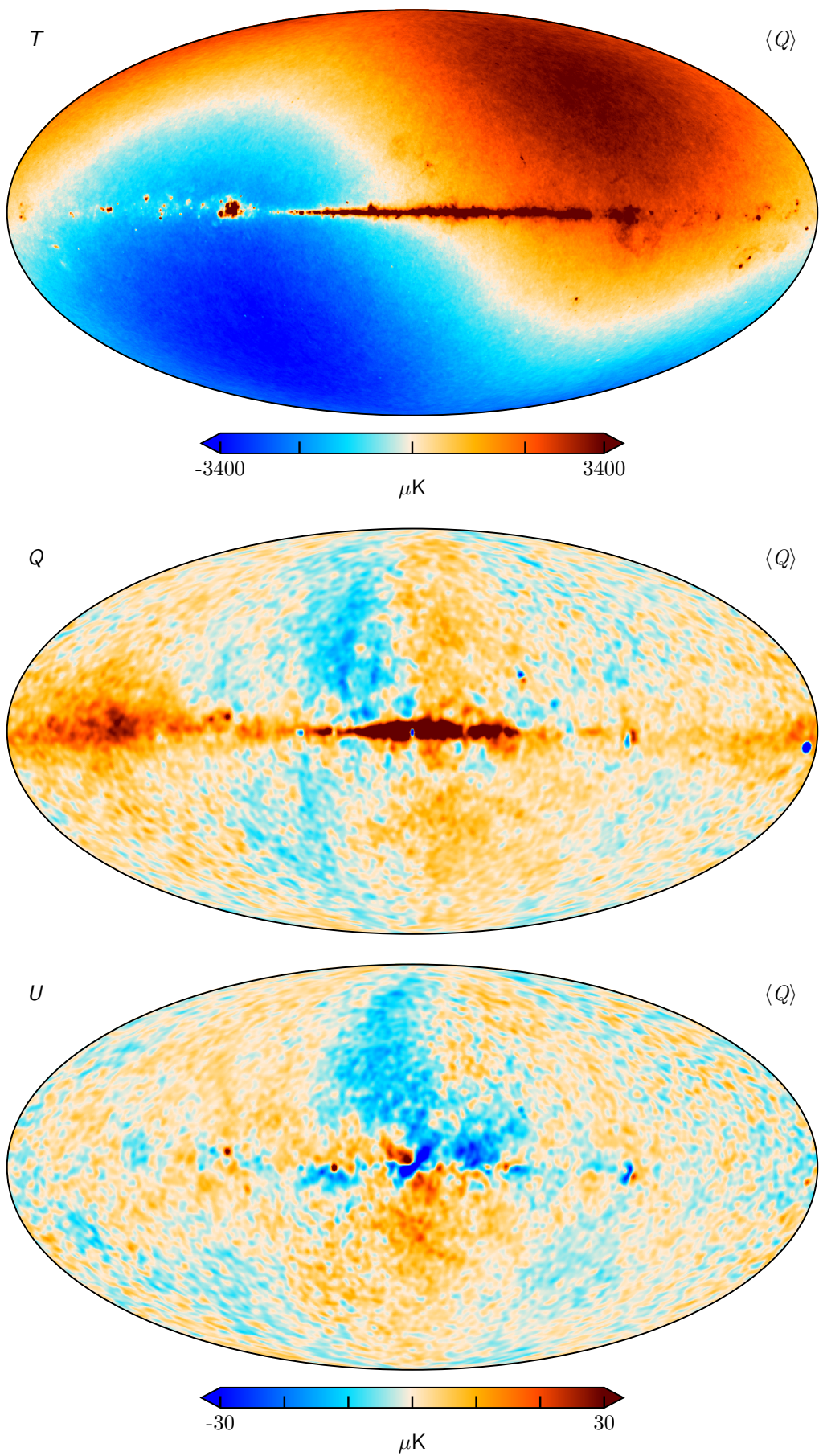


Fig. 14. Q -band

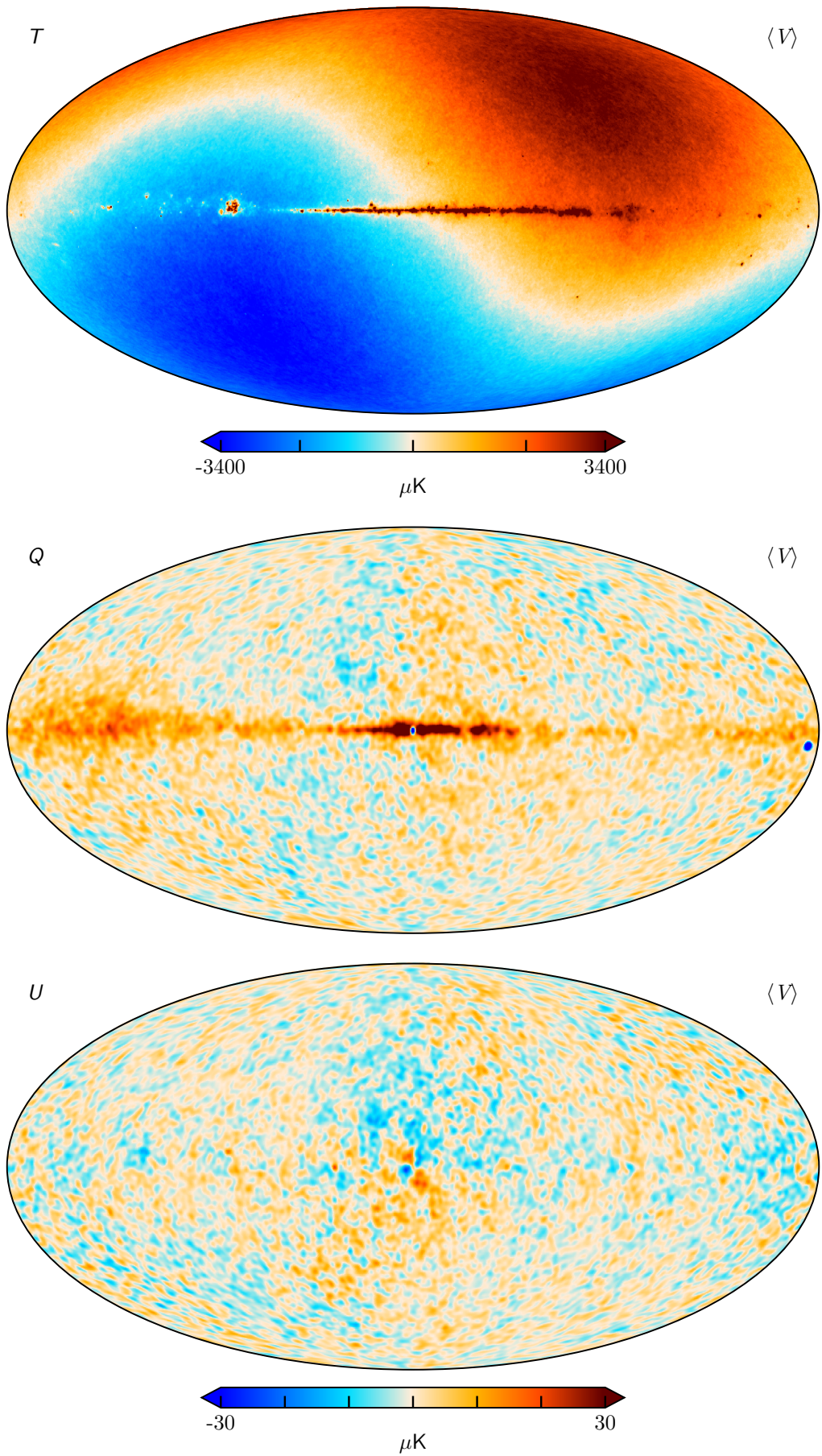


Fig. 15. V -band

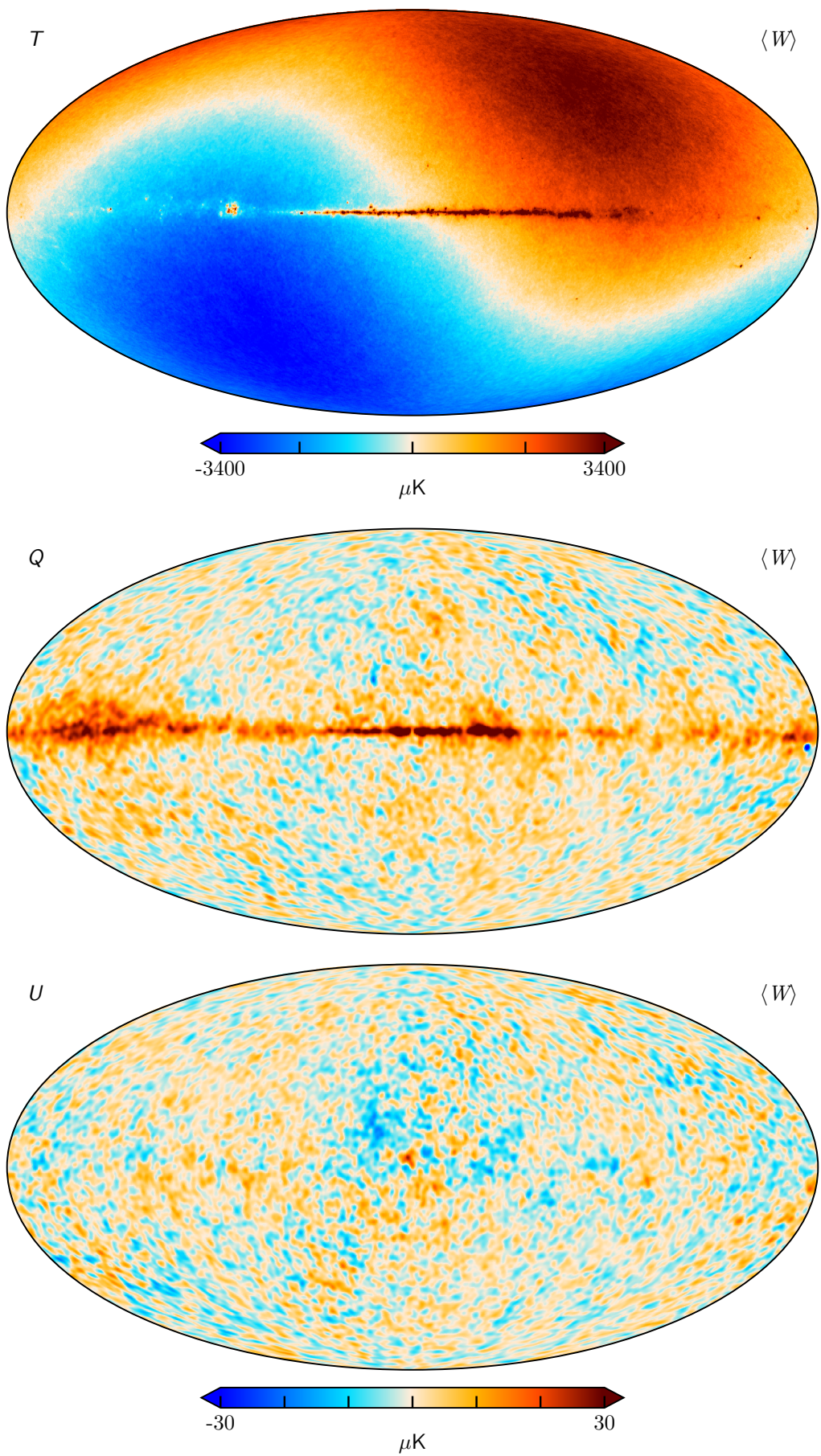
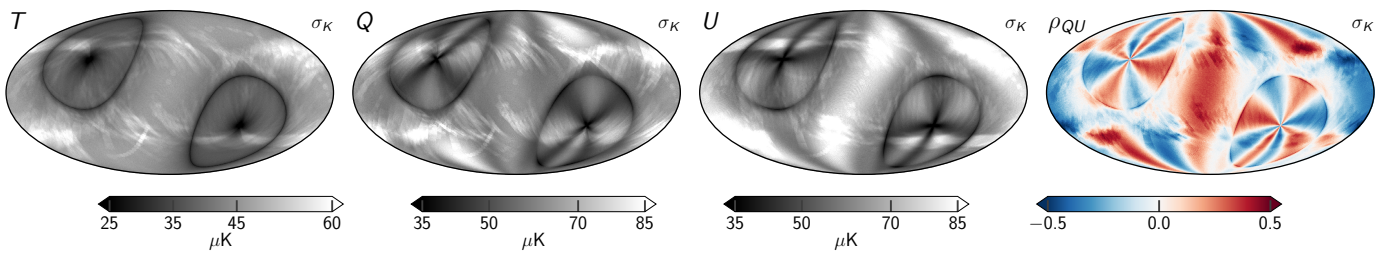
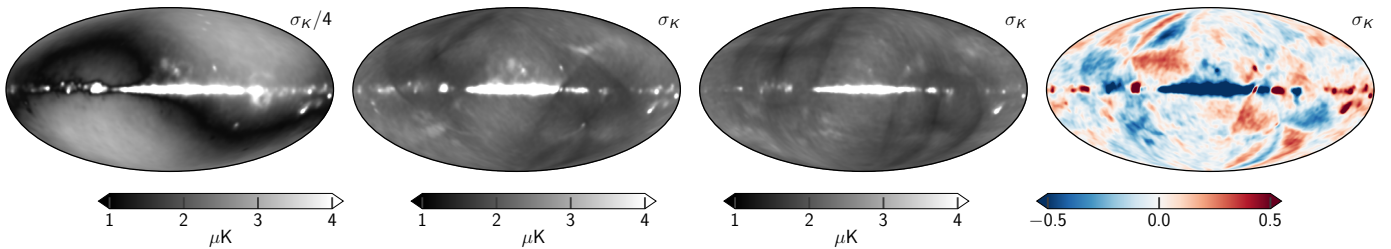


Fig. 16. W -band

**Fig. 17.** RMS**Fig. 18.** K_{std}

- Ali-Haïmoud, Y., Hirata, C. M., & Dickinson, C. 2009, MNRAS, 395, 1055
 Andersen et al. 2022, A&A, in press [arXiv:2201.08188]
 Barnes, C., Hill, R. S., Hinshaw, G., et al. 2003, ApJS, 148, 51
 Barrett, R., Berry, M. W., Chan, T. F., et al. 1994, Templates for the Solution of Linear Systems (Society for Industrial and Applied Mathematics)
 Basyrov et al. 2022, A&A, submitted [arXiv:2208.14293]
 Bennett, C. L., Bay, M., Halpern, M., et al. 2003a, ApJ, 583, 1
 Bennett, C. L., Halpern, M., Hinshaw, G., et al. 2003b, ApJS, 148, 1
 Bennett, C. L., Larson, D., Weiland, J. L., et al. 2013, ApJS, 208, 20
 BeyondPlanck. 2022, A&A, submitted [arXiv:2011.05609]
 Dicke, R. H., Peebles, P. J. E., Roll, P. G., & Wilkinson, D. T. 1965, ApJ, 142, 414
 Frigo, M. & Johnson, S. G. 2005, Proceedings of the IEEE, 93, 216, special issue on “Program Generation, Optimization, and Platform Adaptation”
 Galloway et al. 2022, A&A, in press [arXiv:2201.03509]
 Gjerløw et al. 2022, A&A, submitted [arXiv:2011.08082]
 Greason, M. R., Limon, M., Wollack, E., et al. 2012, Nine-Year Explanatory Supplement, 5th edn., Greenbelt, MD: NASA/GSFC
 Haslam, C. G. T., Salter, C. J., Stoffel, H., & Wilson, W. E. 1982, A&AS, 47, 1
 Hill, R. S., Weiland, J. L., Odegard, N., et al. 2009, ApJS, 180, 246
 Hinshaw, G., Barnes, C., Bennett, C. L., et al. 2003, ApJS, 148, 63
 Hinshaw, G., Nolta, M. R., Bennett, C. L., et al. 2007, ApJS, 170, 288
 Hinshaw, G., Weiland, J. L., Hill, R. S., et al. 2009, ApJS, 180, 225
 Hu, W., Fukugita, M., Zaldarriaga, M., & Tegmark, M. 2001, ApJ, 549, 669
 Ihle et al. 2022, A&A, in press [arXiv:2011.06650]
 Jarosik, N., Barnes, C., Bennett, C. L., et al. 2003a, ApJS, 148, 29
 Jarosik, N., Barnes, C., Greason, M. R., et al. 2007, ApJS, 170, 263
 Jarosik, N., Bennett, C. L., Dunkley, J., et al. 2011, ApJS, 192, 14
 Jarosik, N., Bennett, C. L., Halpern, M., et al. 2003b, ApJS, 145, 413
 Keihänen et al. 2022, A&A, in press [arXiv:2011.06624]
 Lange, A. E., Ade, P. A., Bock, J. J., et al. 2001, Phys. Rev. D, 63, 042001
 Mather, J. C., Cheng, E. S., Cottingham, D. A., et al. 1994, ApJ, 420, 439
 Mather, J. C., Fixsen, D. J., Shafer, R. A., Mosier, C., & Wilkinson, D. T. 1999, ApJ, 512, 511
 Page, L., Jackson, C., Barnes, C., et al. 2003, ApJ, 585, 566
 Penzias, A. A. & Wilson, R. W. 1965, ApJ, 142, 419
 Planck Collaboration II. 2016, A&A, 594, A2
 Planck Collaboration I. 2020, A&A, 641, A1
 Planck Collaboration II. 2020, A&A, 641, A2
 Planck Collaboration III. 2020, A&A, 641, A3
 Planck Collaboration Int. XLVI. 2016, A&A, 596, A107
 Press, W. H., Teukolsky, S. A., Vetterling, W. T., & Flannery, B. P. 2007, Numerical Recipes 3rd Edition: The Art of Scientific Computing, 3rd edn. (USA: Cambridge University Press)
 Remazeilles, M., Dickinson, C., Banday, A. J., Bigot-Sazy, M.-A., & Ghosh, T. 2015, MNRAS, 451, 4311
 Silsbee, K., Ali-Haïmoud, Y., & Hirata, C. M. 2011, MNRAS, 411, 2750
 Smoot, G. F., Bennett, C. L., Kogut, A., et al. 1992, ApJ, 396, L1
 Stevenson, M. A. 2014, The Astrophysical Journal, 781, 113
 Svalheim et al. 2022, A&A, in press [arXiv:2011.08503]
 Tramonte, D., Génova-Santos, R. T., Rubiño-Martín, J. A., et al. 2023, MNRAS, 519, 3432
 van der Vorst, H. A. 1992, SIAM Journal on Scientific and Statistical Computing, 13, 631
 Watts et al. 2022, A&A, in press [arXiv:2202.11979]
 Weiland, J. L., Odegard, N., Hill, R. S., et al. 2011, ApJS, 192, 19

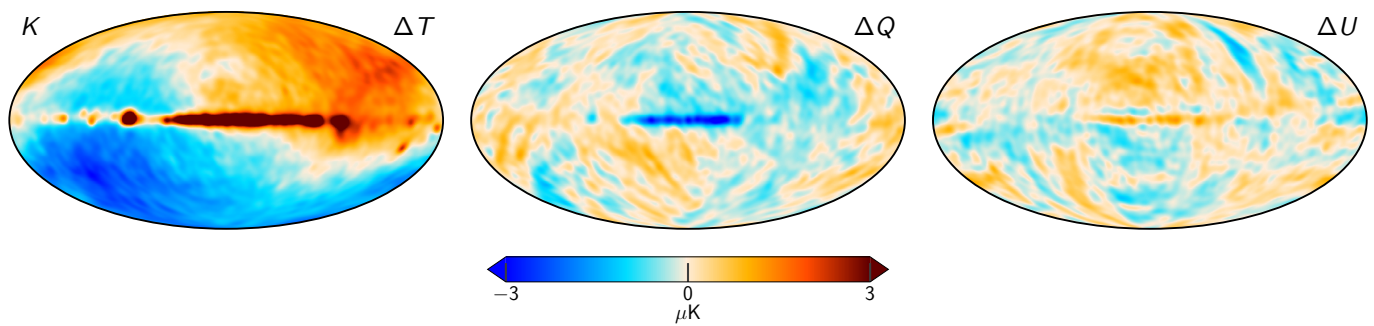


Fig. 19. K sample diff

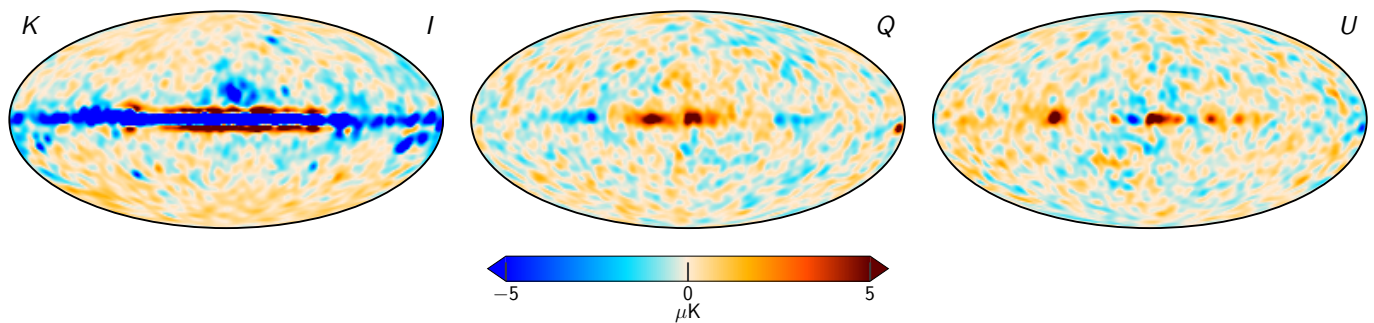
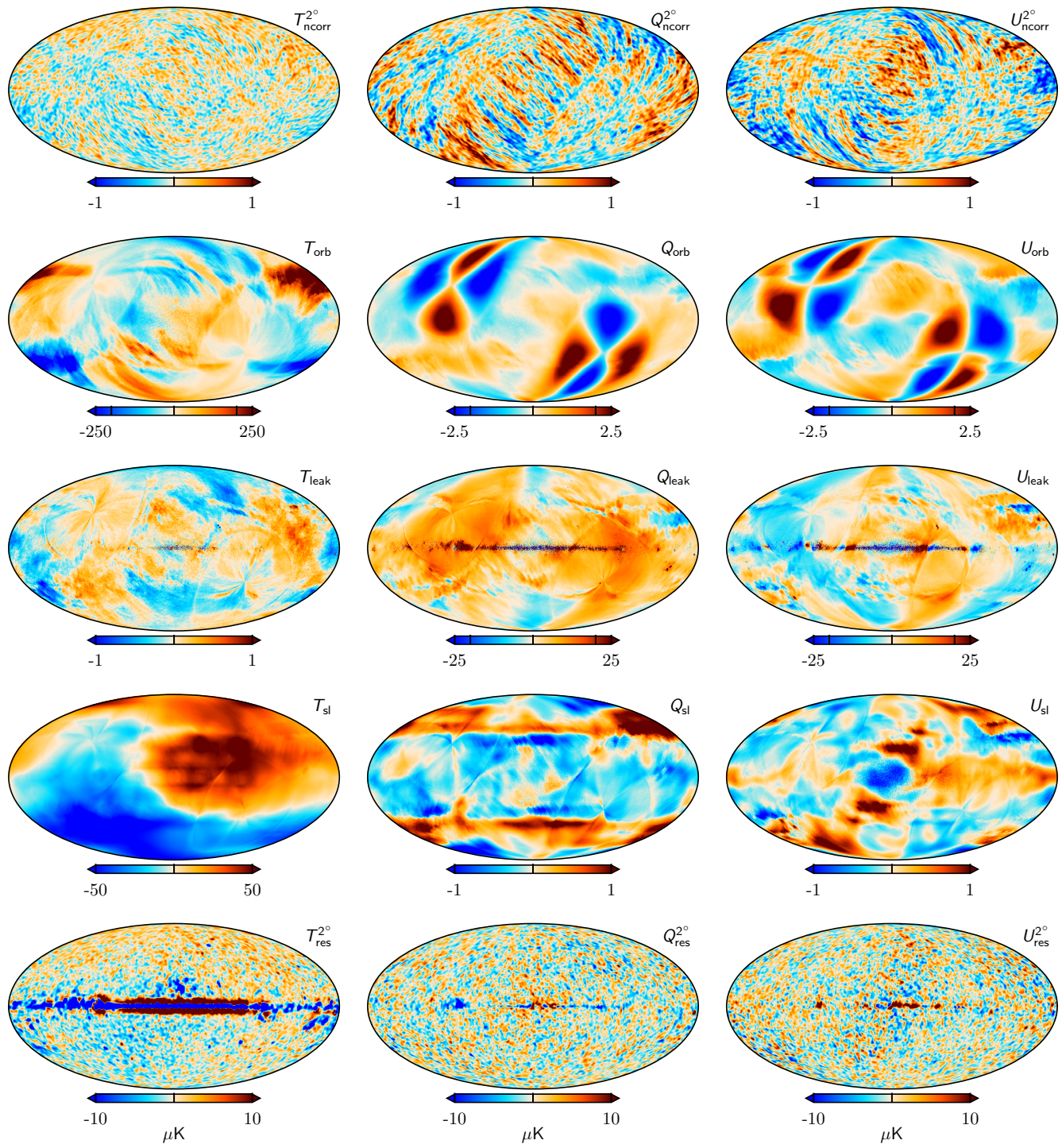


Fig. 20. K residual

**Fig. 21.** Time-ordered components projected

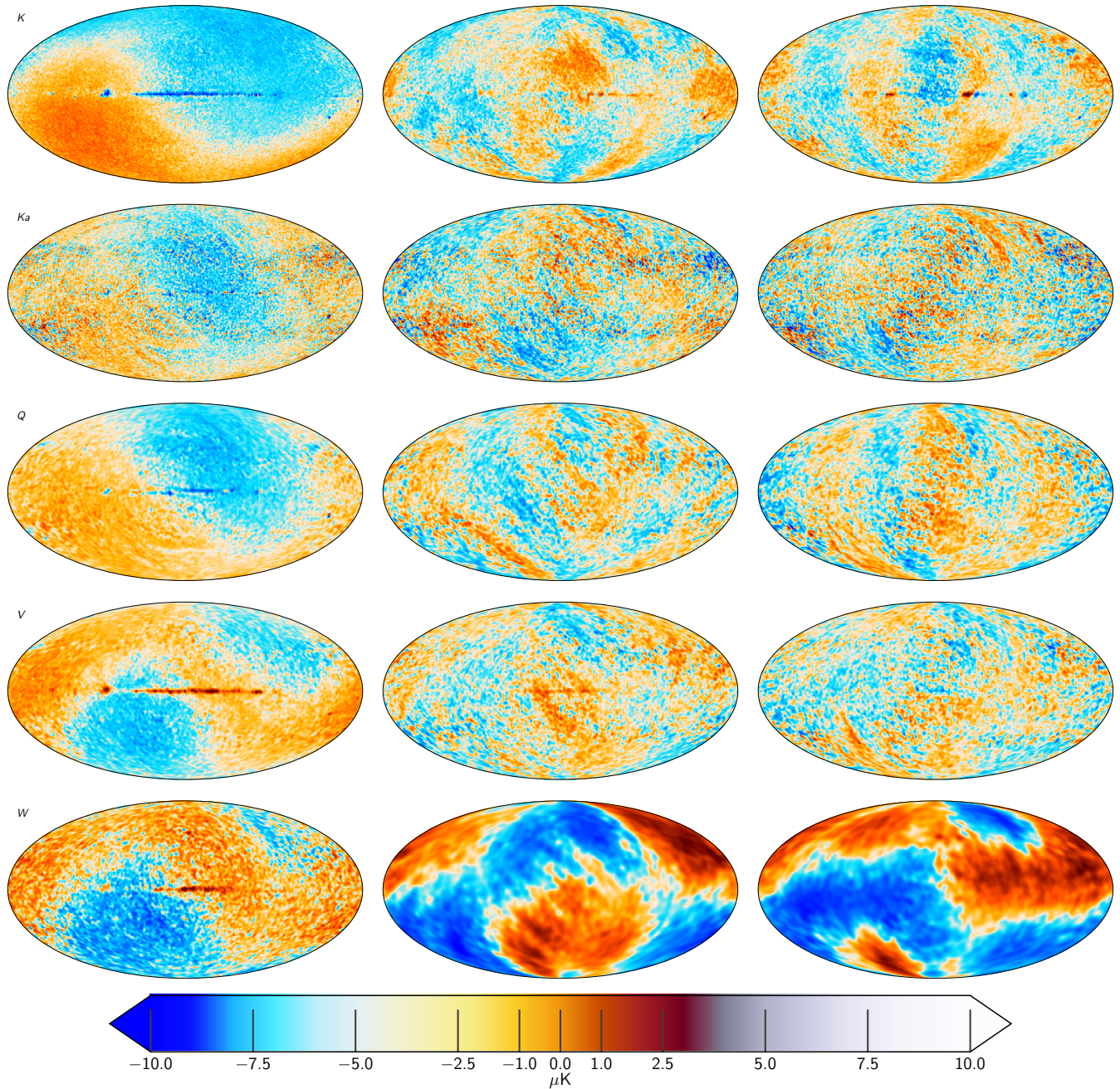
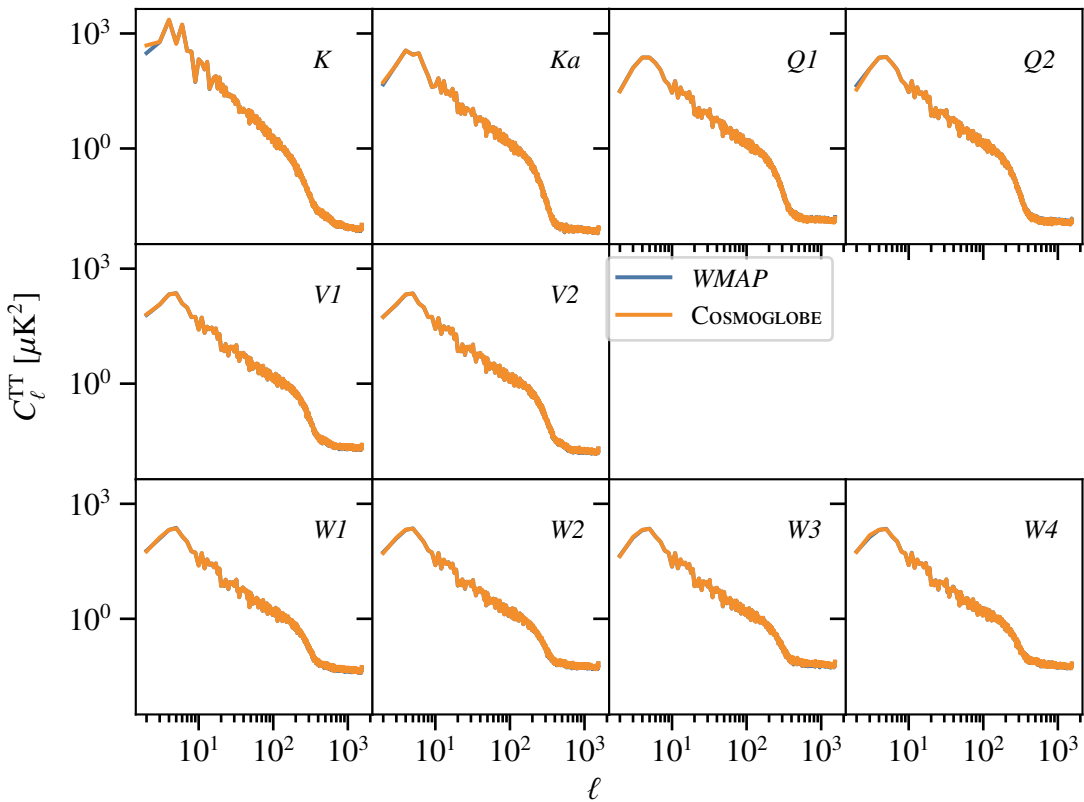
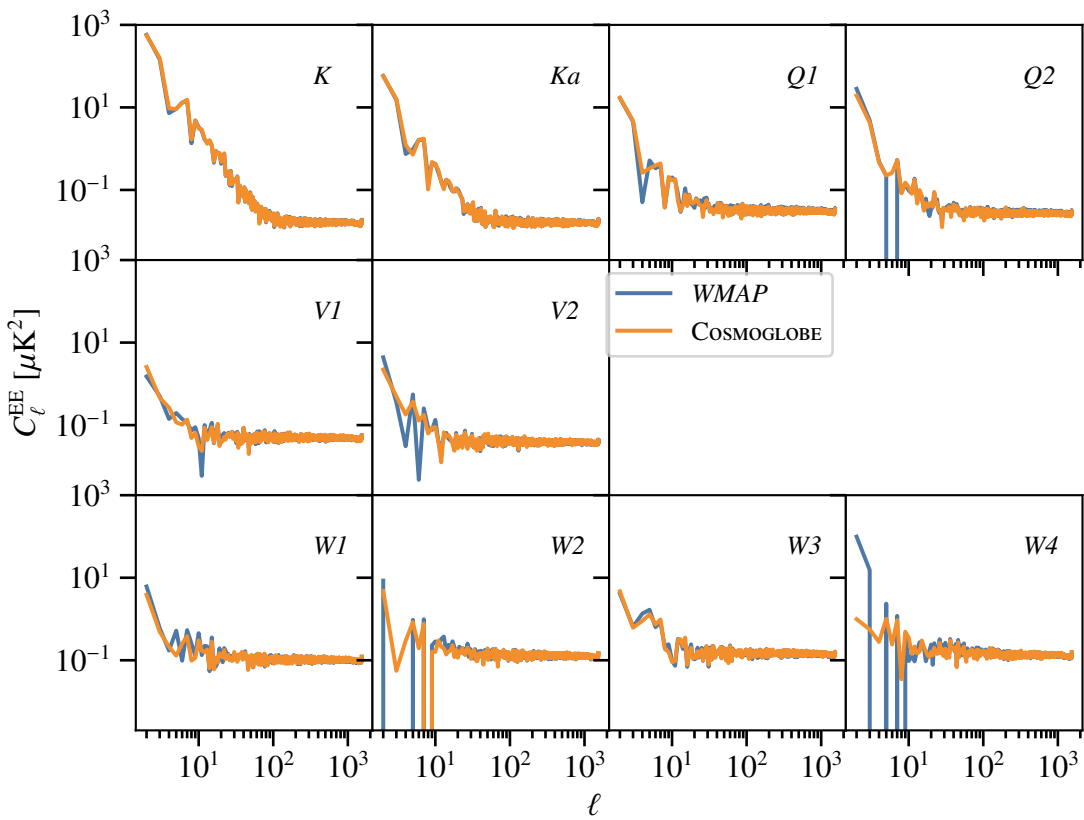
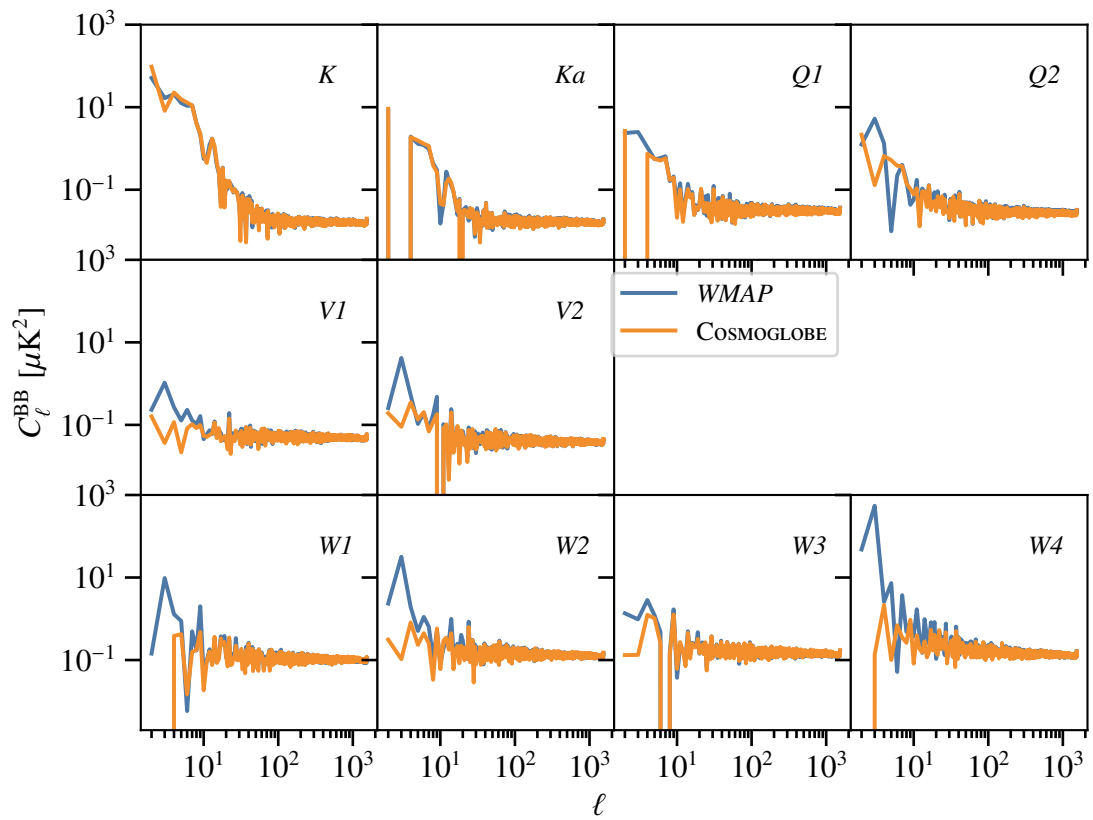
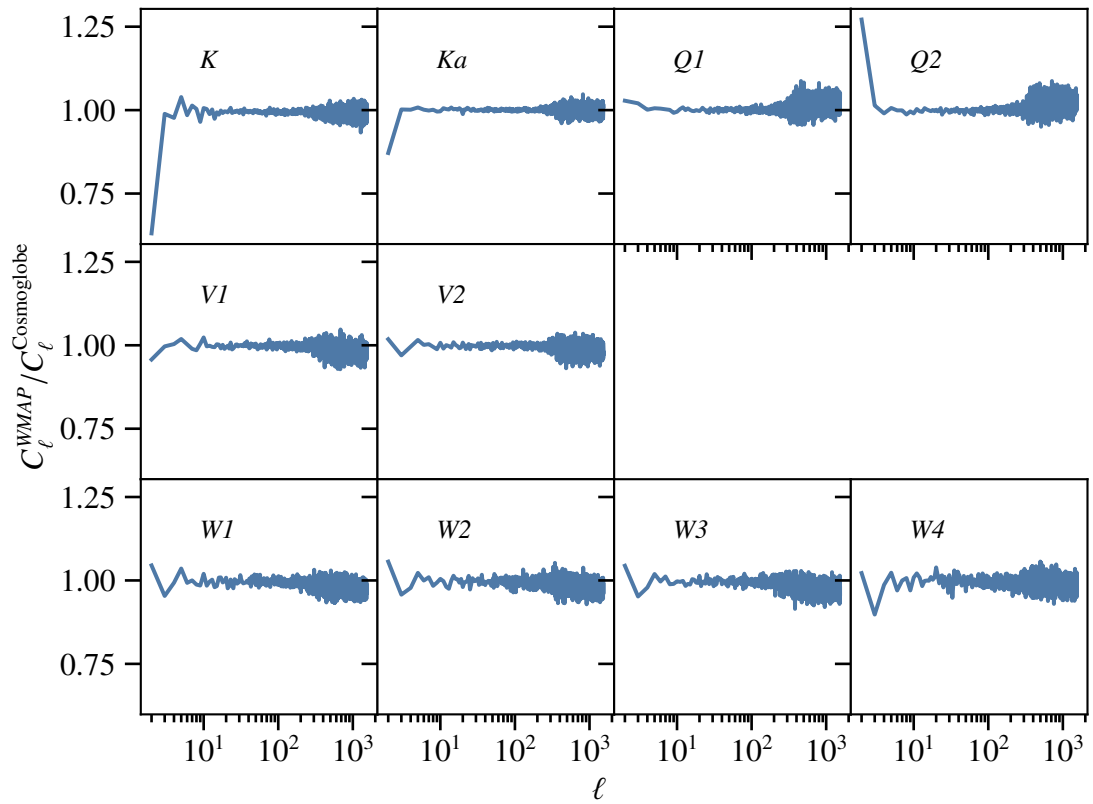
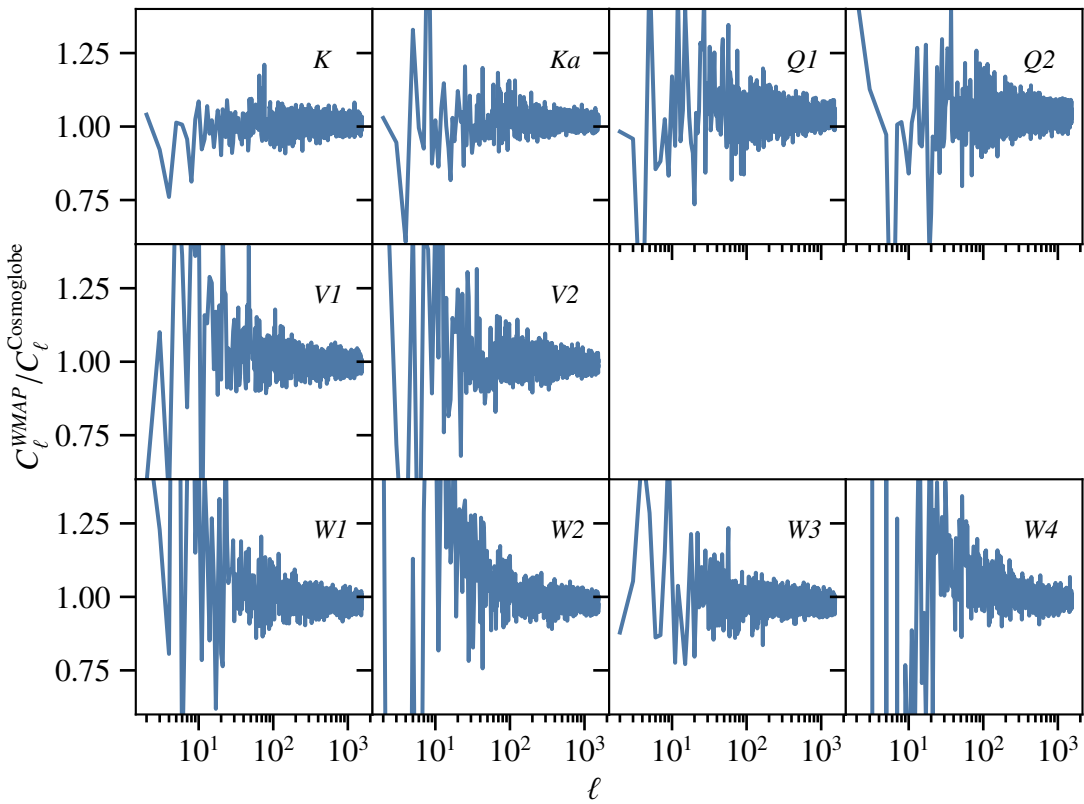
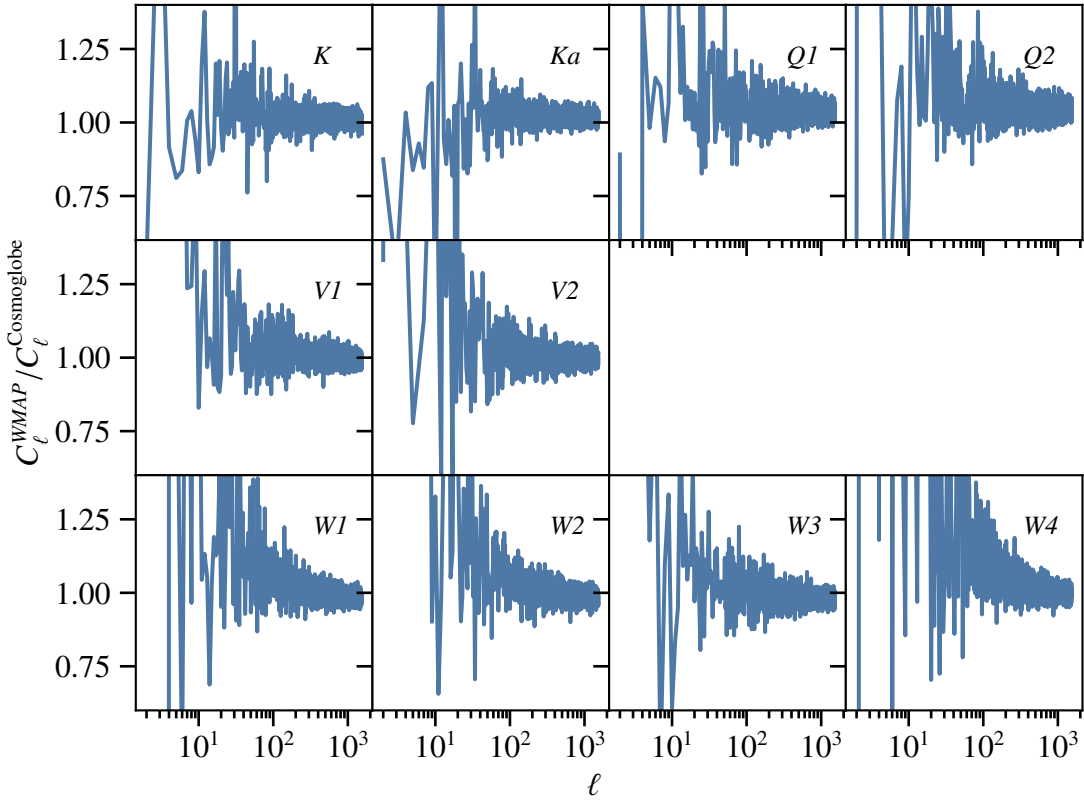


Fig. 22. Difference maps between the COSMOGLOBE and 9-year WMAP frequency maps. Columns show Stokes T , Q , and U parameter maps, while rows show K -, Ka -, Q -, V -, and W -band maps. The temperature maps are smoothed to an angular resolution of 1° FWHM, while the polarization maps are smoothed to 5° FWHM.

**Fig. 23.** TT power spectra**Fig. 24.** EE power spectra

**Fig. 25.** BB power spectra**Fig. 26.** TT ratios

**Fig. 27.** EE ratios**Fig. 28.** BB ratios

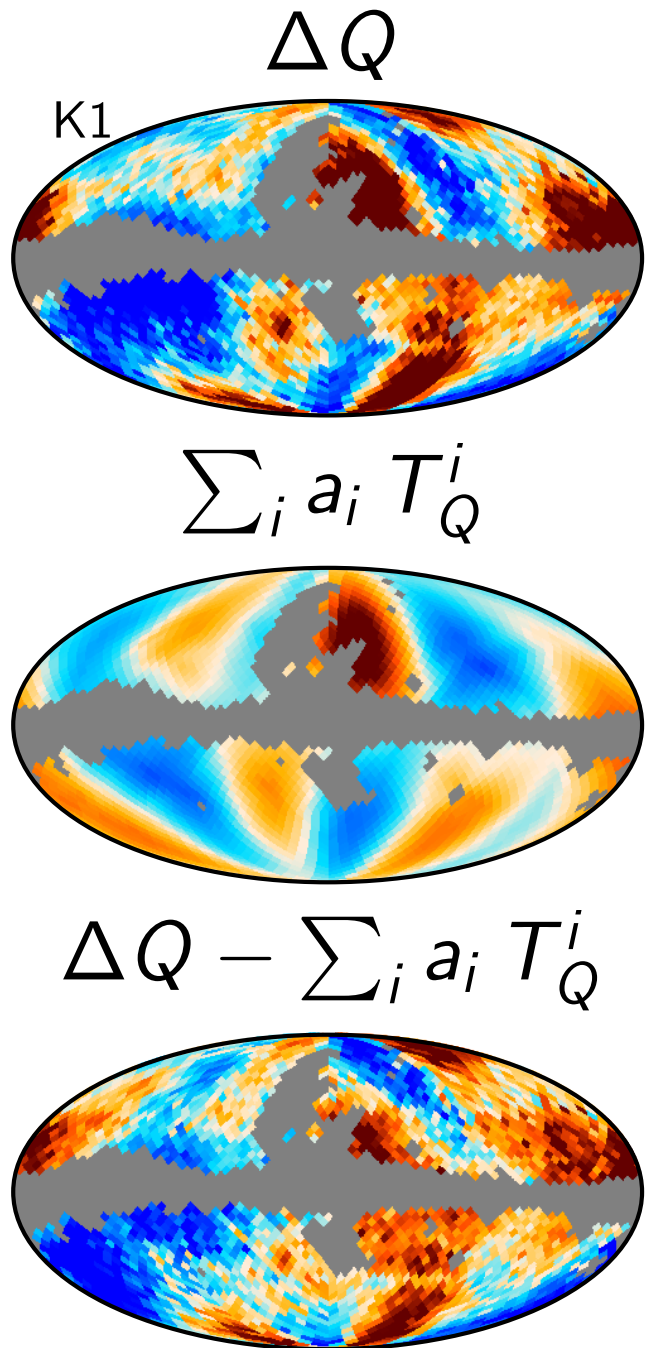


Fig. 29. K-band transmission imbalance templates

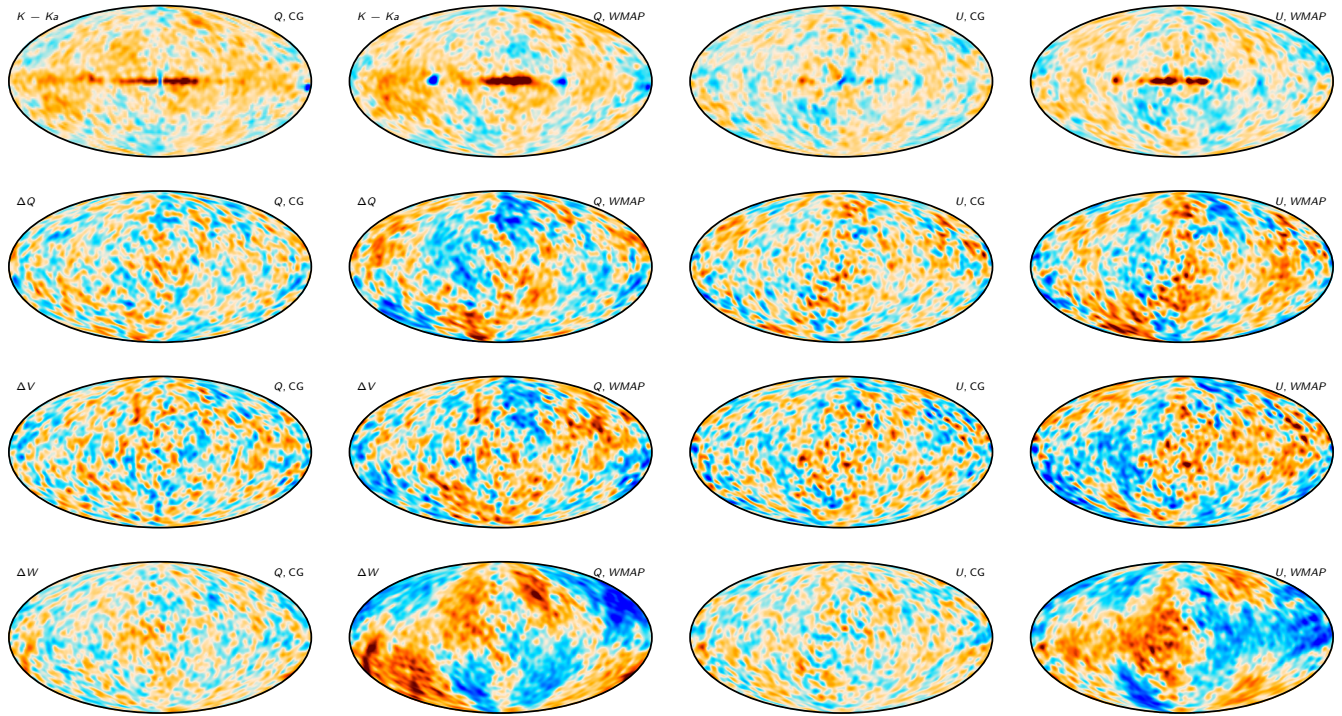


Fig. 30. Half-difference maps, smoothed by 10° .

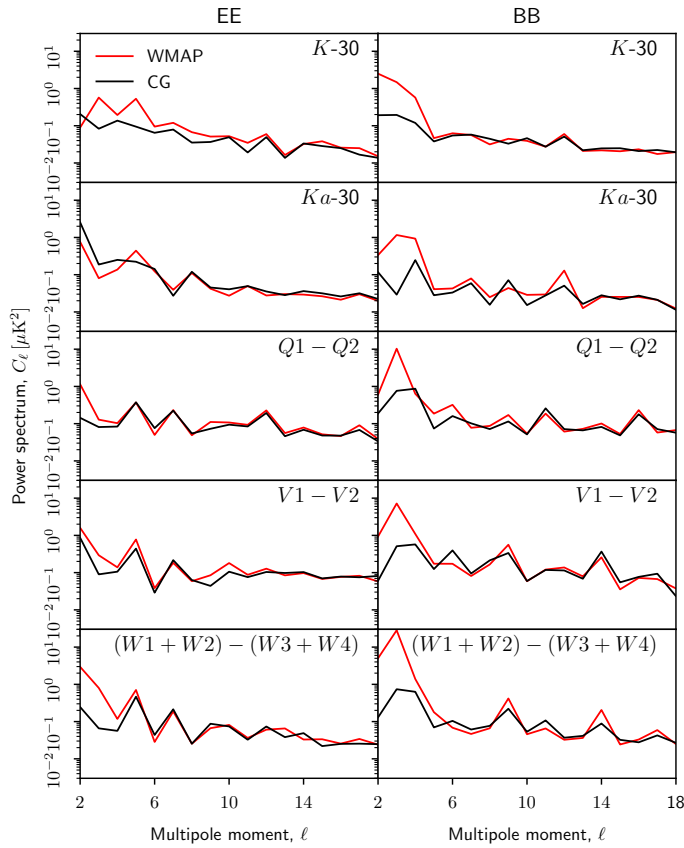
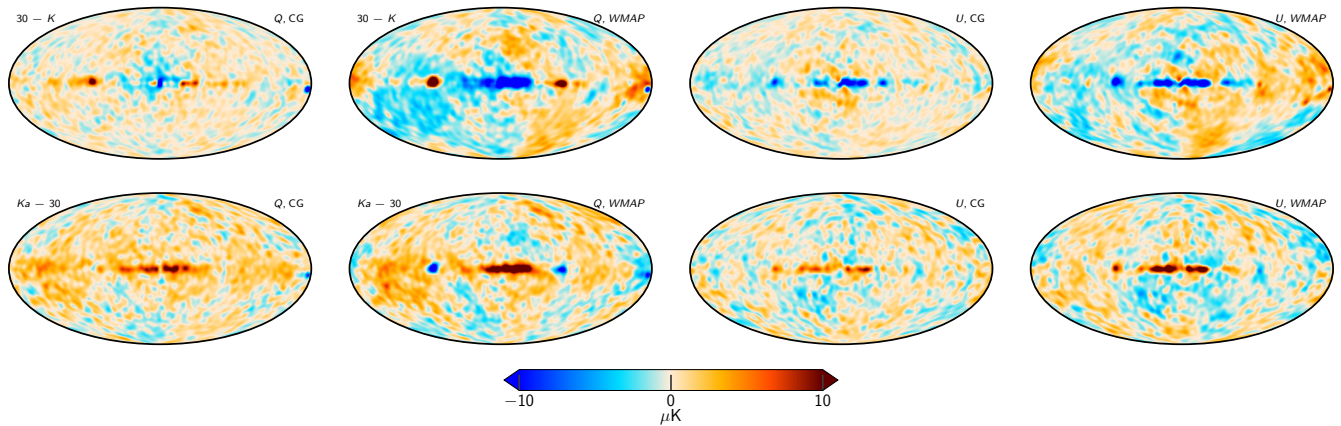
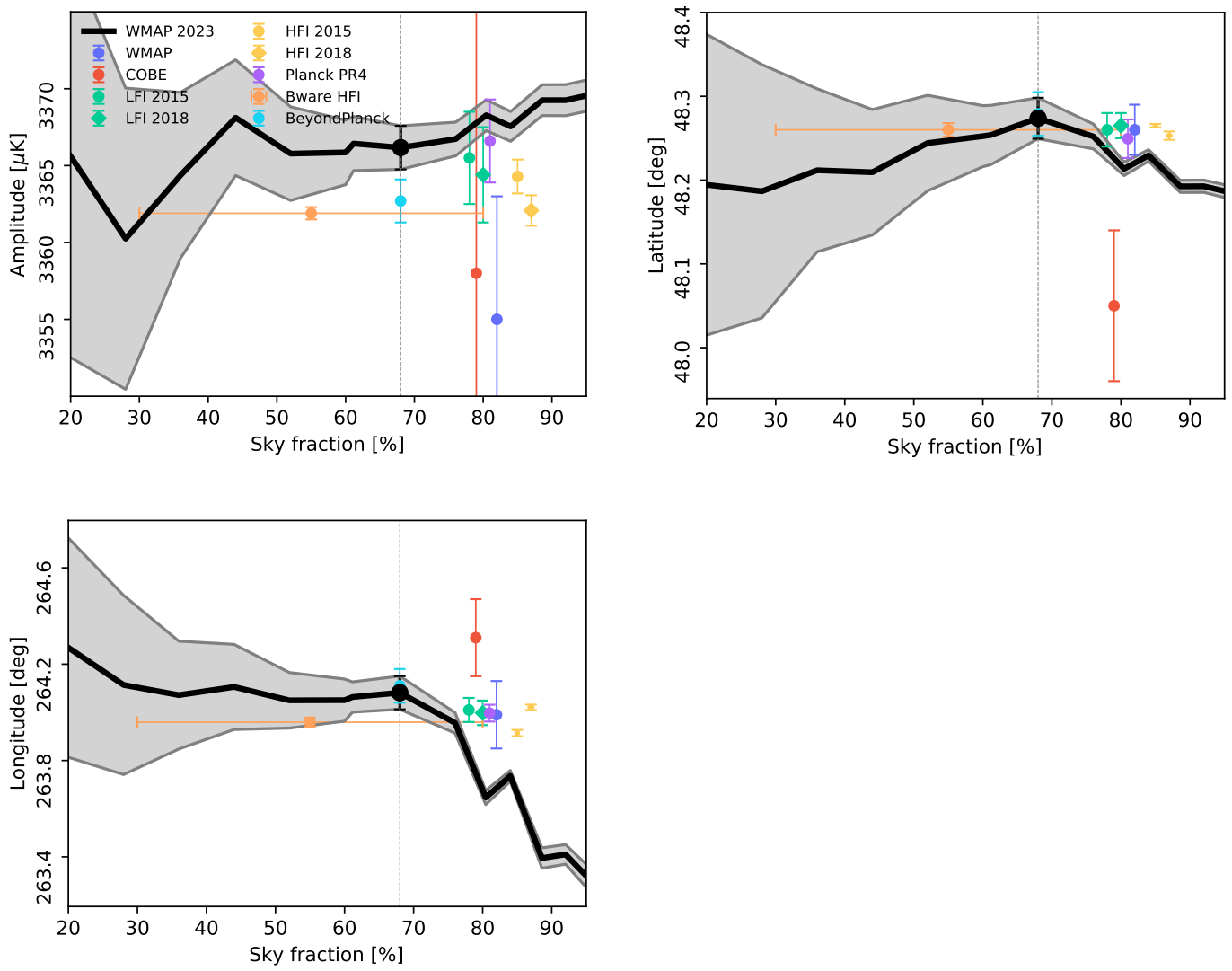
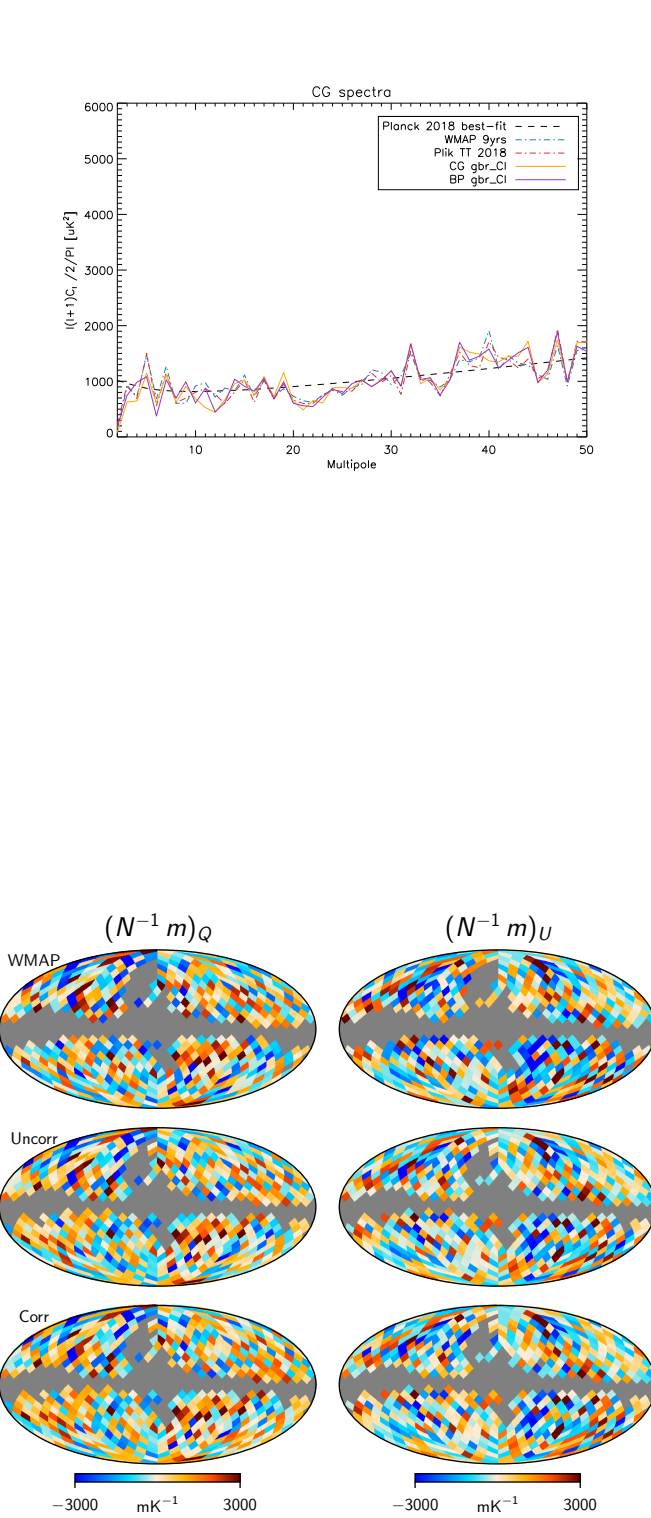
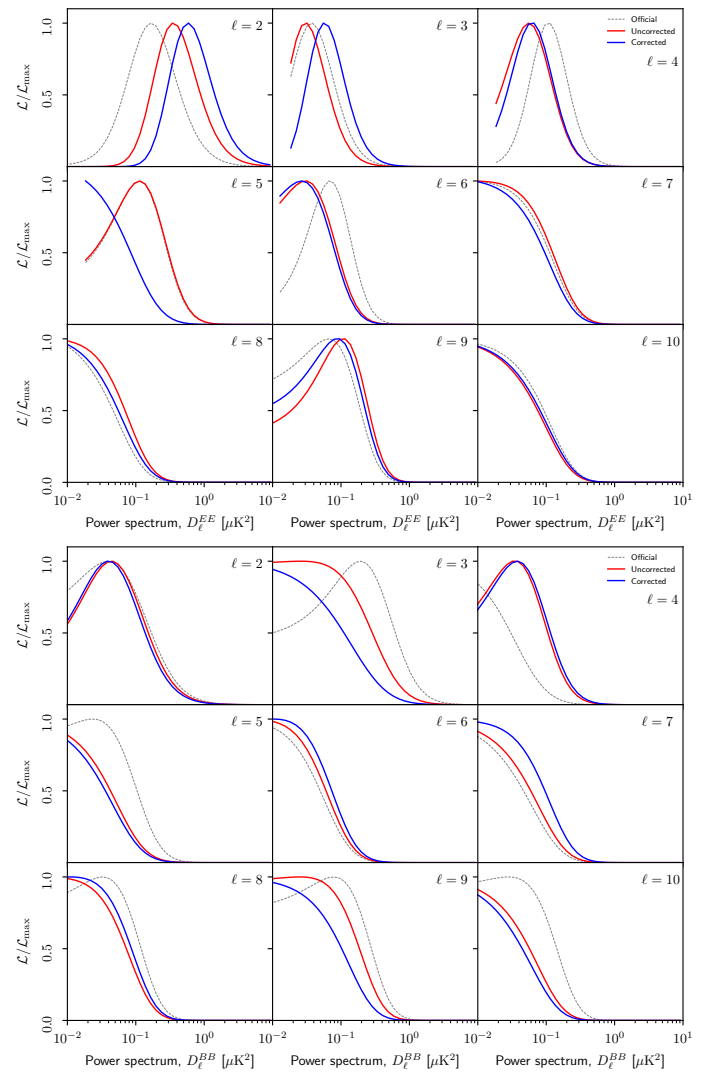


Fig. 31. Half-difference spectra.

**Fig. 32.** Mean of WMAP+LFI bands

**Fig. 33.** Noise-weighted likelihood input maps.**Fig. 34.** Likelihood slices

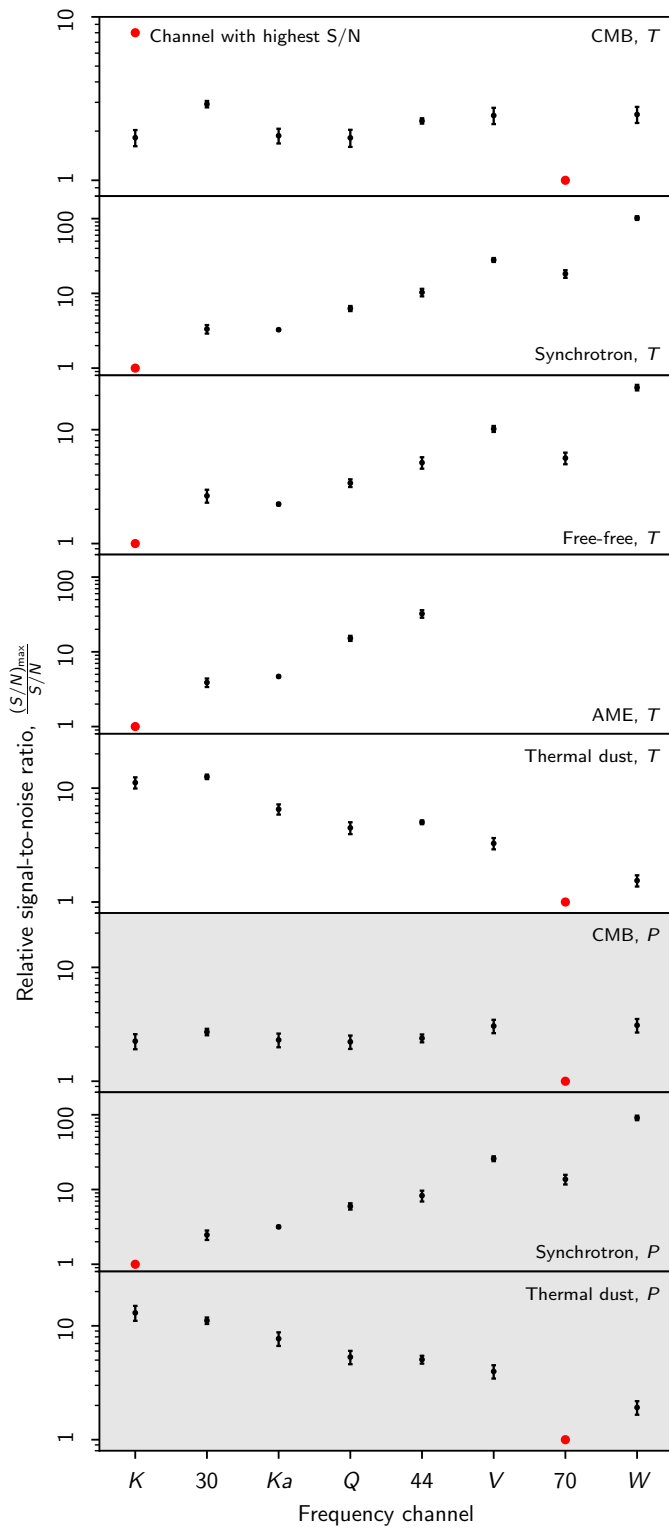


Fig. 35. Relative signal-to-noise ratios for WMAP and LFI channels and various components.

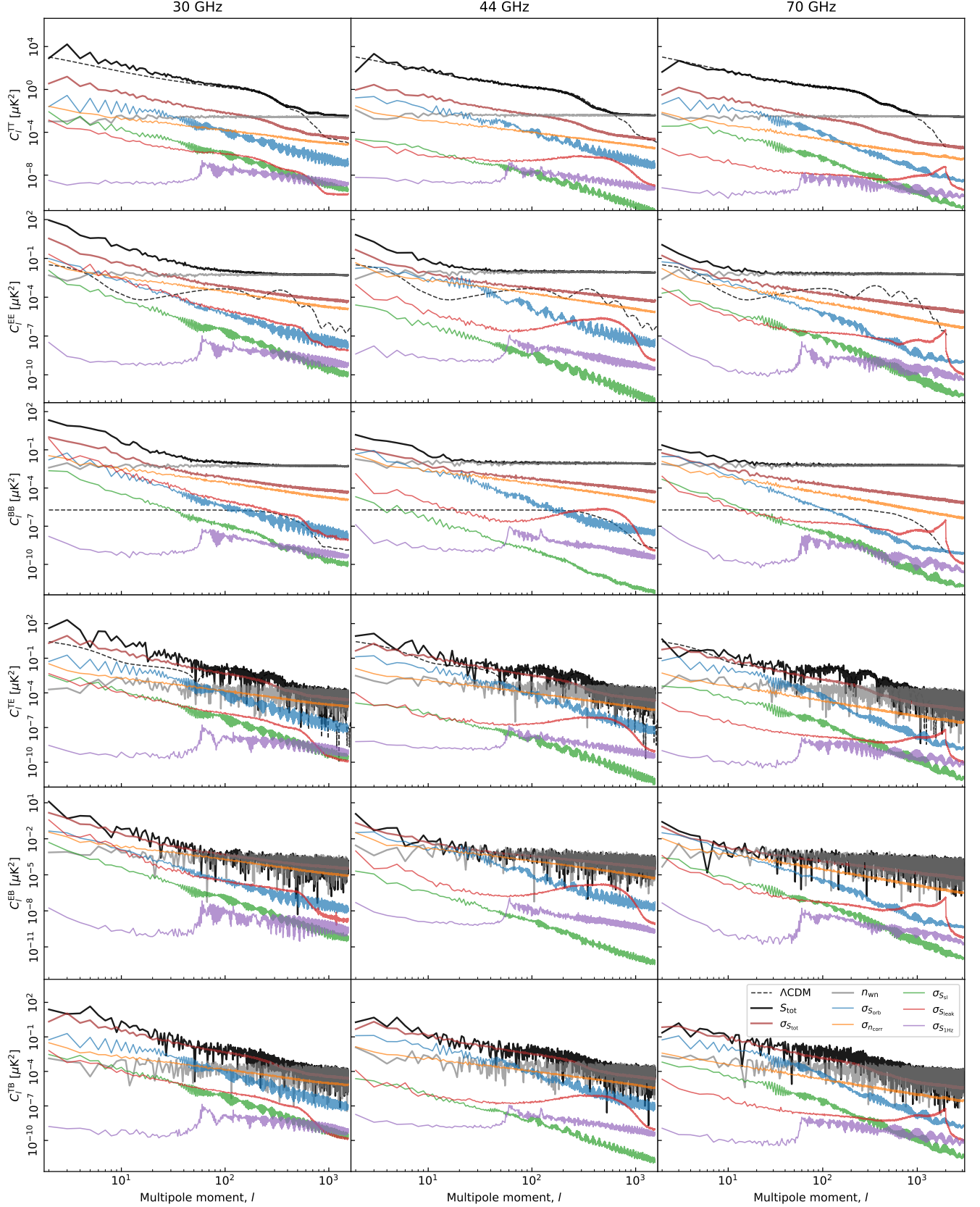


Fig. 36. Pseudo-spectrum standard deviation for each instrumental systematic correction shown in Figs. ??–?? (thin colored lines). For comparison, thick black lines show spectra for the full coadded frequency map; thick red lines show the standard deviation of the same (i.e., the full systematic uncertainty); gray lines show white noise; and dashed black lines show the best-fit *Planck* 2018 ΛCDM power spectrum convolved with the instrument beam. Columns show results for 30, 44 and 70 GHz, respectively, while rows show results for each of the six polarization states (TT, EE, BB, TE, TB, and EB). All spectra have been derived outside the CMB confidence mask presented by [Andersen et al. \(2022\)](#) using the HEALPix *anafast* utility, correcting only for sky fraction and not for mask mode coupling.

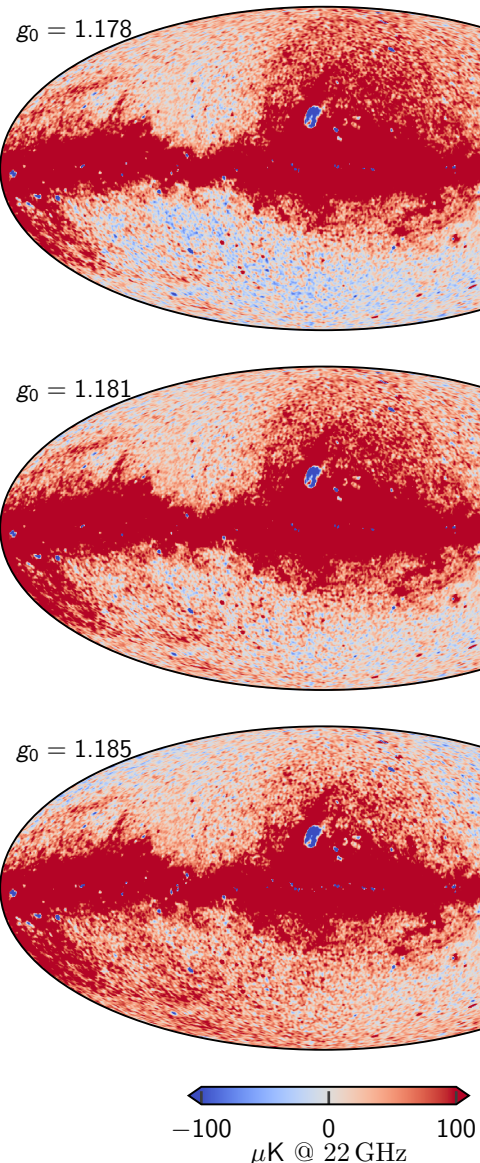


Fig. 37. Dependence on AME amplitude evaluated at 22 GHz as a function of absolute calibration. Each map comes from the fifth iteration of a dedicated `Commander` run that fixed g_0 while letting all other TOD parameters be fit. The values of $g_0 = 1.178$ and $g_0 = 1.185$ represent 3.5σ draws from the prior distribution with mean 1.1815 and standard deviation 0.001. The dipole visible in the top and bottom panels is aligned perfectly with the Solar dipole, and is directly due to variations in the K -band absolute calibration.

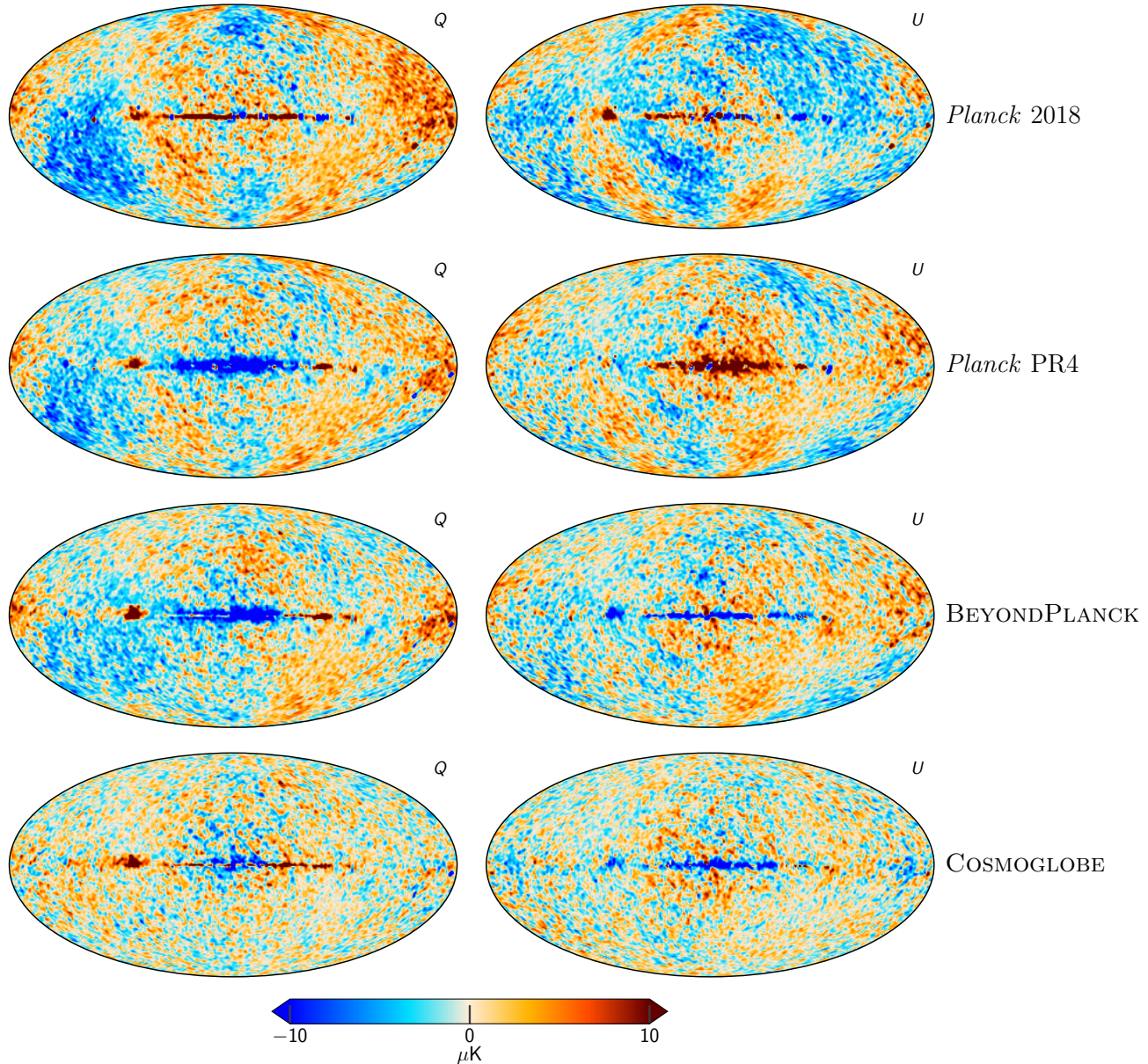


Fig. 38. Difference maps between the *Planck* 30 GHz and *WMAP* K-band maps. The columns are (1) *Planck* 2018 v. *WMAP*9, (2) *Planck* PR4 v. *WMAP*9, (3) BEYONDPLANCK v. *WMAP*9, and (4) COSMOGLOBE *Planck* 30 GHz and *WMAP* K-band both produced in this paper. All maps have been smoothed to a common resolution of 2° FWHM, and the K-band map has been scaled by 0.495 to account for different central frequencies, assuming a synchrotron spectral index $\beta_s = -3.1$.

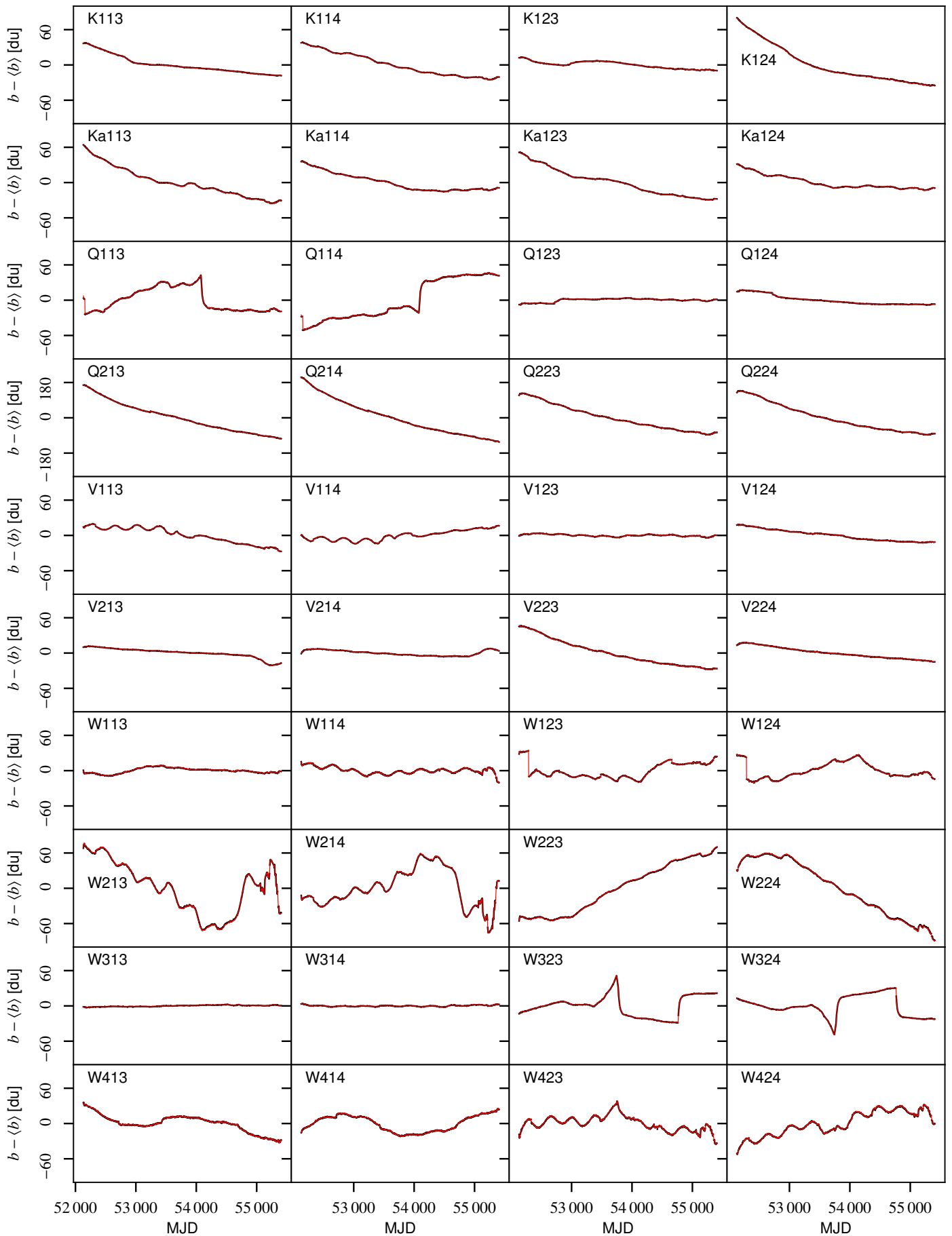
Appendix A: Survey of instrumental parameters

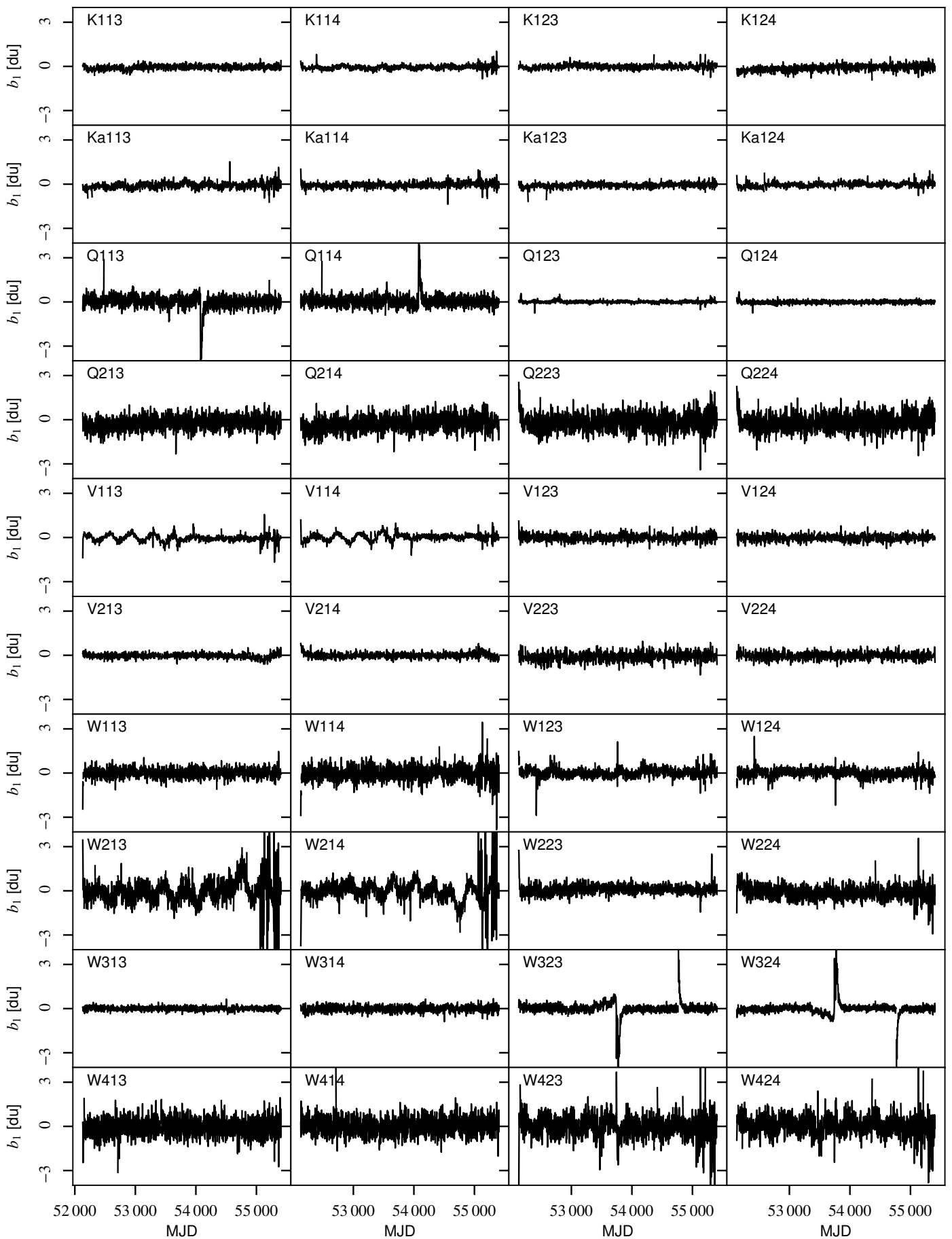
Appendix A.1: Gain, baselines, noise and χ^2

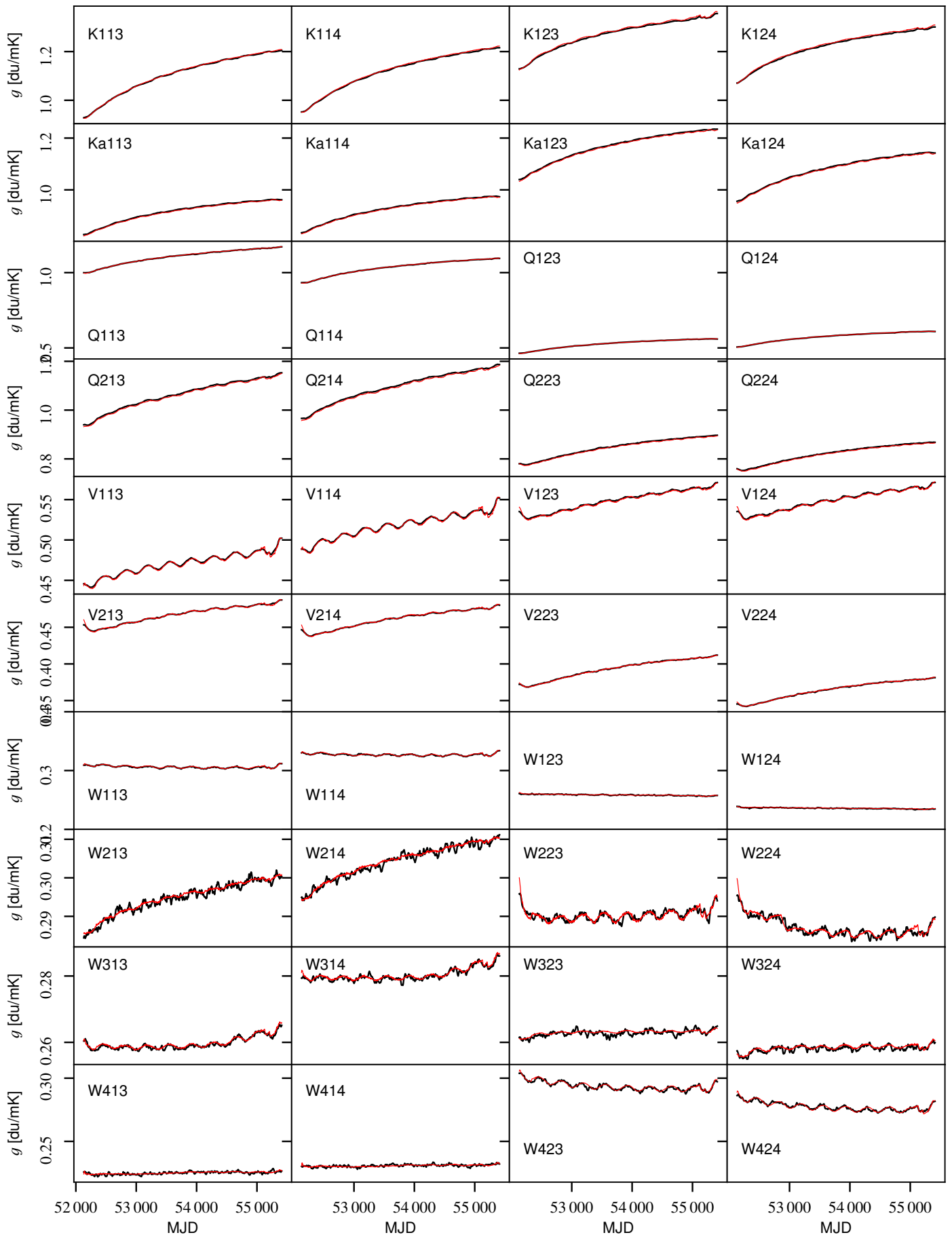
Appendix A.2: Transmission imbalance

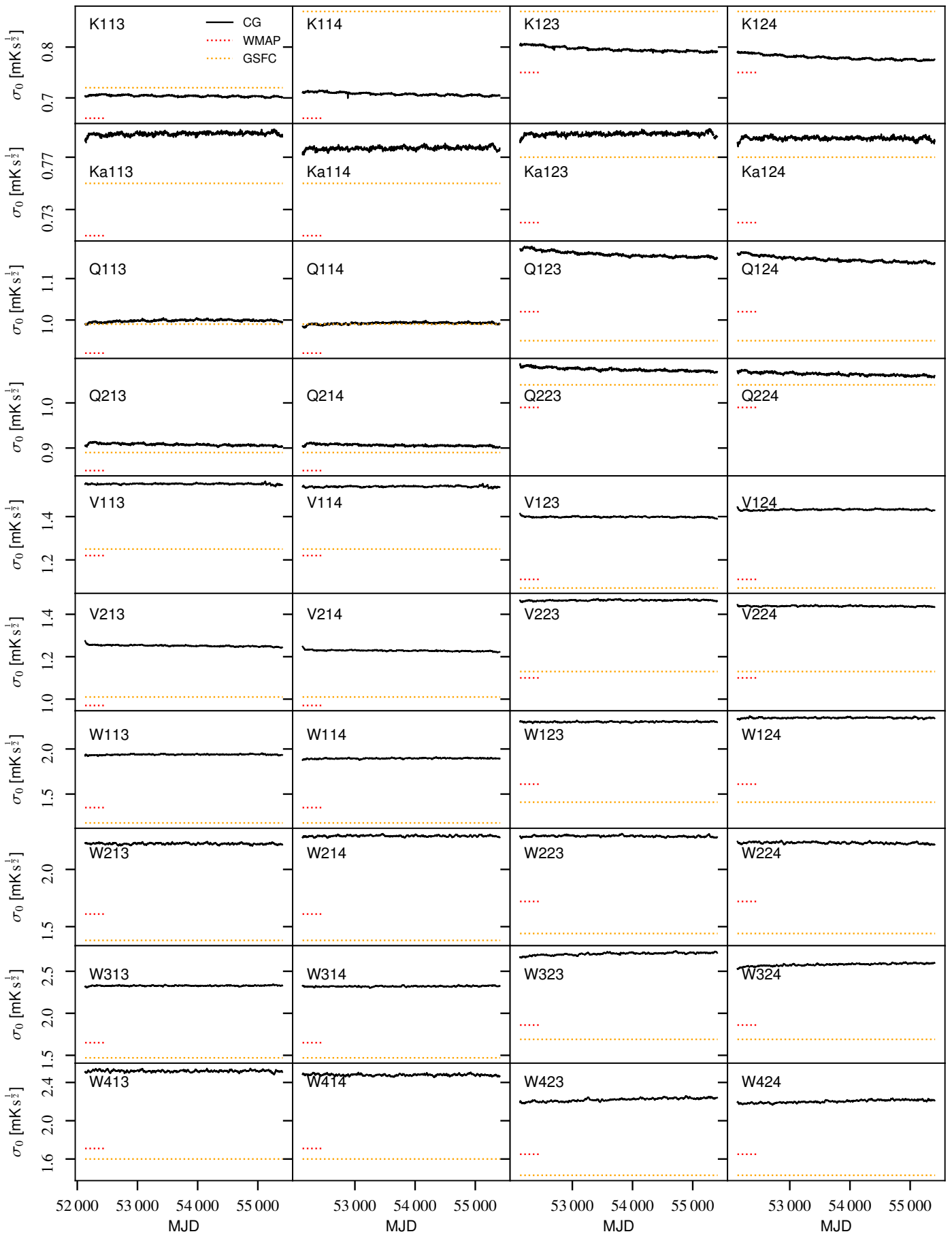
Appendix B: *WMAP* frequency map survey

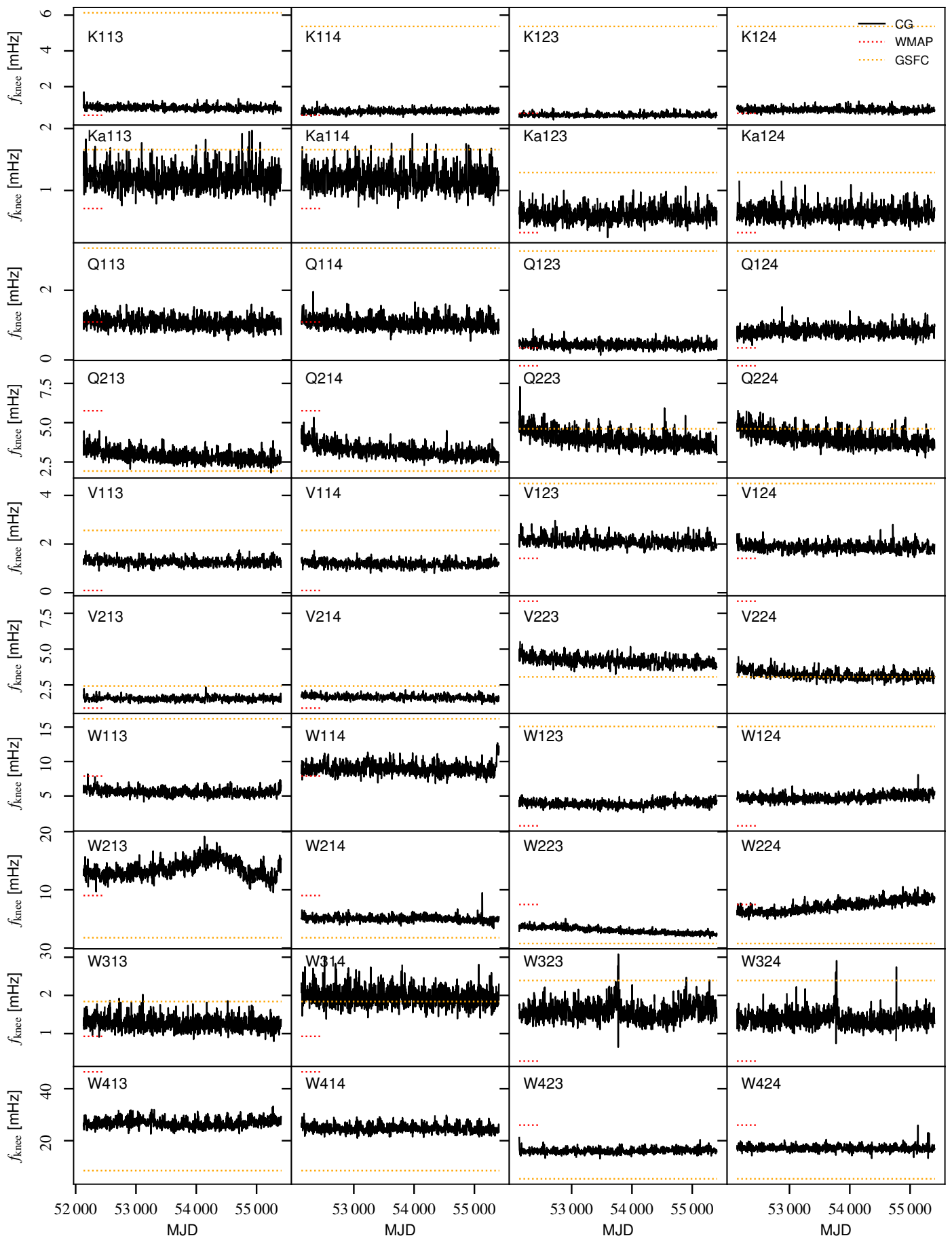
Appendix C: Comparison with BEYONDPLANCK LFI results

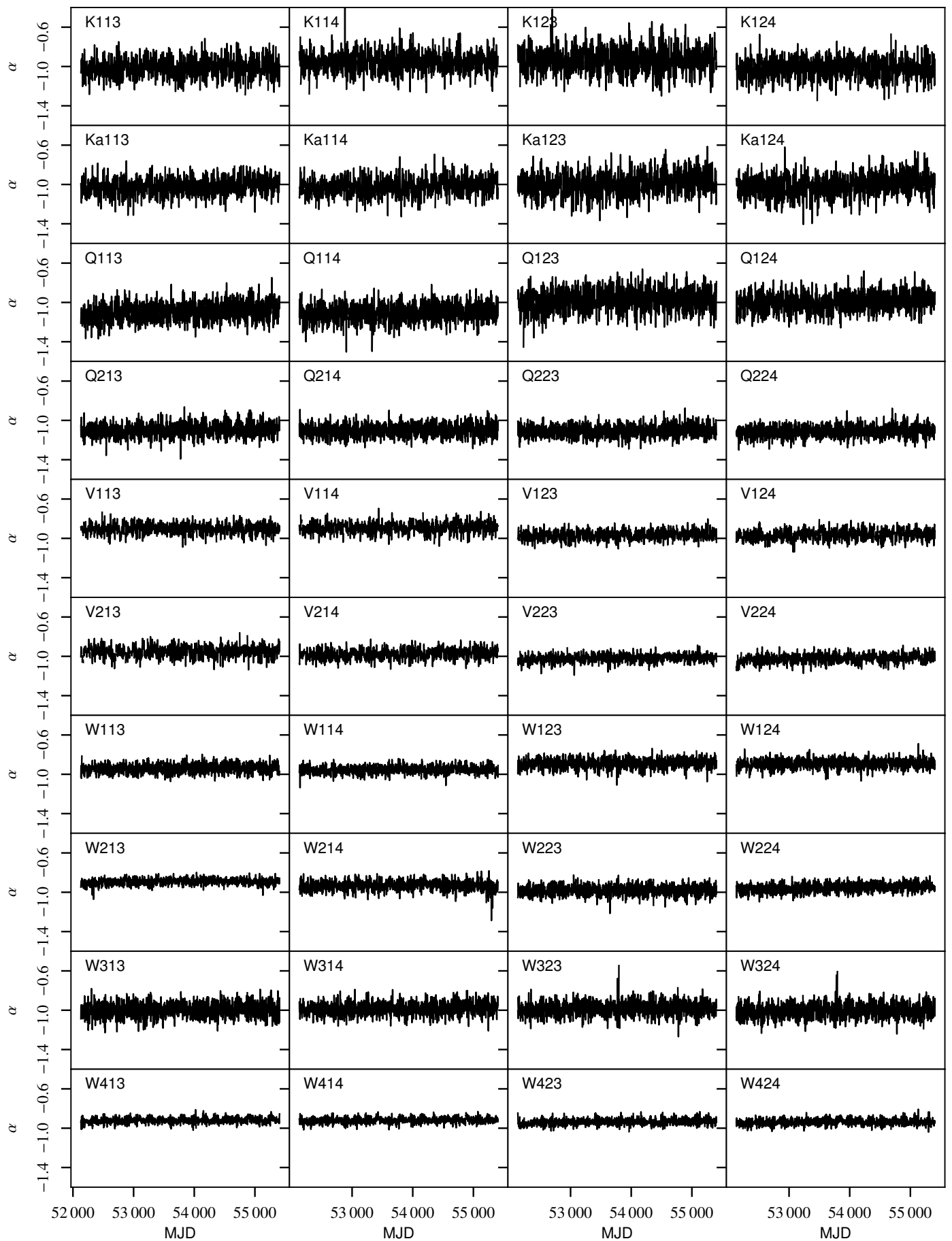
**Fig. A.1.** baseline.

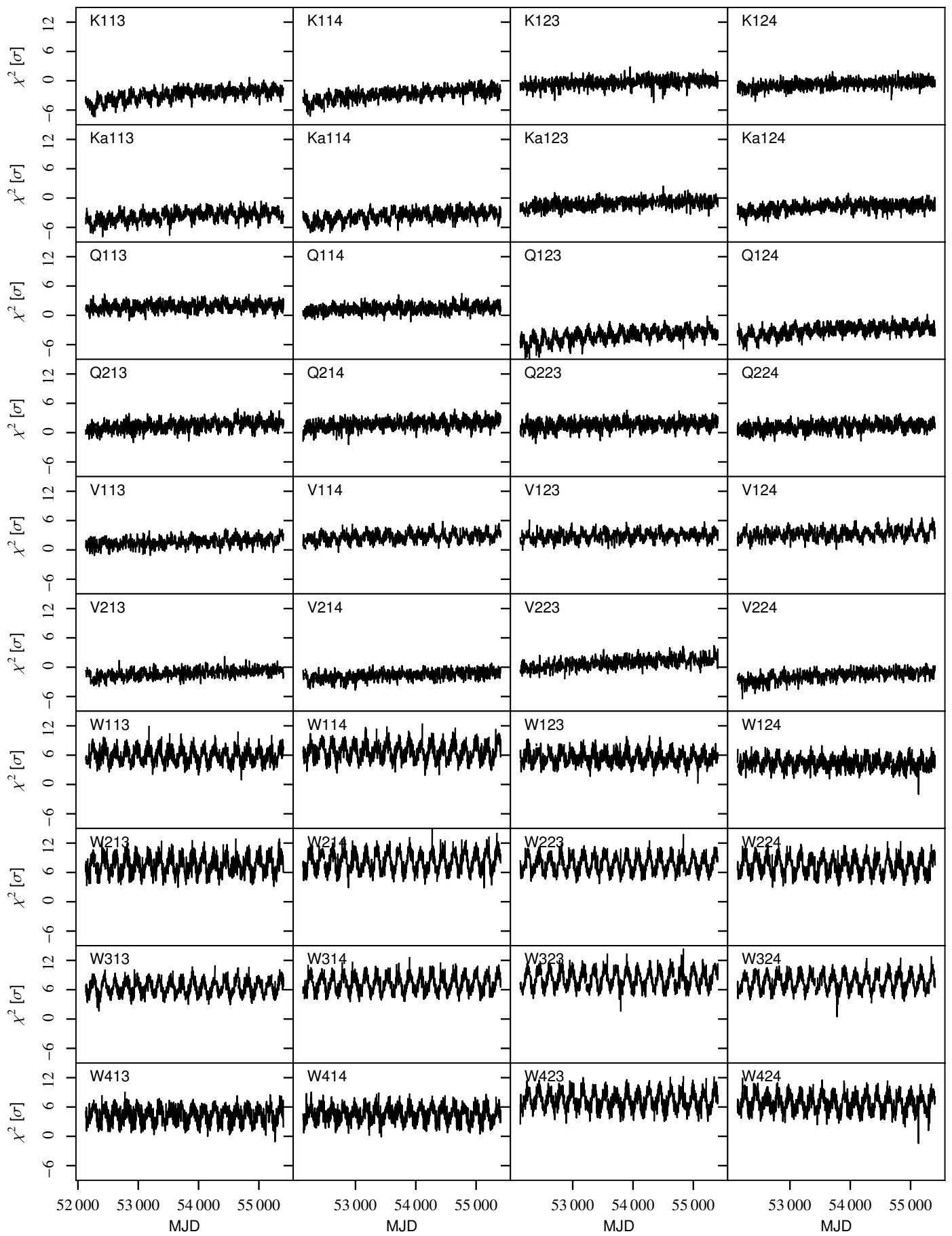
**Fig. A.2.** baseline slopes.

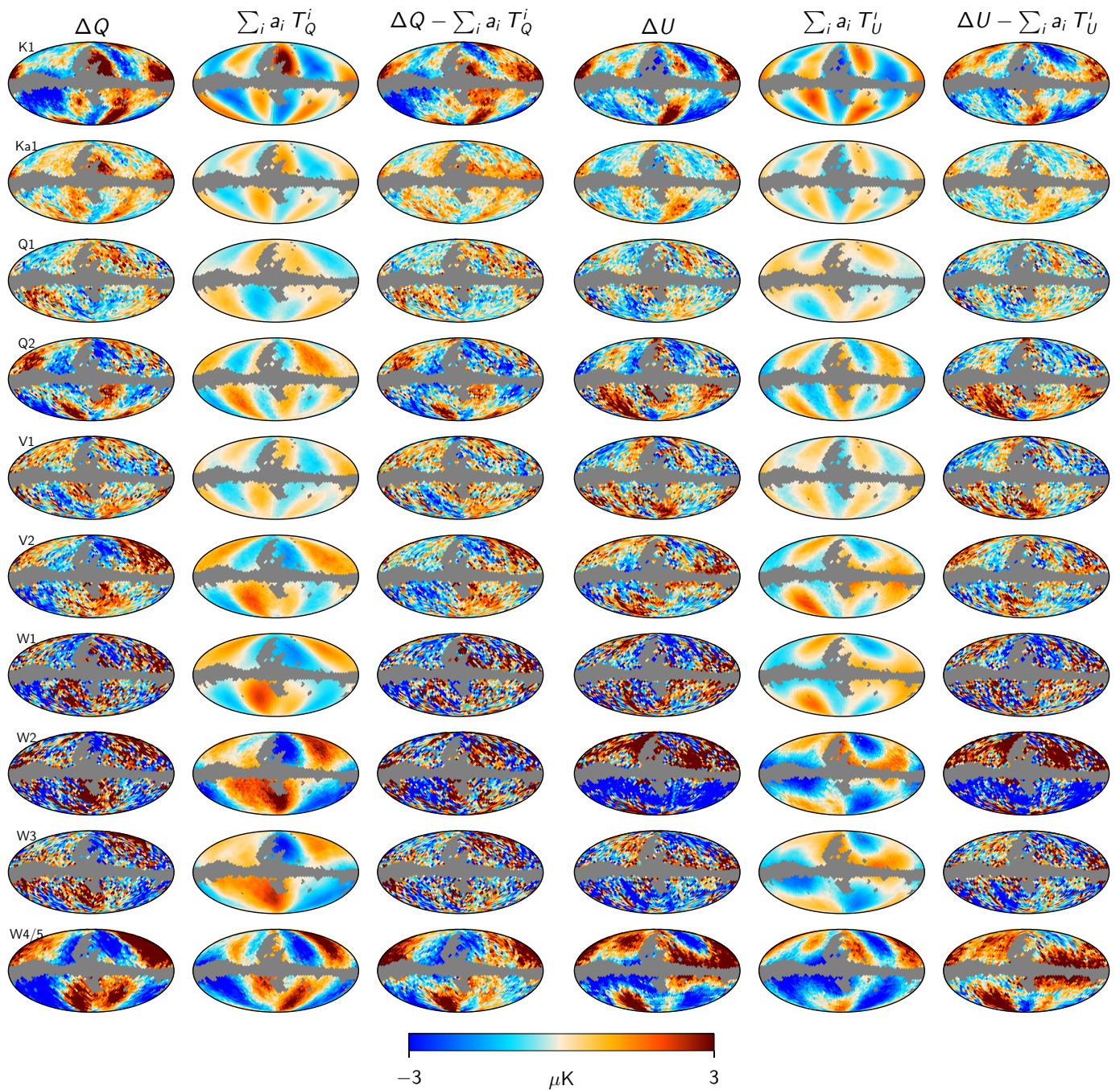
**Fig. A.3.** Gain.

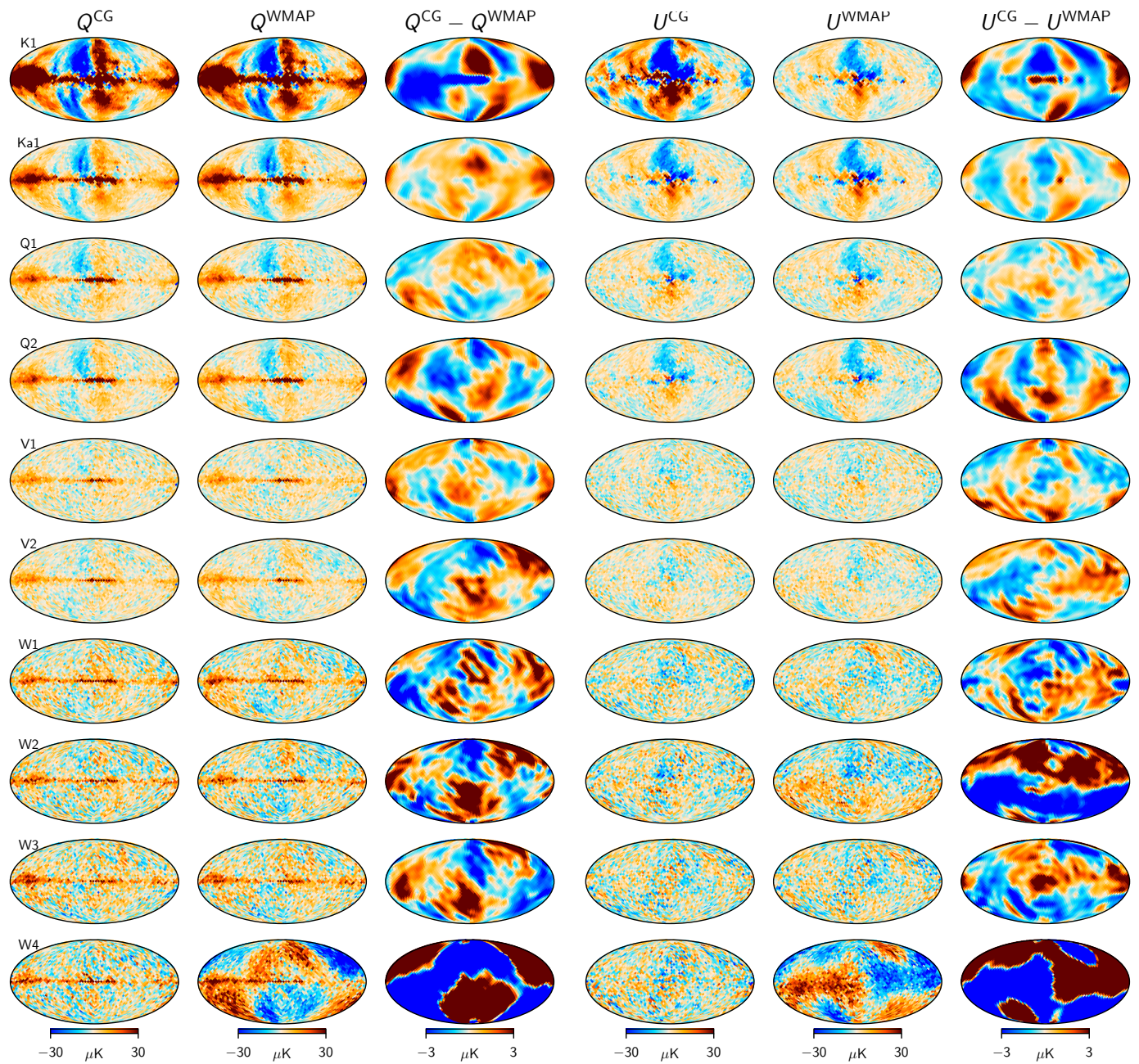
**Fig. A.4.** σ_0 .

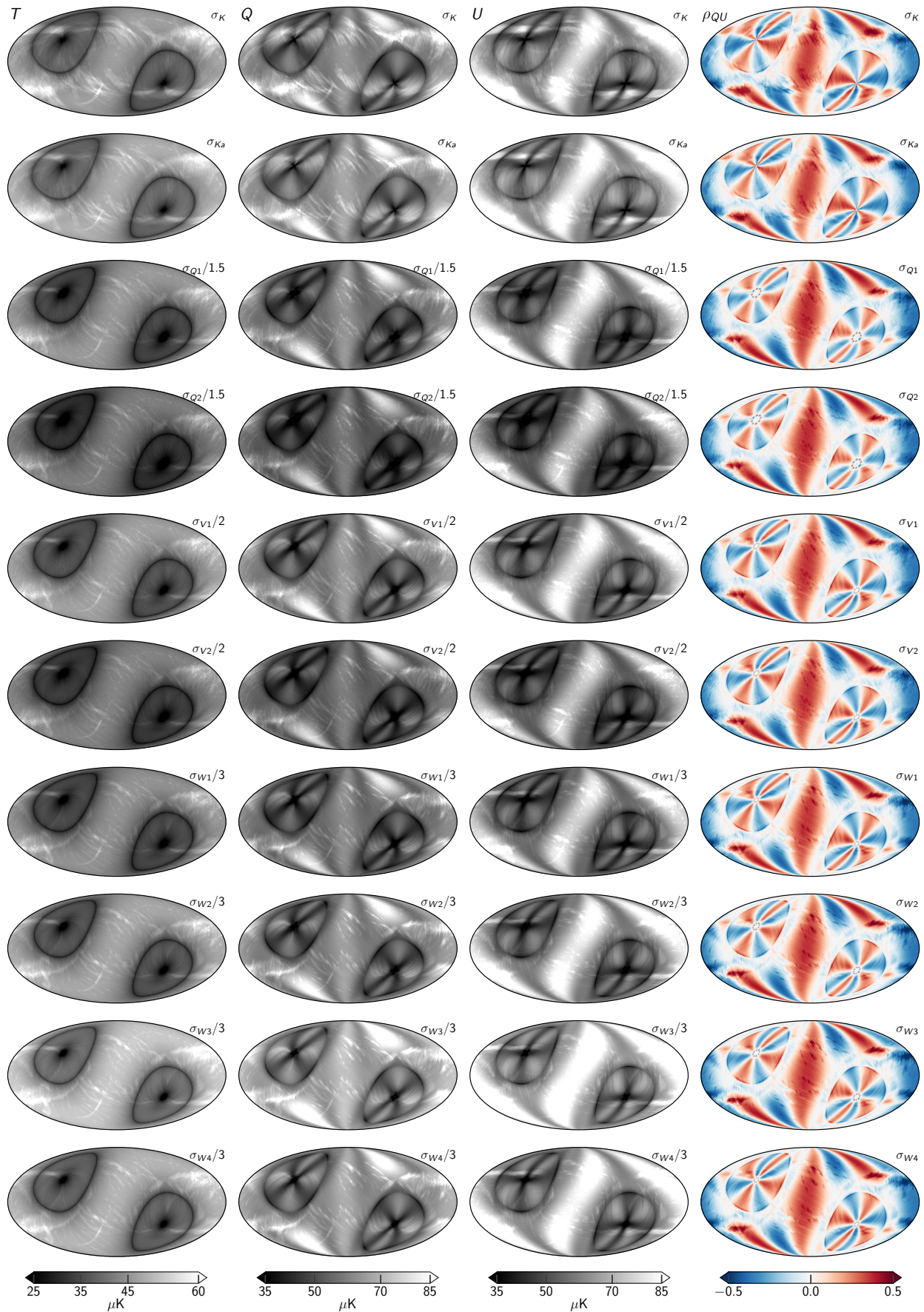
**Fig. A.5.** Fknee.

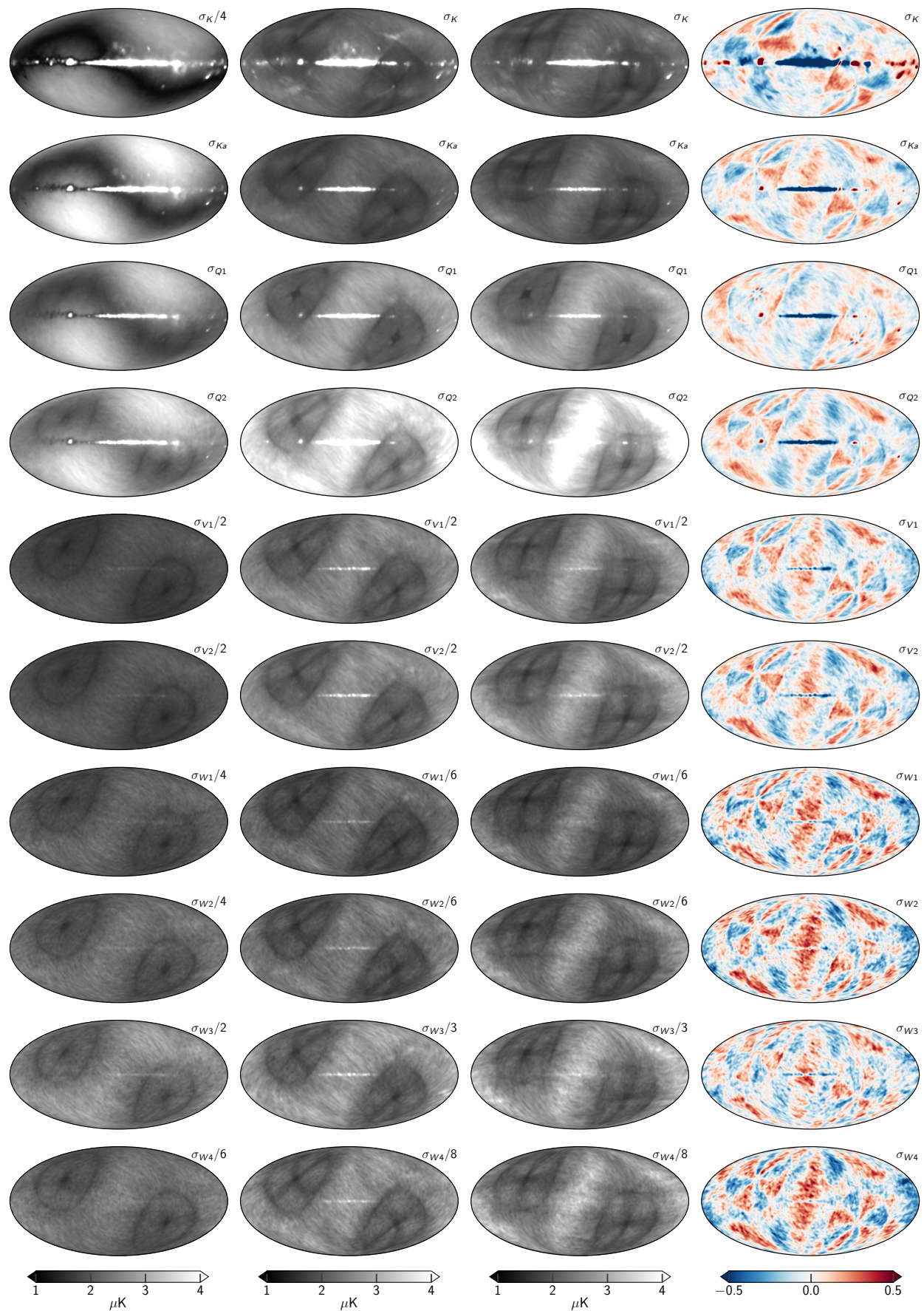
**Fig. A.6.** α .

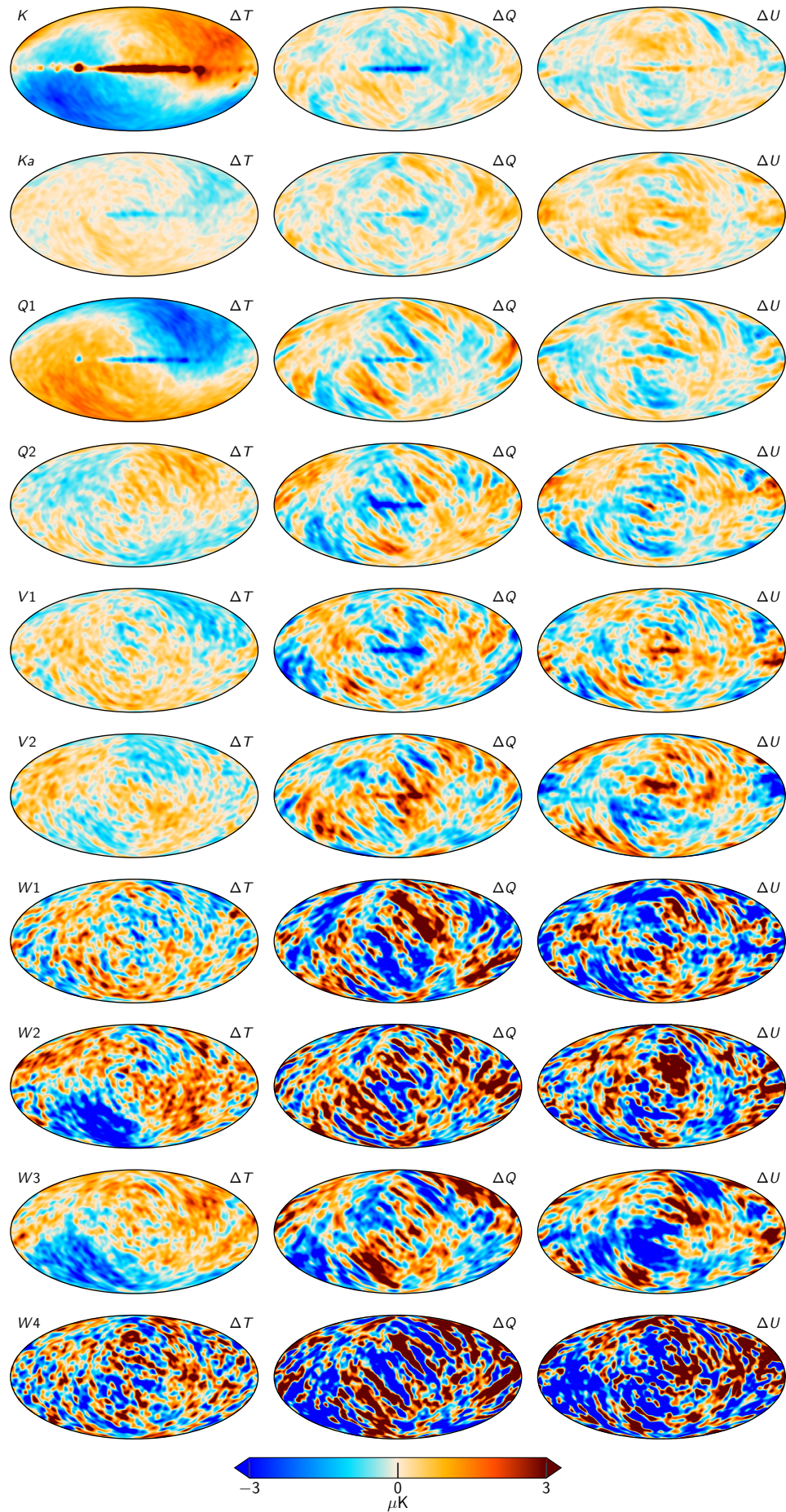
**Fig. A.7.** chisq.

**Fig. A.8.** Transmission imbalance templates

**Fig. B.1.** Sky maps

**Fig. B.2.** RMS maps

**Fig. B.3.** STD std

**Fig. B.4.** Differences between two samples

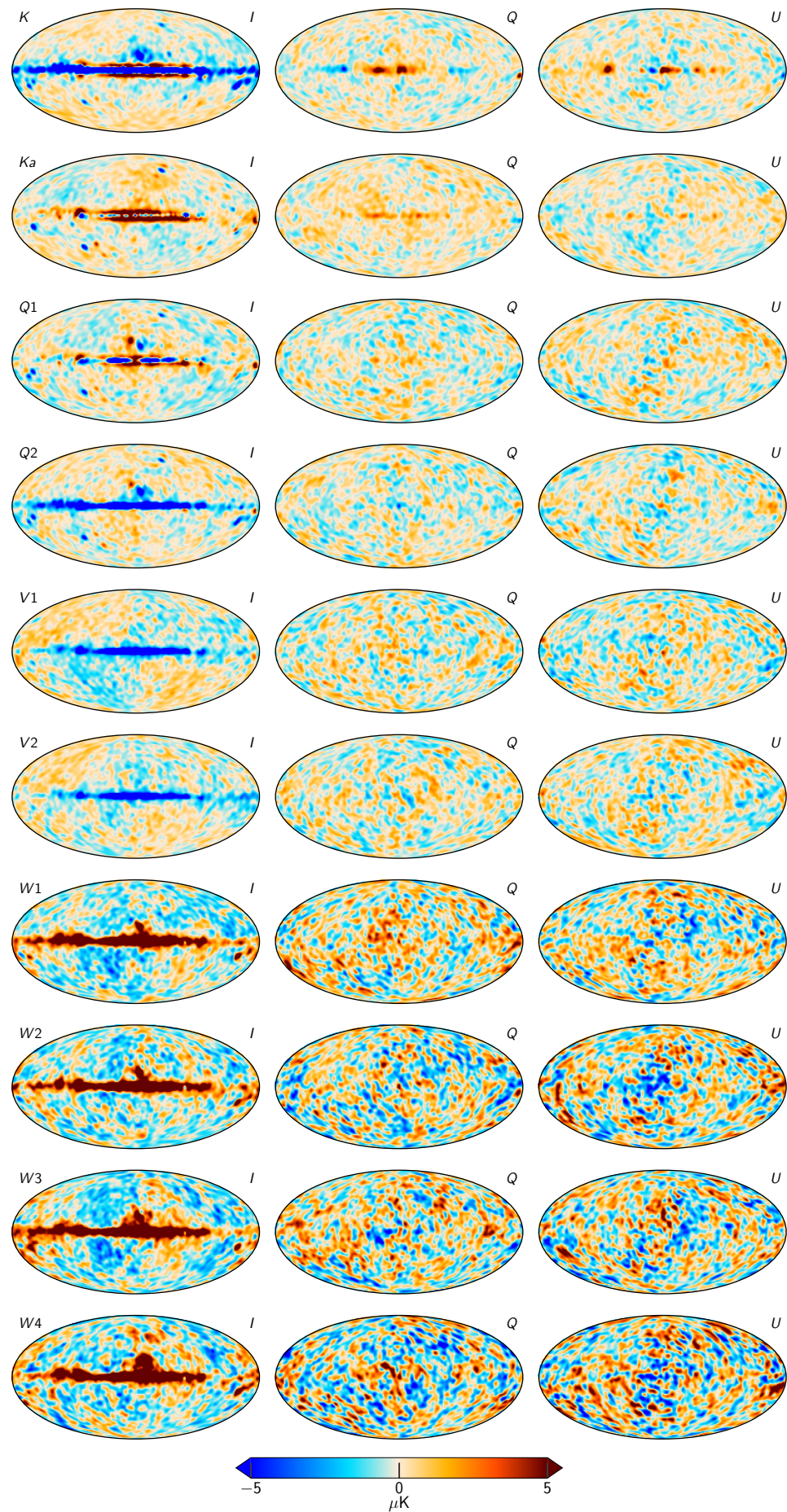


Fig. B.5. TOD Residuals for each of the WMAP channels, smoothed by 5° .
Article number, page 50 of 50